Time-lapse inversion of Controlled Source Electromagnetics using vertical sources and receivers

Dissertation
zur Erlangung des akademischen Grades
doctor rerum naturalium (Dr. rer. nat.)
im Fachbereich Geowissenschaften
der Freien Universität Berlin

vorgelegt von
Cedric Patzer

Berlin, 2018

Gutachter:

Betreuer:	Prof. Dr Oliver Ritter
	Freie Universität Berlin, Deutsches GeoForschungsZentrum Potsdam
Zweitgutachter:	Prof. Dr. Georg Kaufmann
	Freie Universität Berlin
Tag der Disputation:	08.01.2019

To my parents, Katrin and Ralph

Abstract

Knowledge of spatial and temporal distribution of fluids in the subsurface is crucial in a wide range of applications. During the production of crude oil typically high saline produced formation water is injected into the reservoir layer, aiming to push the oil towards production wells. While oil is commonly seen as an electrical insulator, the injected saline brines are characterised by low electrical resistivity. Thus, electromagnetic (EM) methods and especially Controlled Source Electromagnetics (CSEM) attracted an increasing interest to monitor these resistivity changes inside the reservoir over time.

This thesis mainly reports on numerical aspects of modelling and inversion of land based CSEM with particular focus towards hydrocarbon monitoring applications. Most of the presented developments were inspired by a superordinate research project including CSEM field surveys across an actively producing onshore oil field in Northern Germany.

In producing oil fields there exists a large number of steel-cased wells. Such existing oil field infrastructure and especially the presence of metal casings significantly alters the propagation of EM fields in the subsurface. Their spatially unfavourable dimensions effectively prohibits a straightforward implementation into the modelling grid. Thus I developed a new modelling approach allowing consideration of such thin but vertically extended highly conductive structures including their mutual interaction. The developed methodology had been implemented into existing modelling and inversion codes. Using the new approach to investigate the influence of metal casings on CSEM data shows that they act as additional inductively coupled vertical electric dipole sources at depth and thereby increase resolution capabilities at depth. The presence of metal casings can thus be exploited by optimising the source receiver layout in such a way that the strength of these additional vertical dipole sources is maximised.

An additional working package of the superordinate project was the measurement of vertical electric fields in a shallow observation well. However, measurements of vertical electric fields requires long measurement dipoles to achieve satisfactory signal-to-noise ratios. Such extended dipoles span several modelling cells and are therefore in conflict with assumptions usually made for modelling, that receivers can be represented as point dipoles. I therefore expanded the modelling and inversion codes to consider the physical receiver dimensions. The new algorithm implicitly considers imperfect alignment of the receiver with the corresponding field component. Without the consideration of this effect inversion of vertical electric field measurements is likely to cause erroneous results.

Finally I discuss different aspects of time-lapse inversion required to track changes in fluid saturation over time. The cascaded inversion scheme is applied to synthetic time-lapse data for a simplified oilfield undergoing brine flushing. The influence of various inversion parameters in particular different regularisation techniques are examined. Surface based sources and receivers typically provide low sensitivity towards deep targets in highly conductive backgrounds. Despite that using additional constraints, in particular a model weighting scheme together with energised steel casings allowed to track resistivity changes inside the reservoir based on synthetic time-lapse data.

Kurzzusammenfassung

Wissen über räumliche und zeitliche Verteilung von Fluiden im Untergrund is unerlässlich für eine Reihe von Anwendungen. Typischerweise wird während der Förderung von Rohöl salinares produziertes Formationswasser in die ölführende Formation injiziert um das Öl-Wasser-Gemisch in Richtung der Förderbohrungen zu spülen. Während Öl als elektrischer Isolator gilt, zeichnen sich die injizierten salinaren Fluide durch eine hohe elektrische Leitfähigkeit aus. Daher erfahren elektromagnetische Methoden und insbesondere Controlled Source Electromagentics (CSEM) zunehmendes Interesse diese Änderung des elektrischen Widerstands mit der Zeit zu überwachen.
Diese Arbeit beschäftigt sich im wesentlichen mit numerischen Aspekten der Modellierung und Inversion von CSEM an Land mit speziellem Fokus auf der Überwachung der Kohlenwasserstoff Produktion. Die meisten der gezeigten Entwicklungen sind entwickelt im Zuge eines übergeordneten Forschungsprojektes inklusive CSEM Feldmessungen in einem produzierenden Ölfeld in Norddeutschland.
Produzierende Ölfelder sind gekennzeichnet durch eine große Anzahl von Stahl verrohrten Bohrungen. Die Anwesenheit von Stahlinfrastruktur insbesondere von Stahlschutzrohren beeinflusst die Ausbreitung von elektromagnetischen Feldern im Untergrund. Deren unvorteilhafte Geometrie erlaubt keine direkte Berücksichtigung in dem Modellierungsgitter. Daher habe ich einen neuen Modellierungsanzatz entwickelt der es erlaubt solch dünne aber vertikal ausgedehnte hochgradig leitfähige Strukturen inklusive deren gegenseitige Wechselwirkung zu berücksichtigen. Die entwickelte Methode wurde in bestehende Modellierungs- und Inversionssoftware implementiert. Mithilfe dieses neuen Ansatzes konnte der Einfluss von Stahlverrohrungen auf CSEM Daten untersucht werden. Stahlverrohrungen wirken wie zusätzliche induktiv angeregte vertikale elektrische Dipolquellen im Untergrund und helfen daher die Auflösung in der Tiefe zu erhöhen. Die Anwesenheit von Stahlverrohrungen kann daher ausgenutzt werden in dem man die Quell-Empfänger-Geometrie in einer Art und Weise optimiert, die die Stärke dieser zusätzlichen vertikalen Dipolquellen maximiert.
Ein weiteres Arbeitspaket des übergeordneten Forschungsprojektes bestand in der Messung von vertikalen elektrischen Feldern in flachen Beobachtungsbohrungen. Messungen des vertikalen elektrischen Feldes erfordert lange Messdipole um ein ausreichendes Signal-Rausch-Verhältnisses zu gewährleisten. Solch ausgedehnte Dipole überspannen mehrere Zellen des Modellierungsgitters und verletzen die übliche Annahme, wonach die Länge der Empfänger vernachlässigbar ist. Daher habe ich die bestehenden Modellierungs- und Inversionsprogramme erweitert um die physischen Dimensionen von elektrischen Feld Empfängern zu berücksichtigen. Der implementierte Algorithmus berücksichtigt implizit Abweichungen der Orientierung des Messdipols von der Richtung der zu messenden Feldkomponente. Ohne dieser Berücksichtigung führt eine Inversion von vertikalen elektrischen Feld Daten zu fehlerhaften Ergebnissen.
Schließlich werden unterschiedliche Aspekte von time-lapse Inversion diskutiert, welche notwendig ist um Änderungen der Fluidzusammensetzung abzubilden und zu verfolgen. Eine kaskadiertes Inversionsschema wurde auf synthetische time-lapse Daten eines vereinfachten Ölfeldes angewendet. Untersucht wurde der Einfluss verschiedener

Parameter insbesondere verschiedener Regularisierungstechniken. Sender und Empfänger an der Erdoberfläche sind typischerweise wenig sensitiv zu tiefen Strukturen in leitfähiger Umgebung. Anhand von synthetische Daten konnte gezeigt werden, dass das benutzen zusätzlicher Nebenbedingungen wie einer Modellgewichtung und dem ausnutzen von vorhandenen Stahlverrohrungen es dennoch erlaubt Änderungen innerhalb des Ölreservoirs zu lokalisieren.

Eidesstattliche Erklärung

Ich versichere hiermit an Eides Statt, dass diese Arbeit von niemand anderem als meiner Person verfasst worden ist. Alle verwendeten Hilfsmittel wie Berichte, Bücher, Internetseiten oder ähnliches sind im Literaturverzeichnis angegeben, Zitate aus fremden Arbeiten sind als solche kenntlich gemacht. Die Arbeit wurde bisher in gleicher oder ähnlicher Form keiner anderen Prüfungskommission vorgelegt und auch nicht veröffentlicht.

July 10, 2019

Cedric Patzer

Contents

1 Introduction **3**

2 The Controlled Source Electromagnetics method **5**
2.1 CSEM data acquisition and processing 6
2.2 Existing modelling and inversion algorithms 7
2.2.1 Forward modelling 8
2.2.2 Inversion 9
2.3 Radiation pattern of horizontal electric dipole transmitters 10

3 Electromagnetic monitoring of the Bockstedt oil field **13**
3.1 The Bockstedt oil field 13
3.2 2D Magnetotelluric survey and CSEM modelling study 15
3.3 CSEM Field surveys 18

4 Steel casings **21**
4.1 Finite element modelling 22
4.2 Implementation into CSEM modelling and inversion 23
4.2.1 Calculation of coupling coefficients 25
4.2.2 Implemented optimisation strategies 26
4.2.3 Estimation of background conductivity 27
4.3 Numerical experiments 28
4.3.1 Current distributions along casings 29
4.3.2 Implications for the Bockstedt field surveys 32
4.4 Inversion Examples 33
4.4.1 Inversion neglecting steel casings 33
4.4.2 Sensitivity Study 34
4.4.3 Influence on reservoir resolution 36
4.4.4 Application to field data 41
4.5 Discussion and conclusions 43

5 Elongated Receivers **45**
5.1 Implementation 46
5.1.1 Calculation of summation operator 47
5.2 Modelling Examples 48
5.2.1 Horizontal Field Receivers 48
5.2.2 Vertical receivers 51

5.3 Inversion Examples . . . 56
5.3.1 Sensitivity . . . 57
5.3.2 Inversion result . . . 59
5.4 Summary and Discussion . . . 61

6 Time-lapse inversion **63**
6.1 A reference time-lapse dataset . . . 63
6.2 Choice of time-lapse methodologies . . . 65
6.2.1 Data space approaches . . . 65
6.2.2 Model space approaches . . . 66
6.3 Regularisations . . . 67
6.3.1 Smoothness constraint regularisation . . . 67
6.3.2 Tikhonov . . . 69
6.3.3 Minimum support . . . 69
6.3.4 Cauchy . . . 69
6.4 An unconstrained inversion example . . . 70
6.5 Implementation of additional constraints . . . 71
6.5.1 Starting and reference models . . . 71
6.5.2 Model weighting . . . 72
6.5.3 Bounded conductivity transformation . . . 73
6.6 Time-lapse inversion results . . . 73
6.6.1 Tikhonov + Modelweighting . . . 74
6.6.2 Tikhonov + Model Weighting + Conductivity Boundaries . . . 75
6.6.3 Minimum Support + Model weighting . . . 78
6.6.4 Cauchy + Model weighting . . . 79
6.6.5 Tikhonov + Modelweighting + Ez . . . 79
6.6.6 Choice of the starting Model . . . 82
6.7 Discussion and Conclusion . . . 84

7 Summary **89**

List of Figures

2.1 Sketch of CSEM method 5
2.2 Sketch of the CSEM transmitter 6
2.3 Sketch of an EM receiver station 7
2.4 Sketch of staggered Finite Difference (FD) grid 9
2.5 Schematic radiation pattern of HED source 11

3.1 Map of the Lower Saxony Basin 14
3.2 3D resistivity model used for baseline study 15
3.3 Absolute and relative differences of electric and magnetic field components 16
3.4 Absolute and relative differences of E_x and H_y components at surface . 17
3.5 Absolute and relative differences of electric and magnetic field components 18
3.6 Setup of all CSEM field surveys across the Bockstedt oil field 19

4.1 Map view of the source-borehole geometry 22
4.2 Anomalous electric field due to presence of well 23
4.3 Sketch indicating the dimensions of one casing segment (taken from Patzer et al., 2017b). 24
4.4 Sketch showing independent coupling coefficients 27
4.5 Current distribution along a single steel-cased well 28
4.6 Relative current strength along steel casings 30
4.7 Current distribution with distance to the transmitter 31
4.8 Relative change in TFs amplitude due to the presence of steel-cased wells 32
4.9 Final model of inversion of synthetic data neglecting presence of wells . 34
4.10 Misfits of inversion neglecting casings 35
4.11 Change of the cumulative sensitivity 36
4.12 True model used to generate synthetic data 37
4.13 Final inversion models under the influence of steel casing 38
4.14 Initial misfit of one TF 39
4.15 Final misfit of one TF 40
4.16 Inversion results of field data inversion 42

5.1 Sketch illustrating the summation operator (taken from Patzer et al., 2019) 47
5.2 Comparison classical point HED and elongated HED 49
5.3 Comparison imperfect aligned receiver 50
5.4 2D MT model to illustrate static shift 52

5.5 Vertical electric field receiver and field distribution with depth 53
5.6 Deviation from verticality 54
5.7 Effect of deviation on field data (inline component) 56
5.8 Effect of deviation on field data (broadside component) 57
5.9 True model used for inversion 58
5.10 Sensitivity distribution VED receiver 58
5.11 Comparison of inversion results between classical HED receivers and elongated vertical electric dipole (VED) receivers 60

6.1 True models of synthetic time-lapse dataset 64
6.2 Time-lapse difference of synthetic data 65
6.3 Inversion model using smooth inversion showing overshooting effect . 68
6.4 Unconstrained 3D inversion time-step 1 70
6.5 Initial misfit of the unconstrained inversion 71
6.6 Final misfit of the unconstrained inversion 72
6.7 Model weighting scheme 73
6.8 Parameter transformation 74
6.9 Inversion models of the reference dataset 75
6.10 Misfit of inversion models of the reference dataset 76
6.11 Inversion models of the reference dataset including constraints on conductivity 77
6.12 Distribution of misfits per receiver station 77
6.13 Inversion models of the reference dataset using Minimum support regularisation 78
6.14 Distribution of misfits per receiver station for the Minimum Support time-lapse inversion 79
6.15 Inversion models of the reference dataset using Cauchy regularisation . 80
6.16 Development of nRMS over the iterations 80
6.17 Time-lapse inversion models of modified reference dataset using vertical receivers 81
6.18 Distribution of misfits for the time-lapse inversion 82
6.19 Constrained starting model for time-lapse inversion 83
6.20 Time-lapse inversion model of modified starting model 83
6.21 Distribution of misfits for the time-lapse inversion 85

Legend of used symbols and constants

Symbol	Name	Unit	Description
$\mathbf{E}$	Electric field	$[\mathrm{V\,m^{-1}}]$	
$\mathbf{B}$	Magnetic flux density	[T]	
$\mathbf{H}$	Magnetic field strength	$[\mathrm{A\,m^{-1}}]$	
$\mathbf{J}$	Electric current density	$[\mathrm{A\,m^{-2}}]$	
$\mathbf{D}$	Electric displacement field	$[\mathrm{C\,m^{-2}}]$	
ρ_{el}	Free electric charge density	$[\mathrm{C\,m^{-3}}]$	
t	Time	[s]	
T	Period	[s]	$T = f^{-1}$
f	Frequency	[Hz]	$f = T^{-1}$
ω	Angular frequency	[Hz]	$\omega = 2\pi f$
μ	Magnetic permeability	$[\mathrm{H\,m^{-1}}]$	
μ_0	Permeability of vacuum	$[\mathrm{H\,m^{-1}}]$	$4\pi \times 10^{-7}\,\mathrm{H\,m^{-1}}$
ϵ	Electric permittivity	$[\mathrm{F\,m^{-1}}]$	
ϵ_0	Permittivity of vacuum	$[\mathrm{F\,m^{-1}}]$	$8.854187817... \times 10^{-12}\,\mathrm{F\,m^{-1}}$
ρ	Electric resistivity	$[\Omega\,\mathrm{m}]$	$\rho = \sigma^{-1}$
σ	Electric conductivity	$[\mathrm{S\,m^{-1}}]$	$\sigma = \rho^{-1}$
∇	Nabla operator	$[\mathrm{m^{-1}}]$	$\left[\frac{\partial}{\partial x}, \frac{\partial}{\partial y}, \frac{\partial}{\partial z}\right]^T$
i	Imaginary unit		$i^2 = -1$

Chapter 1

Introduction

Information of the spatio-temporal distribution of fluids in the subsurface is crucial information in various different applications ranging from the treatment of contaminated aquifers to geothermal energy production and the extraction of crude oil.
Thus, different geophysical techniques have been developed to monitor such fluid saturations. Most commonly seismic methods are used. Seismic methods allow to map changes in mechanical properties (density, pore pressure, Poisson's ratio etc.) in the subsurface. Although much progress has been made, discriminating between different types of pore fluids remains a challenging task.
The electrical resistivity of sedimentary rocks is mainly controlled by their porosity and the electrical conductivity of the pore fluids (Archie, 1942) as well as the fluid saturation. Thus, methods sensitive to the electrical resistivity of rocks are a promising tool for discriminating pore fluids of different resistivities. Therefore electromagnetic (EM) methods and in particular Controlled Source Electromagnetics (CSEM) became of increasing interest over the last decade in a wide range of settings from marine (e.g Orange et al., 2009) to land based (e.g Wirianto et al., 2010; Schaller, 2018) applications with increasing interest for the production of hydrocarbons.
In general, crude oil is considered to be an electrical insulator while the produced formation water and the injected brines are highly conductive, thereby providing a significant contrast in resistivity between oil-filled and fluid flushed or depleted sections of the oil bearing formations.
This thesis is part of a research project aiming to monitor the fluid saturation in an onshore oil field using land based CSEM with the focus on the improvement of simulation techniques and the necessary time-lapse inversion. Most of the work in this thesis builds on results obtained in (Tietze et al., 2015; Tietze et al., 2017), where in addition to other authors (e.g Streich, 2016) it has been shown that classical surface based horizontal transmitters and receivers do not provide enough resolution at reservoir level to monitor the change of fluid saturation. Thus alternative unconventional source-receiver layouts have been proposed, mainly including vertical electric dipole (VED) transmitters and receivers.
Vertical electric transmitters have been realised by injecting electric current into the ground via the steel casing of an abandoned well. Vertical receivers have been realised by the development of a novel vertical electric field sensor which has been installed and tested in a shallow borehole above an oil-field in northern Germany. Within the

framework of this project time-lapse data have been collected for conventional horizontal electric field data as well as VED transmitters and receivers. However, interpreting data obtained for vertical dipoles required the development of new modelling schemes which had been an essential part of this thesis. Thus this work is structured in the following chapters.

First of all the general methodology of the CSEM method including the pre-existing modelling and inversion tools are summarised in chapter 2 as they form the basis this work builds upon. Second the superordinated research project and its main results beyond the scope of this thesis are summarised in chapter 3. The bulk of this work is divided into three main chapters, discussing the implementation, results and implications of vertical electric sources, receivers and time-lapse inversion.

Boreholes are inevitably present in any oil field. These boreholes usually require steel-casings for stability and production purposes as well as protecting shallower sediments from contamination with the extracted oil and formation water. As steel is six orders of magnitude more conductive than the surrounding rock formations the pure presence of such oil-field infrastructure is likely to effect the response of the measured electric and magnetic fields. Thus in chapter 4 the effect of steel casings on the propagation of EM-fields is discussed. Modelling such effects however is not trivial due to their spatial unfavourable geometries. Therefore a new modelling methodology has been developed and implemented into the existing software. Chapter 4 summarises the new approach and shows how steel casings can be exploited as additional vertical dipole sources by either galvanic or inductive coupling to the transmitter.

As mentioned before various different authors found that the vertical electric field is the most sensitive EM-field component to thin resistive structures commonly associated with hydrocarbon reservoirs. Thus as part of the larger research project a novel vertical electric field receiver has been developed and installed in a shallow observation borehole. However, inversion of such receivers requires considerations of physical receiver dimensions which is commonly neglected in most modelling and inversion schemes. Thus in chapter 5 a novel modelling scheme is presented allowing to consider true receiver layouts in EM modelling and inversion.

Finally in chapter 6 developments for time-lapse inversion are presented and tested on synthetic data. Not only for classical surface based horizontal receivers but also considering vertical sources in the form of a galvanically coupled steel casing as well as vertical electric dipole receivers. Most work of the time-lapse inversion focused on the usage of non-smoothness constraint regularisations. In addition for reservoir monitoring applications lots of information can be feed into the inversion as a-priori knowledge or constraints. In order to overcome the non-uniqueness of the inverse problem, different additional constraints have been tested.

Finally the main results of this work are summarised and recommendations of potential future research projects in the field of EM reservoir monitoring is made.

Chapter 2

The Controlled Source Electromagnetics method

Controlled Source Electromagnetics (CSEM) is an electromagnetic (EM) geophysical method based on the diffusive propagation of electromagnetic fields in the subsurface. Sources of these fields are most commonly grounded electric dipole sources at surface and sometimes magnetic dipole sources in the form of current carrying loops. The resulting electric and magnetic fields are recorded at discrete locations at the earth's surface or in boreholes using induction coils for the magnetic fields and non-polarisable electrodes for the electric fields. The aim is to reconstruct the electrical resistivity structure of the subsurface from these measured fields.
Although CSEM was initially developed on land its main applications have been in marine environments (Streich, 2016). Only recently, it gained attention for land-based applications and especially for reservoir monitoring (Wirianto et al., 2010; Schamper et al., 2011; Schaller et al., 2018).

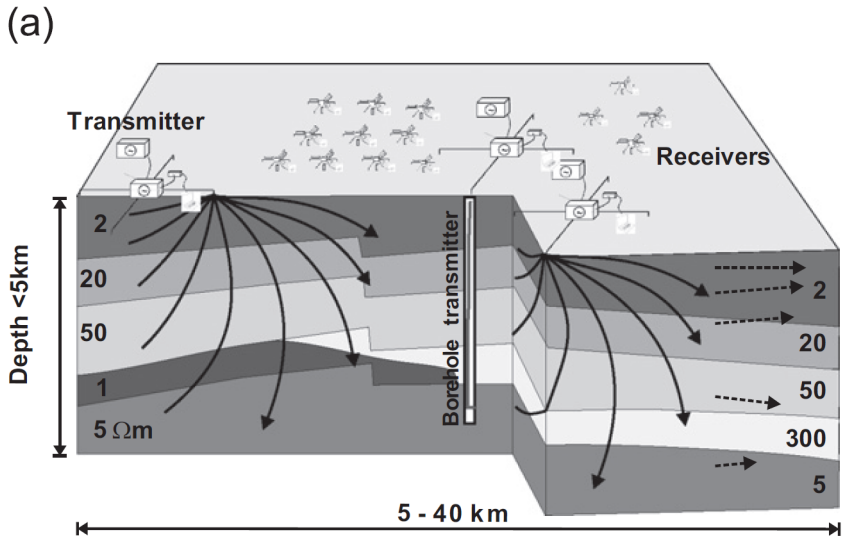

Figure 2.1: Sketch of CSEM method taken from Streich et al. (2010)

This section mainly aims to summarise the method, tools and procedures as they are available at German Research Centre for Geoscience (GFZ), since they form the basis of this work. For a more detailed introduction to CSEM on land see Streich (2016) and for a review on marine applications see Constable (2010). A review focusing more on numerical aspects and especially the inverse problem was given by Zhdanov (2010).

2.1 CSEM data acquisition and processing

CSEM relies on the measurement of electric and magnetic fields at discrete locations mostly at the earth's surface. Signals are recorded as time series and further processing results in CSEM transfer function (TF). These TFs are used as input data in the following inversion in order to obtain the resistivity structure of the subsurface. The methodology of obtaining these TFs from measured time series is described in detail in Streich et al. (2013).

The CSEM transmitter
The CSEM transmitter used by GFZ is composed of three grounded wires of $\approx 1\,\mathrm{km}$ length, all connected to one common grounding electrode (see Fig. 2.2). Currents on

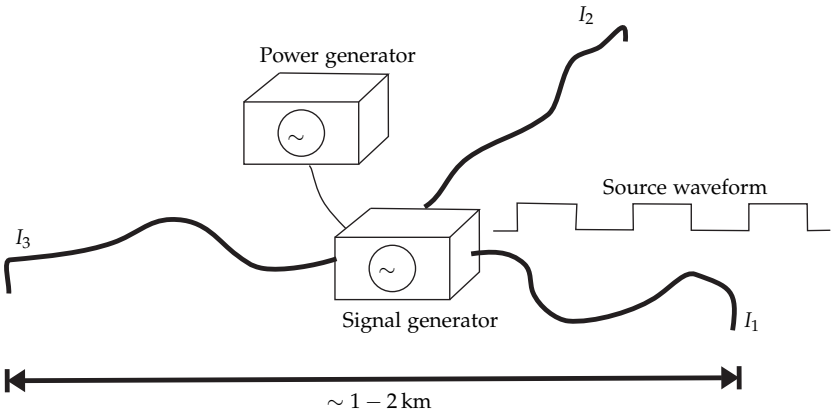

Figure 2.2: Sketch of the CSEM transmitter used by GFZ, modified after Streich et al. (2013).

each wire are shifted in phase by 120°. Therefore the sum of currents on each wire is always equal to zero. The source waveform can be chosen freely and is produced by a signal generator. The whole system operates on 560 V with a maximum current strength of 40 A.

EM field receivers
Time-series of the transmitted EM fields are recorded at receiver stations, mostly at the earth's surface. Variations of the three magnetic field components are recorded by the use induction coils. Two perpendicular grounded electric dipoles measure time-series of voltage differences. Voltages are then transferred into units of the electric field by dividing through the distance between the grounding points of the dipole.

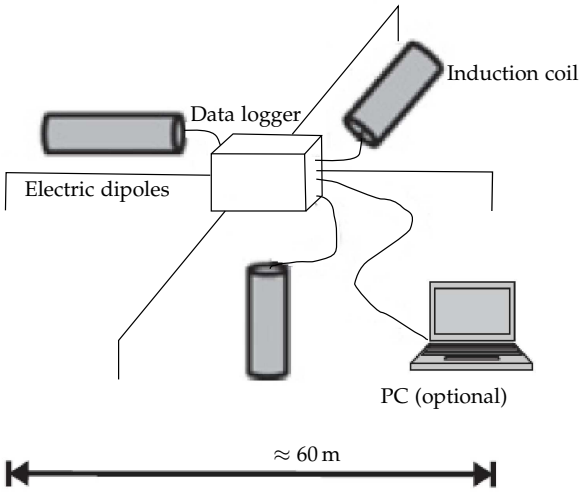

Figure 2.3: Sketch of an EM receiver station as it is used by GFZ, modified after Streich et al. (2013).

Grounding is ensured by the use of non-polarisable Ag-AgCl electrodes. Typical distances between the electrodes is in the order of 60 m. Fig. 2.3 shows a summarised sketch of one receivers station. Both sensor types electrodes as well as induction coils are buried to minimize the effect of changing temperatures as well as moving of the sensors due to wind. Directions are typically determined by magnetic bearing, with the x-direction pointing towards magnetic North and the y-direction towards magnetic East and the z-axis pointing downwards.

Data processing
As the current on all wires of the transmitter allways sums to zero, currents on each wire are not independent of each other and it is possible to relate each measured field component (F) in frequency domain at one receiver station to any two source currents of the transmitter by a set of two independent TFs (T_{ij}^{F}) as shown in eq. 2.1.

$$\begin{bmatrix} T_{13}^{E_x} & T_{23}^{E_x} \\ T_{13}^{E_y} & T_{23}^{E_y} \\ T_{13}^{E_z} & T_{23}^{E_z} \\ T_{13}^{H_x} & T_{23}^{H_x} \\ T_{13}^{H_y} & T_{23}^{H_y} \\ T_{13}^{H_z} & T_{23}^{H_z} \end{bmatrix} \begin{bmatrix} I_1 \\ I_2 \end{bmatrix} = \begin{bmatrix} E_x \\ E_y \\ E_z \\ H_x \\ H_y \\ H_z \end{bmatrix} \tag{2.1}$$

Each T_{ij}^{F} can be interpreted as the field component F produced by a unit current on wire i and a negative unit current on j. TFs are obtained from time series by the use of robust statistical analysis following Streich et al. (2013).

2.2 Existing modelling and inversion algorithms

This work mostly builds on a number of pre-existing modelling and inversion programs which had been extended and optimised to be suitable for monitoring applic-

ations. The 3D CSEM inversion is described in detail in Grayver et al. (2013). The forward modelling within the inversion is based on Streich (2009).

2.2.1 Forward modelling

The fundamental equations describing the behaviour of EM fields are given by Maxwell's equations

$$\nabla \times \mathbf{E} = -\frac{\partial \mathbf{B}}{\partial t} \tag{2.2a}$$

$$\nabla \times \mathbf{H} = \mathbf{J} + \frac{\partial \mathbf{D}}{\partial t} \tag{2.2b}$$

$$\nabla \cdot \mathbf{B} = 0 \tag{2.2c}$$

$$\nabla \cdot \mathbf{D} = \rho_{el} \tag{2.2d}$$

together with Ohm's law and the material relations,

$$\mathbf{J} = \sigma \mathbf{E} \tag{2.3a}$$

$$\mathbf{B} = \mu \mathbf{H} \tag{2.3b}$$

$$\mathbf{D} = \epsilon \mathbf{E}. \tag{2.3c}$$

After applying a fourier transform one can obtain the curl-curl equation for the electric field for the source current density $\mathbf{J}_s$

$$\nabla \times (\nabla \times \mathbf{E}) + i\omega\mu\sigma\mathbf{E} = \mathbf{J}_s. \tag{2.4}$$

The forward modelling relies on solving the curl-curl equation (eq. 2.4) using a secondary field approach. The total electric field is split into a sum of a primary ($\mathbf{E}_p$) and a secondary field ($\mathbf{E}_s$). The primary field is the analytic solution of equation 2.4 for a layered or homogeneous halfspace conductivity distribution σ_p using Streich and Becken (2011b). Once the primary electric field has been determined, the secondary electric field is given as the solution of the following partial differential equation

$$\nabla \times (\nabla \times \mathbf{E}_s) + i\omega\mu\sigma\mathbf{E}_s = -i\omega\mu(\sigma - \sigma_p)\mathbf{E}_p. \tag{2.5}$$

This equation is solved using a Finite Difference (FD) scheme on staggered grids. With *E*-fields being defined on the edge midpoints as illustrated in Fig. 2.4.

After discretisation, one obtains a system of linear equations which is solved using a direct forward solver.

$$\mathbf{A}\mathbf{E}_s = \mathbf{b} \tag{2.6}$$

The response (or field value) at each receiver is than obtained by interpolating the secondary electric field to the receiver location using operators $\mathbf{Q}_E$ and $\mathbf{Q}_H$ respectively.

$$\mathbf{E}_{rec} = \mathbf{E}_{rec,p} + \mathbf{Q}_E\mathbf{E}_s \tag{2.7}$$

$$\mathbf{H}_{rec} = \mathbf{H}_{rec,p} + \mathbf{Q}_H\mathbf{E}_s \tag{2.8}$$

In addition to the interpolation $\mathbf{Q}_H$, also contains a discrete approximation to the curl operator in 2.2a.

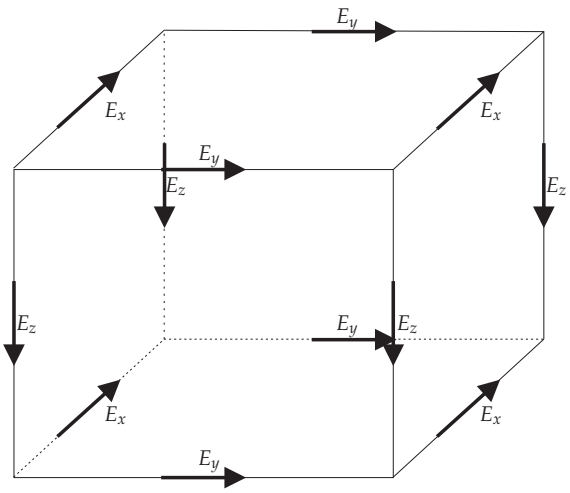

Figure 2.4: Sketch of staggered FD grid where the electric field is evaluated at the edge midpoints.

2.2.2 Inversion

The inversion as it is implemented in Grayver et al. (2013) aims to minimise the following penalty function.

$$\varphi = \frac{1}{2}\|\mathbf{W}_d(\mathbf{f}(\mathbf{m}) - \mathbf{d})\|^2 + \lambda R(\mathbf{m} - \mathbf{m}_{ref}) \tag{2.9}$$

$\mathbf{d}$ represents the measured data vector of electric or magnetic field values or TFs respectively. $\mathbf{m}$ is the model vector containing conductivity values of each FD grid cell. Data and model parameters are linked by the forward operator $\mathbf{f}$ which evaluates predicted data values for a given conductivity model. Since the amplitude of the data varies over several orders of magnitude an additional diagonal data weighting matrix $\mathbf{W}_d$ is given by

$$\mathbf{W}_d = \mathrm{diag}\left(\frac{1}{|d_i|\epsilon_i + \gamma}\right). \tag{2.10}$$

It allows for compensation of different amplitudes of each data point. In addition the influence of noisy data can be reduced by using relative data errors ϵ_i obtained from CSEM processing. γ marks the absolute noise floor to prevent the inversion being dominated by small data values.
Since any inversion is mathematically ill-posed, an additional regularisation term is needed to ensure convergence and give the possibility to add additional a-priori information. R is the regularisation functional and can be regarded as additional constraints to the obtained model. Several different choices of regularisation operators are implemented. The most common constraint is that resistivity values should vary smoothly between neighbouring cells. Different regularisation operators are discussed in detail in section 6.3. A user defined reference model $\mathbf{m}_{ref}$ can be added for additional constraints. Data functional and model regularisation are weighted by the regularisation parameter λ which controls the influence of model regularisation.
The penalty function from equation 2.9 is minimised following an iterative Gauss-Newton algorithm. In each inversion iteration, an update $\mathbf{\Delta m}$ of the current model

vector is evaluated by solving the following system of normal equations

$$\left[\Re\{\mathbf{J}^H\mathbf{W}_d\mathbf{W}_d\mathbf{J}\} + \lambda\mathbf{P}^T\mathbf{P})\right]\boldsymbol{\Delta}\mathbf{m} = \Re\{\mathbf{J}^H\mathbf{W}_d\left(\mathbf{d} - \mathbf{f}(\mathbf{m})\right)\} - \lambda\mathbf{P}^T\mathbf{P}\left(\mathbf{m} - \mathbf{m}_{ref}\right). \quad (2.11)$$

Here $\mathbf{P}^T\mathbf{P}$ stands for the partial derivatives of R with respect to the model parameters.

$$\nabla_m R\left(\mathbf{m} - \mathbf{m}_{ref}\right) = \mathbf{P}^T\mathbf{P}\left(\mathbf{m} - \mathbf{m}_{ref}\right) \quad (2.12)$$

The Jacobian or the sensitivity of the forward operator is given by

$$\mathbf{J} = \nabla_m\mathbf{f}(\mathbf{m}) \quad (2.13)$$

$$= \mathbf{Q}\mathbf{A}^{-1}\mathbf{G} \quad (2.14)$$

with $\mathbf{G}$ given as

$$\mathbf{G} = \Big[\left(\frac{\partial\mathbf{b}}{\partial m_1} - \frac{\partial\mathbf{A}}{\partial m_1}\mathbf{E}_{s,grid}\right), \left(\frac{\partial\mathbf{b}}{\partial m_2} - \frac{\partial\mathbf{A}}{\partial m_2}\mathbf{E}_{s,grid}\right), \ldots , \left(\frac{\partial\mathbf{b}}{\partial m_{N_m}} - \frac{\partial\mathbf{A}}{\partial m_{N_m}}\mathbf{E}_{s,grid}\right)\Big] \quad (2.15)$$

The normal equations are solved using conjugated gradients (CG). The iterative process is continued until the normalised root mean squared error (nRMS) is below a user defined threshold or the maximum number of inversion iterations is reached.

$$\text{nRMS} = \sqrt{\frac{1}{N}\left[\mathbf{W}_d(\mathbf{f}(\mathbf{m}) - \mathbf{d})\right]^H\left[\mathbf{W}_d(\mathbf{f}(\mathbf{m}) - \mathbf{d})\right]} \quad (2.16)$$

Ideally misfits should be normally distributed and the nRMS should converges to 1.

2.3 Radiation pattern of horizontal electric dipole transmitters

The physics of CSEM is mainly controlled by the characteristics of the EM field emitted by the transmitter. In order to understand many of the effects discussed in the following chapters it is crucial know the basic radiation pattern of the electric field produced by a horizontal electric dipole (HED) transmitter at surface.
Fig. 2.5 sketches the general distribution of the three electric field components emitted by a HED source at the surface of a homogeneous halfspace. Fig. 2.5 a)-c) shows map views of the different field components near the surface. All three components show different characteristics. Highest amplitudes are generally found at the transmitter and are decreasing with distance. Decrease is not uniform but strongly dependent on the component and the orientation to the transmitter.
For an x oriented dipole the x-component of the electric field (cf. Fig. 2.5 a) will have highest amplitudes in inline as well as broadside direction to the transmitter with opposite phases in the two transmitter orientations. Between these maxima discrete lines of zero crossing marks also a change in polarity (change in colour from red to blue).
The y-component on the other hand (cf. Fig. 2.5 b) has maximum amplitudes in an approximately 45° angle to the transmitter. Zero crossings are found in inline as well

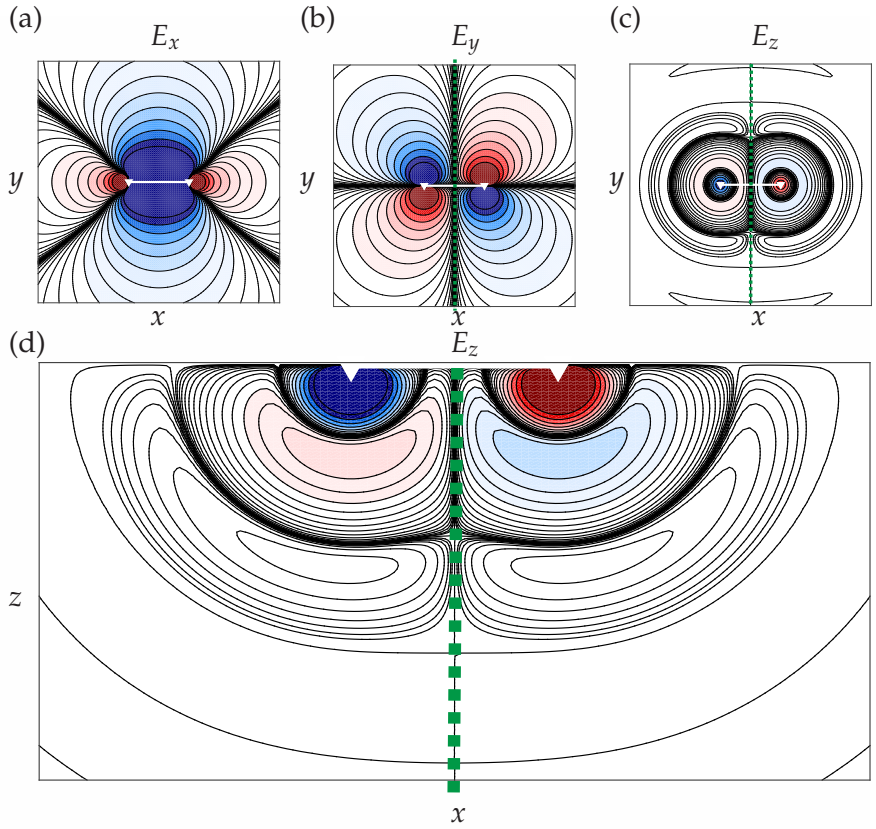

Figure 2.5: Schematic radiation pattern of different field components emitted by a HED source at the surface of a homogeneous halfspace (see also Patzer et al., 2017b). (a) Map view of the x component of the electric field at surface. (b) Map view of the y component of the electric field at surface. (c) Map view of the z component of the electric field just below the surface. (d) Distribution of the E_z component along a XZ slice through the transmitter position. In all figures the source-dipole is shown as white line. Colour saturation indicates the amplitude of the emitted electric field and the colour marks the phase angles. A green line indicates the symmetry axis and zero crossing of the field component in broadside direction to the transmitter.

as broadside direction. Maximum values of the y-component correspond to the zero crossings of the x-component shown in a).
Maximum values of the z-component of the electric field is found just below the two grounding points of the transmitter (cf. Fig. 2.5 c) with again opposite polarity. The most prominent zero crossing is marked as green line forming a YZ oriented plane perpendicular to the transmitter direction.
The vertical electric field vanishes directly at the earths surface, as shown in Fig. 2.5 d). Furthermore the radiated field forms quarter shells with oscillating polarity. According to the skin effect the amplitude of the field decreases with depth, while the volume of the shells increases with depth and distance to the transmitter.

Chapter 3

Electromagnetic monitoring of the Bockstedt oil field

This thesis is part of a research project called Enhanced Oil Recovery (EOR) monitoring, a collaboration of German Research Centre for Geoscience (GFZ) with Wintershall Holding GmbH, Kassel (Germany), a medium sized German oil company. During the production of crude oil, it is common practice to inject fluids (brines, formation water, CO_2, etc.) into the hydrocarbon bearing formation. Aiming to push the oil from the injection well towards extraction wells and hence increase oil production. This technique is especially used to increase the amount of recoverable oil from the reservoir and is therefore commonly referred to as Enhanced Oil Recovery. To optimise this process and reduce the amount of expensive drilling operations, it is crucial to know the temporal and spatial distribution of the injected fluids and the oil in place.
The electrical resistivity of these injected fluids is commonly up to two orders of magnitude lower then the electrically resistive oil ($\approx 1\,\Omega\,\mathrm{m}$ vs. $\approx 100\,\Omega\,\mathrm{m}$). Therefore, electromagnetic (EM) methods and especially Controlled Source Electromagnetics (CSEM) have become of interest for monitoring this replacement of resistive oil by conductive brines mainly in a marine setting (e.g. Orange et al., 2009) and more recently also on land (e.g. Wirianto et al., 2010; Schamper et al., 2011; Schaller, 2018).
Over the course of six years starting in 2012, the project covered the entire research chain ranging from hardware development, theoretical studies on optimal survey design, data acquisition, interpretation as well as the development of a numerical framework for time-lapse inversion. Most technological developments have been applied in several field surveys in the Bockstedt oil field, an actively producing onshore oil field in Northwest Germany.
This section summarises some main results and findings of this project outside the scope of this thesis. Some of these results had been of great influence on the development of this thesis.

3.1 The Bockstedt oil field

The Bockstedt oil field is located 40 km south of the city of Bremen at the northern edge of the Lower Saxony Basin (see Fig. 3.1). The Lower Saxony Basin is the most important oil province in Northern Germany (Betz et al., 1987). As being part of

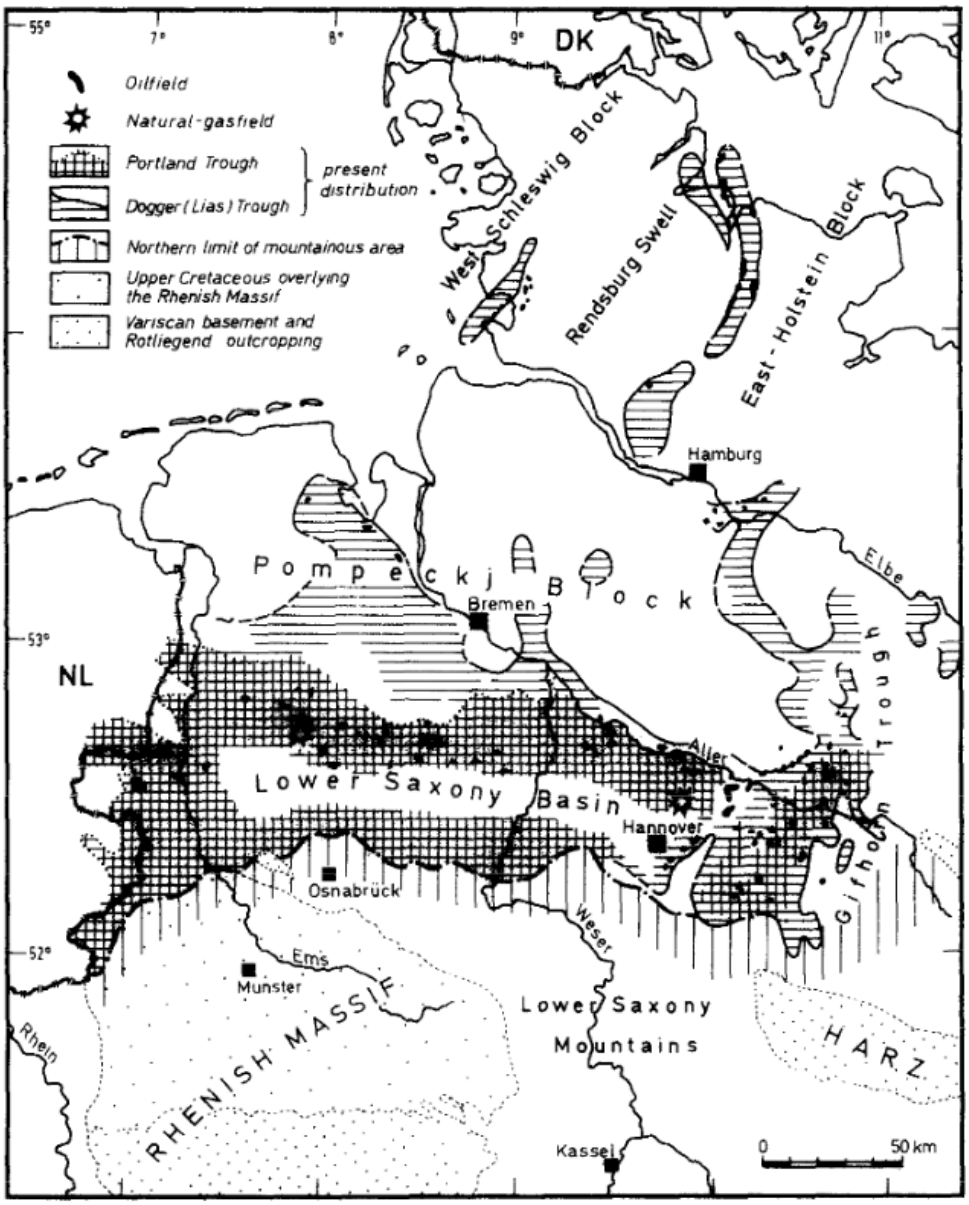

Figure 3.1: Map of the Lower Saxony Basin and the location of associated oil and gas fields (Modified after Betz et al., 1987).

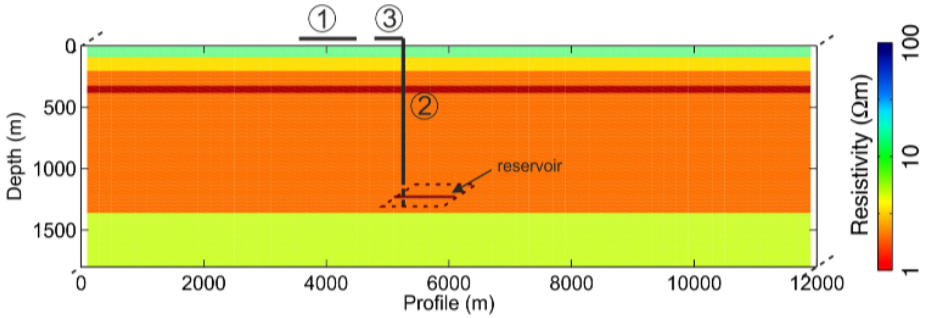

Figure 3.2: 3D resistivity model used to model the expected time-lapse differences (taken from Tietze et al., 2015).

the central European basin system it was formed by rifting processes caused by the break up of Pangea in late Jurassic to early Cretaceous. Due to subsidence it was filled by series of marine, lacustrine and hypersaline sediments of the late Jurassic and early Cretaceous. Today the sediments of the Lower Saxony Basin reach 2400 m thickness. Hydrocarbon source rocks of the lower Jurassic can be found in the entire basin. Their thickness varies between 15-30 m. The reservoir rocks are mostly made up of siliciclastic sandstones. Migration into the reservoir rocks took place from upper Cretaceous to Quaternary times. The trap structure of the Bockstedt oil field is formed by a local block faulted high. The recoverable depth of the oil field is in about 1200 m depth with varying thickness between 3 to 35 m.
The Bockstedt oil field has been discovered in 1954 and is in production ever since. After the primary oil production highly saline produced formation water has been injected into the formation during the secondary oil production phase, starting from 1959 onwards. Today during the tertiary oil production phase polymers are added to the injected fluids to increase the amount of recoverable oil even further.

3.2 2D Magnetotelluric survey and CSEM modelling study

The general aim of this research project is to show that it is possible to detect the change in the resistivity structure inside the reservoir due to oil production by repeated measurements (time-lapse surveys) across the oil field. To examine whether CSEM is generally able to resolve resistivity changes in such a deep and thin reservoir, a modelling study has been carried out using background resistivity models obtained from Magnetotelluric (MT) measurements across the oil field. Detailed results are presented in Tietze et al. (2015) and Tietze et al. (2017).
The used background structure is shown in Fig. 3.2. It is made of the typical highly conductive mainly layered sediments of the North German basin. Close to surface, resistivity is in the order of 12 Ω m and is generally decreasing with depth. In approximately 300 m depth, a highly conductive layer of 1 Ω m and 100 m thickness was found. Below this layer, resistivities vary only little between 3 and 5 Ω m. The obtained conductivity structure agrees well with a borehole log from the study area.
Based on this background conductivity structure, a CSEM modelling study has been performed. CSEM responses have been calculated for two identical source receiver

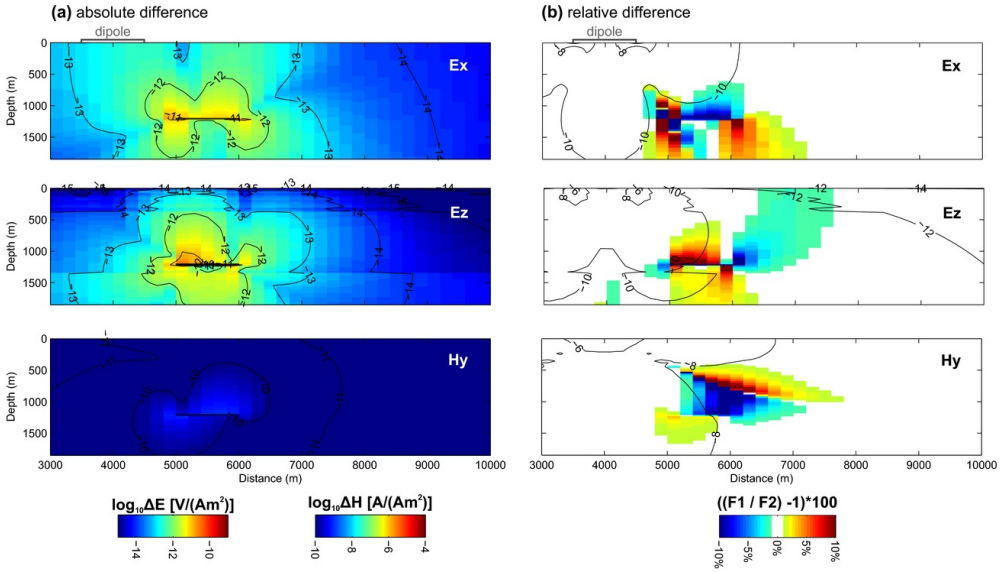

Figure 3.3: Absolute and relative differences of electric and magnetic field components for a frequency of 0.1 Hz (taken from Tietze et al., 2015). Transmitter is a 1 km long grounded HED at surface. Shown is the same slice through the 3D model as in Fig. 3.2.

setups and changing resistivities of a 3D reservoir ($1000 \times 1000 \times 15\,\mathrm{m}^3$) in 1200 m depth. The two states of the reservoir resemble a partly depleted reservoir of $16\,\Omega\,\mathrm{m}$ and a fully brine flushed state of $0.6\,\Omega\,\mathrm{m}$. Aim of this study was to test whether the expected differences between these CSEM time-lapse responses are large enough to be above the expected noise floor of this region. In addition it was aimed to find source receiver configurations that are most sensitive towards these changes.

The main result of this study is, summarised in Fig. 3.3. It shows absolute and relative differences of different EM field components for one frequency in inline direction and depth between the two modelled scenarios. Only three components are shown as the E_y, H_x and H_z component are zero in inline direction to an horizontal electric dipole (HED) source (cf. Fig. 2.5). In order to be able to resolve changes in the responses absolute differences (left panel) need to be above the background noise floor of the study area and the relative difference should be above 1% (right panel).
For classical HED transmitters at surface sizeable changes in EM-field amplitudes above the 1% threshold (coloured areas in the right panel of Fig. 3.3) are only reached at depth in close proximity of the reservoir. This lead to the conclusion that monitoring of oil saturation using only conventional surface based CSEM measurements of horizontal fields will not be feasible. However, the figure also shows that measurements of the vertical electric field near the surface (see the middle panel in Fig. 3.3) may provide enough resolution to the changes in reservoir depth.

Sensitivity increases above the estimated noise floor even when measuring horizontal electric fields at surface if one is using vertical electric dipole (VED) sources. An easy realisation of such vertical sources can be achieved by attaching the CSEM transmitter to the metal casing of an existing well, resulting in a source comprising a horizontal as well as a vertical component (HV-source, transmitter 3 in Fig. 3.2).

The use of such energised steel casings as source requires the description of the source current along the casing as input into the modelling. According to Yang et al. (2009) currents along such energised casings decay exponentially with depth. Thus the current is modelled as

$$I(z) = I_0 \left(1 - \frac{\log_{10} z}{\log_{10} L}\right)^s, \tag{3.1}$$

with I_0 being the maximum current at surface, L the total length of the casing and s a scaling factor controlling how fast currents are decreasing with depth.
Fig. 3.4 shows relative and absolute differences of field amplitudes at surface along a profile in inline direction to the transmitter for a range of frequencies using an HV-source for various scale parameters.
White areas in the upper part of each panel at the right hand side shows that regard-

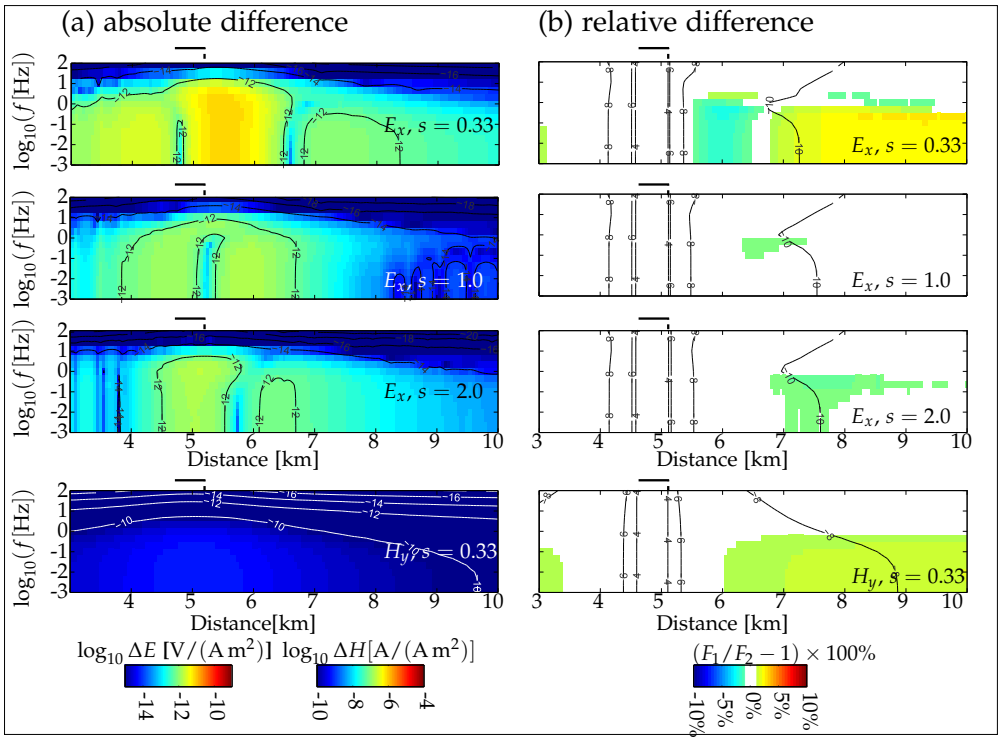

Figure 3.4: Absolute and relative differences of E_x and H_y components at surface along a profile in inline direction to the transmitter for a range frequencies (taken from Tietze et al., 2017). Transmitter is a HV-source with a 1 km long grounded HED component connected to a 1.3 km long steel-cased well. Shown is the same slice through the 3D model as in Fig. 3.2.

less of the scale parameter frequencies above 1 Hz do not provide enough resolution at reservoir depth. Coloured areas also show that, using an HV-source instead of the classical surface based transmitter relative differences are above the 1% threshold over large parts of the shown profile for the E_x component as well as the H_y component. However, absolute differences of the H_y component is below the assumed noise floor of $10^{-9}\,\mathrm{A\,A^{-1}\,m^{-2}}$, while absolute difference of E_x components exceed the noise floor of $10^{-14}\,\mathrm{V\,A^{-1}\,m^{-2}}$ over large parts of the shown profile. This lead to the conclusion

that surface based measurements of the horizontal electric field may be suitable for reservoir monitoring if combined with an HV-source and the scaling factor in the range of 0.33.
Similar improvements are obtained regarding the resolution capabilities of measuring the vertical electric field in combination with an HV-source. Fig. 3.5 shows results in the same way as in Fig. 3.3. Depending on the scaling parameter the relative difference

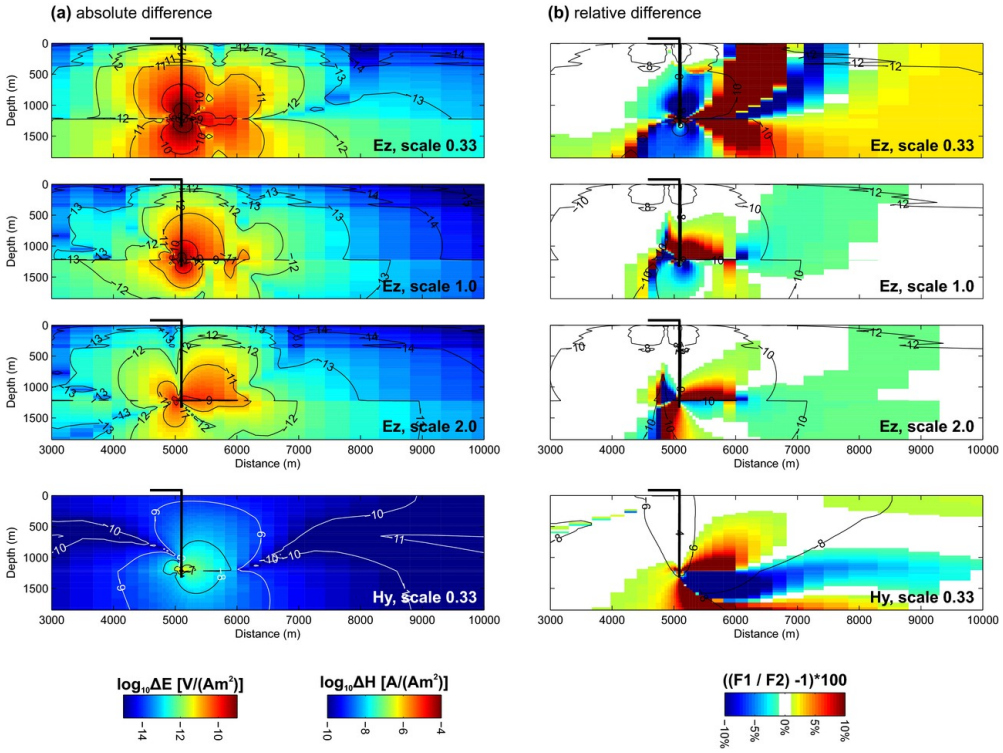

Figure 3.5: Absolute and relative differences of electric and magnetic field components for a frequency of 0.1 Hz (taken from Tietze et al., 2017). Transmitter is a HV-source with a 1 km long grounded HED component connected to a 1.3 km long steel-cased well. Shown is the same slice through the 3D model as in Fig. 3.2.

of the shallow vertical electric field increases to more than 5% using an HV-source. Sensitivity of the H_y component increases too but absolute differences do not significantly exceed the assumed noise floor.
These general findings that vertical electric sources and receivers provide highest resolution capabilities towards thin resistive structures is in agreement with other publications (e.g. Streich, 2016).

3.3 CSEM Field surveys

The findings of the modelling study have been applied in three CSEM field surveys in three consecutive years (2014,2015 and 2016) in the Bockstedt oil field. The setup of all surveys is summarised in Fig. 3.6. Four transmitters (marked by red lines) have been installed in all three surveys. To obtain the desired HV-source discussed before,

one leg of the CSEM transmitter S01 has been galvanically attached to the casing of a 1.3 km abandoned injection well Bo-23. As discussed before modelling such kind of HV-source requires the knowledge of the current distribution along the attached steel-cased well which is exponentially decaying with depth and the rate of decay is depending on the frequency and the resistivity of the surrounding rock formations. Evaluating the exact current distribution along such steel-cased wells has been shown to be a challenging task. Therefore, numerical considerations of steel-casings in CSEM was a major topic of this PhD thesis and is discussed in detail in chapter 4.

Horizontal electric fields have been recorded at 25-27 receiver stations (shown as

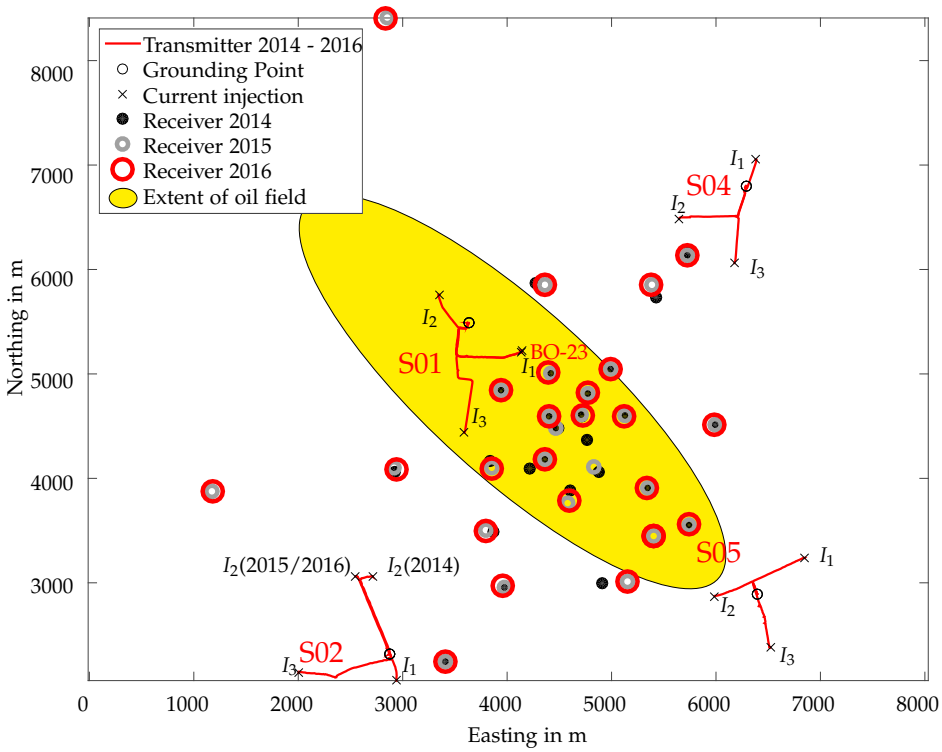

Figure 3.6: Setup of all CSEM field surveys across the Bockstedt oil field. Each survey consisted of four transmitters and 25 (2014) and 27 (2015/2016) receivers respectively. Transmitters as well as receivers had to be reinstalled for each survey. Changing receiver position occurred due to various reasons, mainly due to land access and newly constructed windmills. Current electrode I_2 of transmitter S02 was moved due to saftey issues to avoid an additional crossing of a road.

red,grey and black circles). The majority of the receiver stations has been redeployed within ≈ 10 m of the original 2014 position.

As discussed before and shown in Tietze et al. (2017) measurements of the vertical electric field provide highest sensitivity towards changes in resistivity of the reservoir. Thus a novel vertical electric field sensor has been developed and installed in a specially drilled 200 m deep well in the Bockstedt oil field. As mentioned in Tietze et al. (2018b), the vertical electric field near the surface is two to three orders of mag-

nitude smaller than the classical horizontal field components. This requires rather long measurement dipoles (100 m-200 m). Accurate modelling of the response of such receivers requires consideration of the dipole dimension as well as orientation of these receivers, which is commonly neglected for conventional horizontal electric field receivers. Implementation of these type of receivers is described in section 5 and was another major topic this thesis.
A detailed analysis of the data had shown that despite excellent repeatability between the surveys no significant change in the data is obtained (Tietze et al., 2018b). Thus the focus of this work is not in the interpretation of the measured data but rather on the numerical aspects required to interpret such kind of data in general. However most numerical experiments shown in the following chapters rely on the field setups and use variations of a conductivity model representative for the study area.

Chapter 4

Steel casings

In mature oil fields there exists a large number of steel-cased wells. For example there are more than 80 wells in the Bockstedt oil field. Modelling the presence of these metal casings remains a challenging task for Finite Difference (FD) and even for Finite Element modelling, due to the high resistivity contrast of steel ($\approx 10^{-6}\,\Omega\,\mathrm{m}$) to the surrounding rock ($\approx 10\,\Omega\,\mathrm{m}$) in addition to their unfavourable dimensions in comparisons to the geological formations one wants to observe (thin but vertical extended). First theoretical considerations on the effect of steel-cased wells have been described by Wait and Hill (1973). Main result of most published studies investigating the effect of steel-cased wells on electromagnetic (EM) data is that despite their small size in horizontal dimensions, their influence on the EM field distribution in the subsurface can be significant (e.g. Commer et al., 2015).
However, the presence of metal casings can also be exploited. Steel casings can be used as source extension by galvanic connection of the CSEM transmitter to the casing (cf. ection 3), in order to allow more energy to be injected into ground and hence increase sensitivity at depth. First field surveys exploiting the presence of steel-cased wells have been conducted in the Bockstedt oil field (see section 3) and the Hontomín Carbon Capture and Storage (CCS) site ("Advances in Electromagnetic Survey Instrumentation and the Use of a Cased Borehole for Imaging a Deep Formations"; Tietze et al., 2015; Vilamajó et al., 2015). However, accurate descriptions of such sources is not trivial since the current along the casing decreases exponentially with depth whose rate is tightly coupled to the resistivity of the surrounding formations as shown in Yang et al. (2009). Most steel-cased wells are considered vertical (at least in onshore applications), therefore steel casings used as source extensions can be regarded as easy realisation of vertical electric dipole (VED) sources. As demonstrated in Streich (2016) using vertical sources or receivers is most beneficial for resolving layered resistive structures.
Therefore, a major topic of this thesis has the investigation of the effect of steel casings on Controlled Source Electromagnetics (CSEM) data and the development and the implementation of an efficient way to include their effect into the existing 3D modelling and inversion codes including theri mutual interaction. This chapter describes the implemented algorithm and shows the main observed effects of steel casings on EM data as well as during the inversion.

4.1 Finite element modelling

In order to investigate the effect of inductively coupled (passive) steel-cased wells on CSEM data, I performed extensive finite element modelling using the software package Comsol multiphysics. The main results are shown in the following scenario. The transmitter-borehole geometry is shown in Fig. 4.1. Transmitter is a 1 km grounded

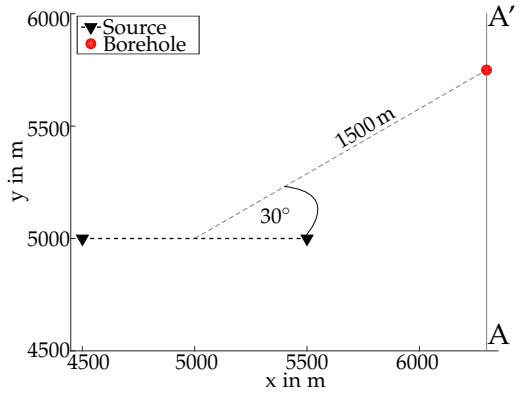

Figure 4.1: Map view of the source-borehole geometry used for investigating the borehole effect with Finite Element modelling.

horizontal electric dipole (HED) source. The borehole is placed at an angle to the transmitter axis to avoid being positioned in zero crossings of any field direction. Due to computational limitations, the casing was approximated as full cylinder of 1 m radius. The casing itself is perfectly vertical and reaches from surface to 1000 m depth. To account for the large horizontal casing dimensions compared to real world steel-cased wells (1 m radius full cylinder versus 0.2 m radius with 2 cm wall thickness) I decreased the conductivity of the casing from $5 \times 10^6\,\mathrm{S\,m^{-1}}$ (typical value of steel) to $1 \times 10^4\,\mathrm{S\,m^{-1}}$. For simplicity, I started modelling a $10\,\Omega\,\mathrm{m}$ homogeneous halfspace conductivity structure.
Due to the high resistivity contrast between the casing and the surrounding formations the grid cells describing the cylinder had to be discretised rather fine, having volumes in the order $0.0630\,\mathrm{m}^3$. The final mesh consisted of 1 010 096 tetrahedrons.
Fig. 4.2 shows results for a frequency of 10 Hz as the relative difference of the electric field distribution for two scenarios. One where the effect of the steel-cased well was taken into account and an undisturbed scenario neglecting the presence of the casing. Differences are confined within a radius of approximately 500 m around the borehole. However within this radius the relative difference exceeds $\pm 100\,\%$. Considering that in oil fields there are tens or hundreds of steel-cased wells in close proximity to each other it is easy to see that this effect is significant and has to be taken into account. The anomalous electric field at $y = 5000\,\mathrm{m}$ corresponds to the zero crossing of the undisturbed field (see section 2.3) as indicated by the high density of isolines.
The shape of the anomalous electric field resembles the shape of an additional VED source. Due to the shape of the borehole (thin and vertical extended) anomalous currents inside the casing are confined to the borehole trajectory, effectively acting as additional vertical dipole sources. The general idea obtained from this finite element

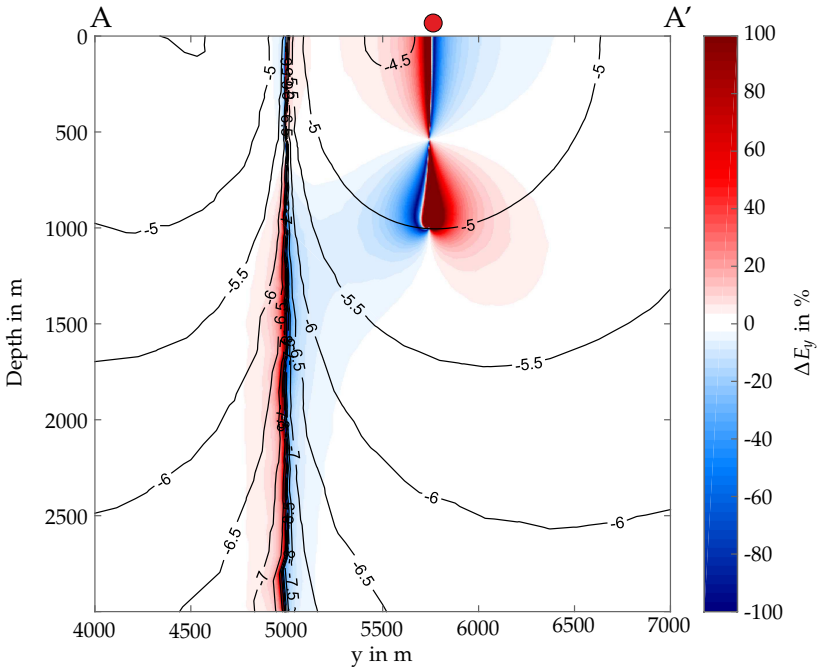

Figure 4.2: Anomalous electric field in $y-$direction due to the presence of the steel-cased well, shown for the scenario in Fig. 4.1 along the indicated profile AA′. The red circle indicates the lateral position of the steel casing. The $\log_{10}$ of absolute values of the undisturbed electric field is shown by isolines.

modelling study is that one can replace the casing by an additional VED source.

4.2 Implementation into CSEM modelling and inversion

In this section I summarise the implementation of steel-cased wells into the CSEM modelling and inversion program by Grayver et al. (2013) which is mainly following the methodology described in Patzer et al. (2017b). To obtain the current strength of the substitute dipole sources I expanded an approach given by Tang et al. (2015) to allow for mutual interaction between multiple wells. The general approach is by itself an implementation of the Method of Moments approach (Harrington, 1968).
In this algorithm, each steel-cased well gets subdivided into a number of segments assuming that each segment has uniform inner (r_i) and outer radius (r_a) and a constant conductivity of the casing (σ_c). Fig. 4.3 shows a sketch of one of these segments.

The response at the centre point $(x_i, y_i, z_{c,i})^T$ of one segment i can be expressed as the sum of a background field produced by the CSEM transmitter neglecting the presence of any steel casings and the scattered electric field produced by each casing segment $1 \leq j \leq N$. Similar to a secondary field approach.

$$\mathbf{E}(x_i, y_i, z_{c,i}) = \mathbf{E}^{bg}(x_i, y_i, z_{c,i}) + \sum_{j=1}^{N} \mathbf{E}^{j}(x_i, y_i, z_{c,i}) \tag{4.1}$$

One can rewrite the response of each single segment using Green's tensors. Following

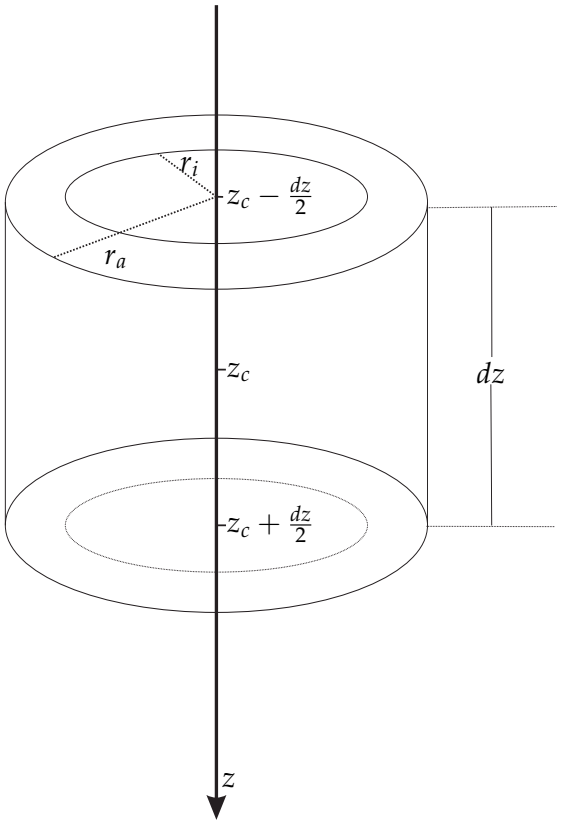

Figure 4.3: Sketch indicating the dimensions of one casing segment (taken from Patzer et al., 2017b).

Einstein's sum convention we get,

$$E_l^j(\mathbf{r}) = \iiint J_k(\mathbf{r}')\Gamma_{l,k}(\mathbf{r},\mathbf{r}')dV';\ l,k \in (x,y,z). \tag{4.2}$$

$\Gamma_{l,k}(\mathbf{r},\mathbf{r}')$ describes one element of the Green's tensor. Each element resembles the l component of the electric field at position $\mathbf{r}$ produced by a unit dipole source oriented in k-direction at position $\mathbf{r}'$. $J_k(\mathbf{r}')$ represents the current density at $\mathbf{r}'$ in k direction. If one is now assuming a constant current density on each segment one can rewrite eq. 4.1 as following:

$$\frac{J_l(\mathbf{r}_i)}{\sigma_c} = E_l^{bg}(\mathbf{r}_i) + \sum_{j=1}^{N} J_k(\mathbf{r}_j) \iiint \Gamma_{l,k}(\mathbf{r}_i,\mathbf{r}')dV_j', \tag{4.3}$$

which can be reformulated into the system of linear equations.

$$\mathbf{AJ} = \mathbf{E}^{bg} \tag{4.4}$$

Where matrix $\mathbf{A}$ contains coupling coefficients between current densities of each casing segment in each direction. The vector $\mathbf{J}$ describes the current density on each casing in each direction and $\mathbf{E}^{bg}$ is the vector of the background electric field in all directions at the centre point of each segment. Once this system of equations is solved,

the current strength of each substitute dipole is given by

$$\mathbf{I} = \pi(r_a^2 - r_i^2)\mathbf{J}. \tag{4.5}$$

The current strength can than be used to calculate an update of the background field to take the effect of steel casings into account.

4.2.1 Calculation of coupling coefficients

The calculation of the entries of the coefficient matrix **A** requires integration of Green's tensors. However a closed formula of the Green's tensor is only available for simple conductivity structures. Therefore I follow the approach by Tang et al. (2015) and limited the general 3D conductivity to a homogeneous halfspace approximation. Green's tensor derivation for the homogeneous halfspace is found in Raiche (1974). As a second assumption I limited the implementation to first order effects of steel-cased wells and assume boreholes to be perfectly vertical, neglecting integrations over all components except the Γ_{zz} which is given by

$$\Gamma_{zz}(x, y, z; x', y', z') = \frac{1}{4\pi\sigma_b}\int_0^\infty \frac{\lambda^3}{s} J_0(\lambda\nu)(e^{-s|z-z'|} - e^{-s(z+z')})d\lambda. \tag{4.6}$$

σ_b is the background conductivity of the halfspace, $s = \sqrt{\lambda^2 - i\omega\mu_0\sigma_b}$ and $\nu = \sqrt{(x-x')^2 + (y-y')^2}$ is the horizontal distance between source and test point. J_0 refers to the Bessel function of the first kind. Analytic integration for the diagonal elements of **A** as well non-diagonal elements of coupling coefficients within the same casing are given by Tang et al. (2015). Diagonal elements are

$$\begin{aligned} A_{ii} = \frac{1}{\sigma_c} &- \frac{r_a}{2\sigma_b}\int_0^\infty \frac{k^2}{s^2}\left(2e^{-s\frac{dz}{2}} - 2 - e^{-s(2z_c+\frac{dz}{2})}\right) J_1(kr_a)dk \\ &+ \frac{r_i}{2\sigma_b}\int_0^\infty \frac{k^2}{s^2}\left(2e^{-s\frac{dz}{2}} - 2 - e^{-s(2z_c+\frac{dz}{2})}\right) J_1(kr_i)dk, \end{aligned} \tag{4.7}$$

and the non-diagonal are given as

$$\begin{aligned} A_{ij} = &-\frac{r_a}{2\sigma_b}\int_0^\infty \frac{k^2}{s^2}\left(e^{-s(|z_i-z_j|+\frac{dz}{2})} - e^{-s(|z_i-z_j|-\frac{dz}{2})}\right. \\ &\left. -e^{-s(z_i+z_j+\frac{dz}{2})} + e^{-s(z_i+z_j-\frac{dz}{2})}\right) J_1(kr_a)dk \\ &+\frac{r_i}{2\sigma_b}\int_0^\infty \frac{k^2}{s^2}\left(e^{-s(|z_i-z_j|+\frac{dz}{2})} - e^{-s(|z_i-z_j|-\frac{dz}{2})}\right. \\ &\left. -e^{-s(z_i+z_j+\frac{dz}{2})} + e^{-s(z_i+z_j-\frac{dz}{2})}\right) J_1(kr_i)dk. \end{aligned} \tag{4.8}$$

In order to allow for multiple steel-cased wells, interaction between the wells has to be considered. Thus I followed the general basic idea in a straight forward way to expand the idea of Tang et al. (2015) for multiple steel casings. Considering there are M casings, one can expand eq. 4.4 to contain $M \times M$ blocks where the diagonal blocks encapsulate the interaction within the same well. The off-diagonal block contains all

interactions between two wells.

$$\mathbf{A} = \begin{pmatrix} \mathbf{A}_{11} & \mathbf{A}_{21} & \dots & \mathbf{A}_{M1} \\ \mathbf{A}_{12} & \mathbf{A}_{22} & \dots & \mathbf{A}_{M2} \\ \vdots & \vdots & \ddots & \vdots \\ \mathbf{A}_{1M} & \mathbf{A}_{2M} & \dots & \mathbf{A}_{MM} \end{pmatrix} \tag{4.9}$$

the diagonal blocks are calculated as presented by Tang et al. (2015). To calculate the off-diagonal blocks I assume the horizontal dimensions of each steel casing to be neglectable compared to the horizontal distance between two wells. Instead I assume the current on each casing to be a vertical line source current. The coefficients in the off-diagonal blocks of $\mathbf{A}$ are therefore calculated as follows:

$$A_{ij} = \pi(r_a^2 - r_i^2) \int_{z_i - \frac{dz}{2}}^{z_i + \frac{dz}{2}} G_{zz}(x_j, y_j, z_j | x_i, y_i, z') dz', \tag{4.10}$$

which finally leads to

$$\begin{aligned} A_{ij} = \frac{r_a^2 - r_i^2}{4\sigma_b} \int_0^\infty \frac{k^3}{s^2} \Big(& 2 + e^{-s(z_j + z_i + \frac{dz}{2})} - e^{-s(z_j + z_i - \frac{dz}{2})} \\ & - e^{-s(z_j - z_i + \frac{dz}{2})} - e^{-s(-z_j + z_i + \frac{dz}{2})} \Big) J_0(kd) dk \,, \end{aligned} \tag{4.11}$$

if $z_i - \frac{dz}{2} < z_j < z_i + \frac{dz}{2}$ and otherwise

$$\begin{aligned} A_{ij} = \frac{r_a^2 - r_i^2}{4\sigma_b} \int_0^\infty \frac{k^3}{s^2} \Big(& e^{-s(|z_i - z_j| + \frac{dz}{2})} - e^{-s(|z_i - z_j| - \frac{dz}{2})} \\ & - e^{-s(z_i + z_j + \frac{dz}{2})} + e^{-s(z_i + z_j - \frac{dz}{2})} \Big) J_0(kd) dk \end{aligned} \tag{4.12}$$

for all segments i and j that do not belong to the same well.

4.2.2 Implemented optimisation strategies

The coupling matrix $\mathbf{A}$ is independent of the actual transmitter, hence it only has to be evaluated once for each frequency. The system of equations from eq. 4.4 than has to be solved for many right hand sides (one for each transmitter). I therefore use the direct solver from the LAPACK library (Anderson et al., 1999) performing a LU decomposition.
During inversion the background model is generally kept fixed, it is therefore sensible to reuse the entire background field in each inversion iteration. This allows elimination of the time consuming evaluation of the additional contribution of each well segment to the background field from all but the first iteration of an inversion.
Especially for large scale applications with a large number of steel-cased wells, calculation of the coupling coefficient matrix becomes time consuming, although only performed once for each frequency during the entire inversion. However computing time can be significantly reduced by making use of symmetries.

As shown in Fig. 4.4 many coupling coefficients are identical when borehole geometries from neighbouring wells do not differ. In the most extreme scenario with

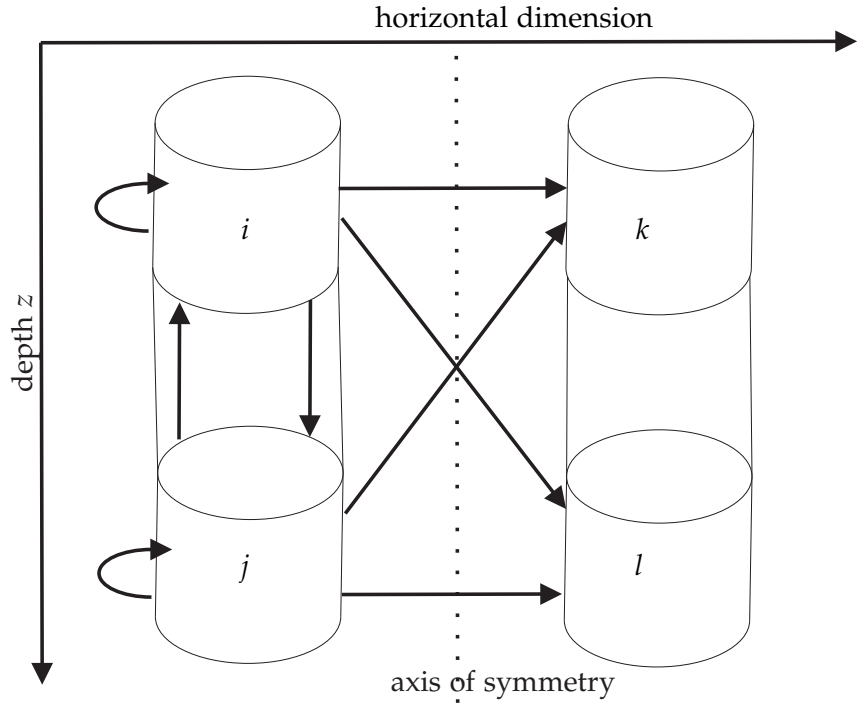

Figure 4.4: Sketch showing independent coupling coefficients between two wells whose segments have the same outer and inner radius as well as conductivity of steel (taken from Patzer et al., 2017b). Furthermore depth as well as thickness of segment i and k are the same. The same holds for segment j and l. Each arrow indicates one coupling coefficient. All missing coupling coefficients are redundant due to rotational symmetry towards the axis of symmetry.

M identical wells split into N segments each, the number of independent coupling coefficients is reduced from $(MN)^2$ to $MN + N^2$.
Finally the calculation of each coupling coefficient is independent and can be distributed among several computing nodes for parallel processing easily.

4.2.3 Estimation of background conductivity

In comparison to the algorithm presented in Patzer et al. (2017b) the way the homogeneous halfspace conductivity is obtained was modified. Initially a weighted average background conductivity along each well was chosen to be the homogeneous halfspace conductivity in the presented algorithm. This leads to erroneous current strengths, especially when the transmitter is galvanically connected to the casing and the galvanic connection is in regions where homogeneous halfspace conductivty and background conductivity differ. This is illustrated in Fig. 4.5 a) where the obtained current distribution along a single steel-cased well being galvanically connected to a transmitter is shown. The background model for this scenario is a layered halfspace model. The averaged resistivity that has been used for the homogeneous halfspace approach is $3.436\,\Omega\,\mathrm{m}$ which does not match the resistivity of the uppermost layer of $12\,\Omega\,\mathrm{m}$. This creates non-physical current strength up to four times the current strength of the transmitter at the top of the casing.

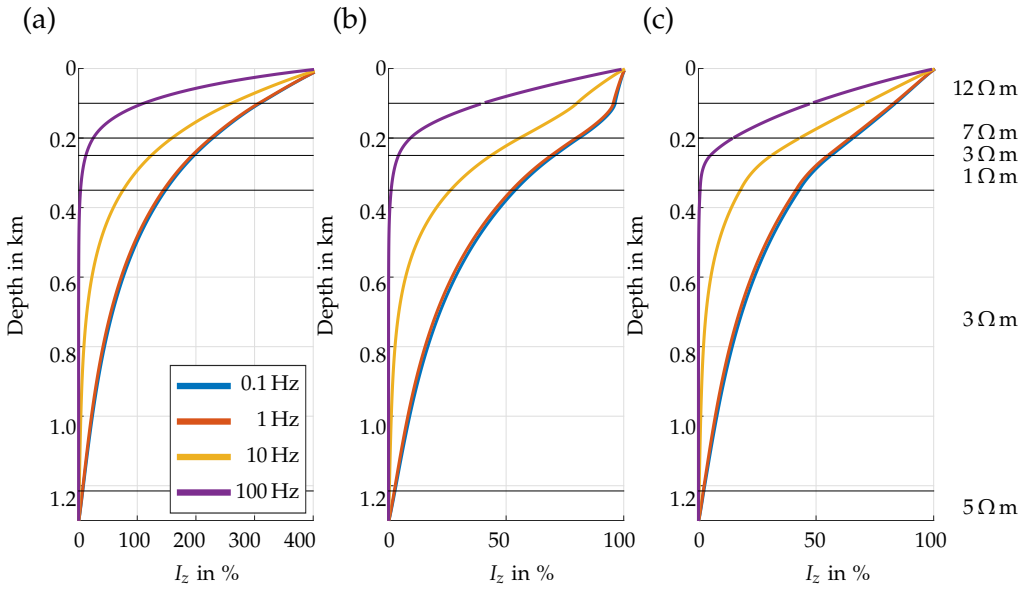

Figure 4.5: Current distribution along a single steel-cased well given a galvanically connected transmitter for a number of frequencies and three different borehole segmentations. Current strengths are normalized to the current strength of the transmitter (a) One halfspace conductivity is chosen for the entire casing. (b) The casing is split in two segments. The upper part of the casing coincides with the first layer, hence uses halfspace conductivity of the first layer. The lower part uses an averaged conductivity of the remaining layers. (c) The casing is split into six segments, one for each layer penetrated by the casing. Each new well is assigned the conductivity of the corresponding layer. Note the different scales of I_z axes between (a) and (b),(c)

Changing the implementation assuming individual values of the halfspace conductivity for each well, allows to simply split one well into multiple wells and stack them on top of each other. By splitting the borehole at the depths of layer boundaries one can consider layered background structures more appropriately than before. Fig 4.5 b)-c) shows the current distribution for the same setup as before but using the refined approach of halfspace conductivity. In scenario b) only the part of the well in the upper most layer is split off the rest of the well. While in scenario c) each part of the well inside each layer is treated as individual steel-cased well. In both cases the unphysical high current strength at the surface returned to 100% of the transmitter strength, which would be expected when it is galvanically attached to the casing. Differences between b) and c) still occur but are far less severe than the difference between a) and b).

4.3 Numerical experiments

In the following I am showing different numerical experiments in order to highlight several aspects of steel-cased wells and their effect on CSEM data as well as practical implications that should be considered when planning CSEM measurements in the presence of steel-cased wells.

4.3.1 Current distributions along casings

Since steel-cased wells act as additional VED sources the strength of the obtained current along each well is of great importance. According to equation 4.4 it is the background electric field along the borehole trajectory that gives rise to the currents along the wellbore. The background electric field is mainly depending on the borehole-transmitter geometry (cf. Fig. 2.5). The current strength along each well is additionally dependent on the background conductivity and the frequency of the used signal. Some of the mentioned aspects are shown and discussed in the two following examples.

Coupling of boreholes

This first example is highlighting the importance of the inductive interaction between wells which had been neglected by Tang et al. (2015). In this scenario two wells of 1300 m length are placed 500 m apart of each other in a 3 Ω m halfspace. A 1000 m long grounded electric dipole transmitter is galvanically connected to one of the casings (the red casing Fig. 4.6 a). Fig. 4.6 b-e) shows current strength along both casings for a number of frequencies and two different scenarios.

The two different scenarios shown are: (i) in b) and d) the interaction between the wells is neglected and (ii) the interaction is taken into account in c) and e). Regardless the interaction, in case of the galvanically connected (active) casing (figures inside the red box) the full current strength of the transmitter is reached near the surface for all frequencies b,c). However, current strength is decreasing exponentially with depth. According to the skin effect the decay is faster for higher frequencies. For frequencies below 1 Hz the rate of the decay does not decrease further, thus the DC limit of current strength is reached. Comparing current strengths for the active casing the difference if interaction between wells is considers is negligible.

The current strength along the inductively coupled (passive) borehole d,e) (Figures inside the green box) is much weaker than for the active well, staying below 2% of the current strength of the transmitter. Due to the large conductivity contrast between air and steel at the top and rock and steel at the bottom current flow across this boundary is permitted resulting in vanishing current strengths at both ends. Therefore highest currents are found in some intermediate depth at approximately 600 m. Similarly to the active borehole, currents are weaker for higher frequencies. The background fields decay faster with depth for higher frequencies. Thus, the maximum current strength along the casing is found at shallower depths for higher frequencies. The DC limit is reached for frequencies below 0.1 Hz. In the case of the inductive coupling neglecting the interaction between wells results in current strengths 50% stronger.

Neglecting the interaction between wells effectively means that the current on each well is obtained as if each well is considered the only well present. In the case of multiple wells the total amount of energy in the system has to stay constant compared to the single casing case. The energy is therefore unevenly distributed between the casings resulting in lower amplitude currents on each well. Therefore neglecting the interaction between casings would in general result in over estimated current strengths on each well and thus significantly overestimate the influence of steel-cased wells.

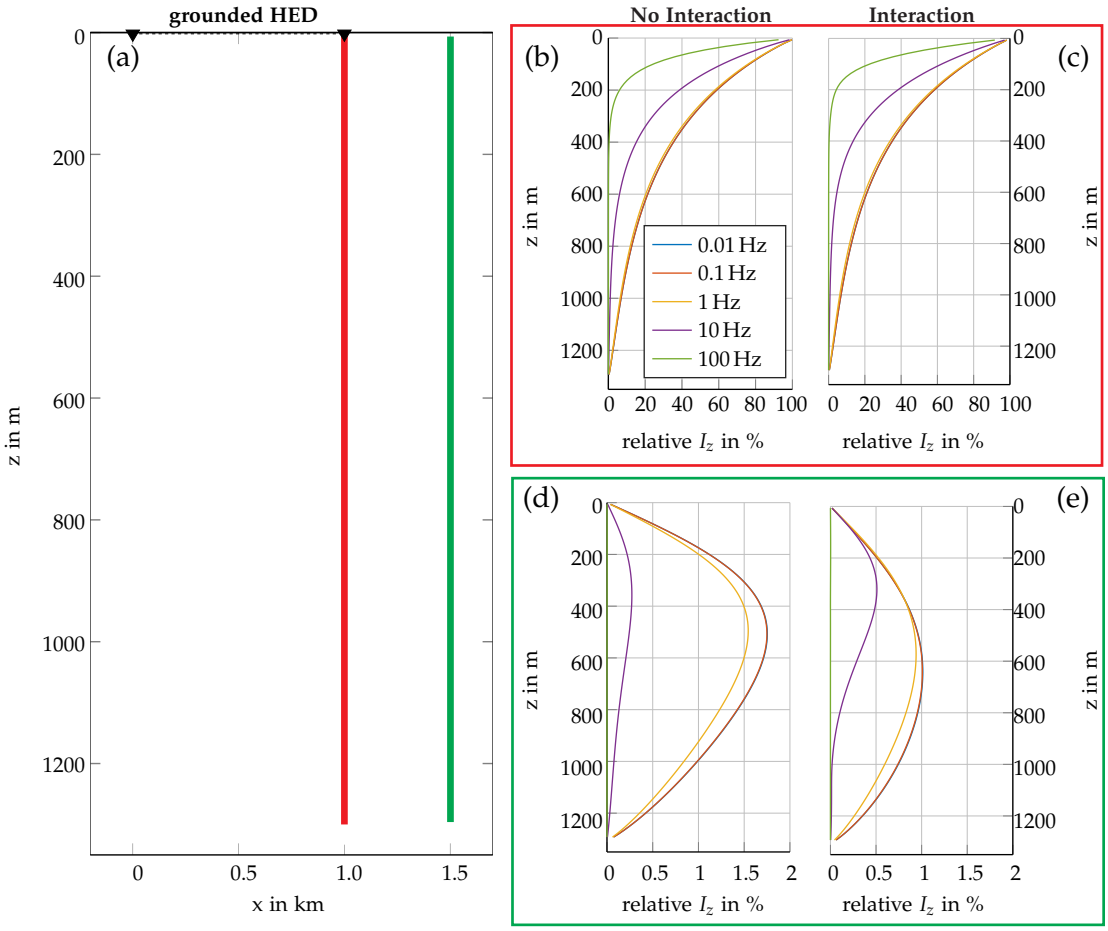

Figure 4.6: Relative current strength normalized to transmitter current along two steel-cased wells for two scenarios. a) Transmitter borehole geometry for both scenarios, red casing is active, green passive. b) Current along red casing neglecting mutual interaction. c) Current along red casing including mutual interaction. d) Current along green casing neglecting mutual interaction. e) Current along green casing including mutual interaction.

Borehole transmitter distance

Another aspect controlling the borehole currents is the distance to the transmitter. Fig. 4.7 shows the obtained current strength along a single metal casing for various distances to a grounded horizontal electric dipole transmitter using a single frequency. The general setup is kept similar to the example before. The borehole is 1300 m long and it is placed inline with the transmitter axis.

In general current decreases rapidly with increasing distance to the transmitter and

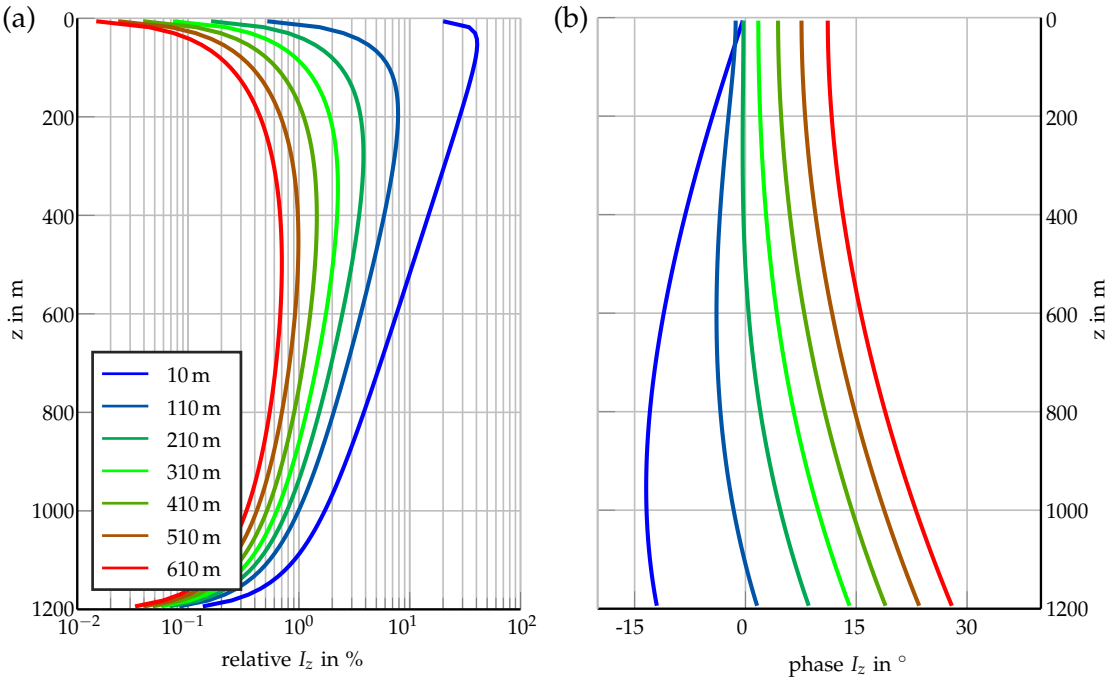

Figure 4.7: Current distribution with depth along steel-cased wells for varying transmitter borehole distances (modified after Patzer et al., 2017b). Transmitter is a grounded electric dipole of 1 km length. Simulations are calculated for a frequency of 1 Hz and the background model has a resistivity of 3 Ω m. Steel casings are placed inline with the transmitter. Distances are taken to the nearest grounding point of the transmitter.(a) Amplitude of current along the well, (b) phase of current along the well. Note the logarithmic scale of I_z axis in (a).

maximum currents are found at shallower depths for smaller distances. At a distance of 10 m currents reach up to 40% of the transmitter strength with its maximum value at 30 m depth.

In addition to the example shown before phases are shown in Fig. 4.7 b). Generally phases do not vary as much with depth as the amplitude. However, phases do change significantly with distance to the transmitter. If the transmitter is placed in 100 m distance to the borehole the induced current along the casing is approximately in phase to the current from the transmitter. For increasing distances phase differences between the borehole current and the transmitter current increase. At a distance of 610 m difference in phase varies between 12° at surface and 28° at 1200 m depth.

These results suggest that if one wants to exploit the presence of steel cased wells

by maximising currents along the wells, it would be most beneficial to attach the CSEM transmitter galvanically. If this is not feasible due to logistical limitations or safety regularities, one should set up the transmitter in close proximity (a few tens of metres) to the casing. As it still results in strong currents along the borehole. Therefore simply installing the transmitter in close proximity to the casing can be seen as easy to implement alternative without direct galvanic attachment.

4.3.2 Implications for the Bockstedt field surveys

In order to quantify how strong the influence of steel-cased wells is on the data collected in the Bockstedt oil field, I calculated the relative influence on synthetic transfer functions (TFs) of the horizontal electric fields using the field setup from the 2014 survey (see section 3). The influence was calculated using the surface position of 78 known wells.
In this example the influence is shown for two polarisations of the transmitter S04. This transmitter has the largest mean distance to all casings ($\approx 2\,\mathrm{km}$) of all transmitters. Fig. 4.8 shows a map view of the relative change in the amplitude of the TF due to the presence of these wells for two different polarisations.
White colours show no influence on TFs, while red colours show an increase in TFs

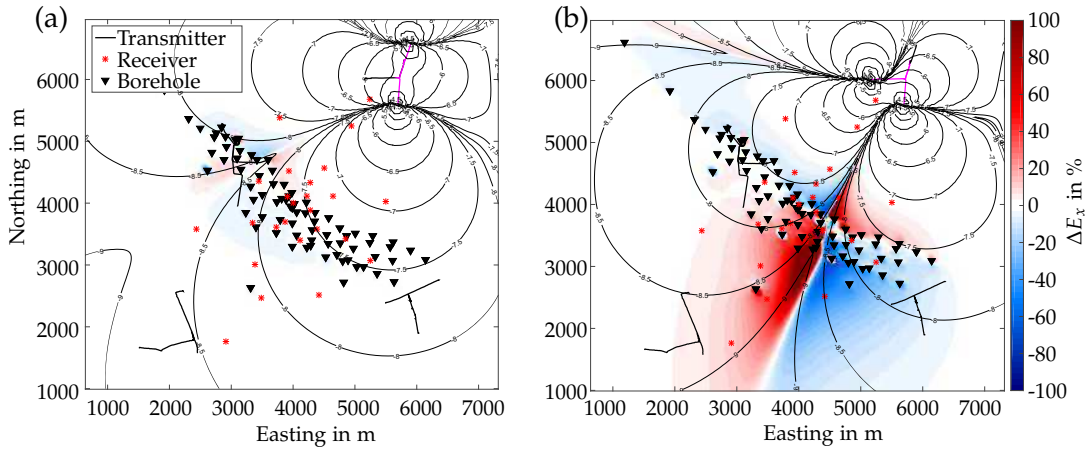

Figure 4.8: Relative change in TFs amplitude due to the presence of steel-cased wells using field setup from the 2014 Bockstedt survey for two different polarisations of the same transmitter a) and b). Wires of independent source current are marked in purple. Background model is a $3\,\Omega\,\mathrm{m}$ homogeneous halfspace and the used frequency is 0.0156 Hz. The $\log_{10}$ of absolute values of the undisturbed electric field is shown by isolines.

amplitude and blue colours a decrease in the absolute value of the TF. The colour saturation marks the strength of the effect of metal casings.
In general Fig. 4.8 a) shows low influence while for a different polarisation of the same transmitter the response will be highly affected, as shown in Fig. 4.8 b). Depending on the source polarisation responses can be altered up to 100 % and more in large portions of the study area while being mainly unaltered for other polarisations.

Systematic investigation had shown that for each transmitter there usually exists one heavily influenced polarisation and one where relative influence is rather weak. The third polarisation is mostly moderately affected.
Since one of the three polarisations is redundant, one can in theory choose those two polarisations for subsequent inversion that are least influenced by steel-cased wells. However, finding those two polarisations in practice is questionable since the actual influence of the boreholes is interacting with the conductivity distribution of the subsurface. Note that the two polarisations of lowest influence will be different for each transmitter-receiver pair and field component and may even change between frequencies.

4.4 Inversion Examples

Finally the influence of steel casings on the inversion itself has to be discussed.

4.4.1 Inversion neglecting steel casings

To show influence of steel-cased wells on the inversion of the data collected in the Bockstedt oil field synthetic data have been created. The true model is a homogeneous halfspace of $3\,\Omega\,\mathrm{m}$ together with the same 78 steel-cased wells as shown before. Again the alternative setup of transmitter S01 not being connected to the casing of the abandoned well is used. Seven frequencies in logarithmic spacing between $1/64\,\mathrm{Hz}$ to $32\,\mathrm{Hz}$ have been used. Data are TFs of horizontal electric fields perturbed by 3% Gaussian noise.

A 3D inversion using these synthetic data as input has been performed neglecting the presence of all metal casings. Starting model was the true $3\,\Omega\,\mathrm{m}$ halfspace. The dimensions of the modelling grid have been set to $150 \times 150\,\mathrm{m}^2$ for horizontal dimensions and an increasing discretisation in vertical direction with 10 m at surface and 50 m at reservoir depth in 1200 m depth.
Fig. 4.9 shows the obtained model. Although the starting model was equal to the true model an artificial conductor of about 1-2 $\Omega\,\mathrm{m}$ is imaged at the position of the metal casings. From Fig. 4.9 b) one can see that the conductor is inclined. It is shallowest just below transmitter S01 at about 300 m depth and moving to greater depths towards the south-east to transmitter S05 in approximately 1200 m depth.
The data fit in form of nRMS is summarised in Fig. 4.10. a) and b) show the distribution of initial and final nRMS per receiver site. The initial nRMS (Fig. 4.10 a) is highest ranging between 15 and 20, for the sites in the centre of the array where also most of the steel cased wells are located. After the inversion nRMS (Fig.4.10 b) is approximately evenly distributed mostly ranging between 10 and 5. Finally the decrease of the global nRMS is shown in Fig.4.10 c). Over the course of 20 iterations misfit decreased continuously from 27.3 to 6.4.
This inversion shows that neglecting the presence of all steel-cased wells during an inversion may lead to artificially high nRMS values even if the true subsurface model is used. This further causes the inversion to place artificial mainly conductive structures that are only caused by the presence of the metal casings. In the shown example the location of the conductive artefacts correlates well with the position of the borehole

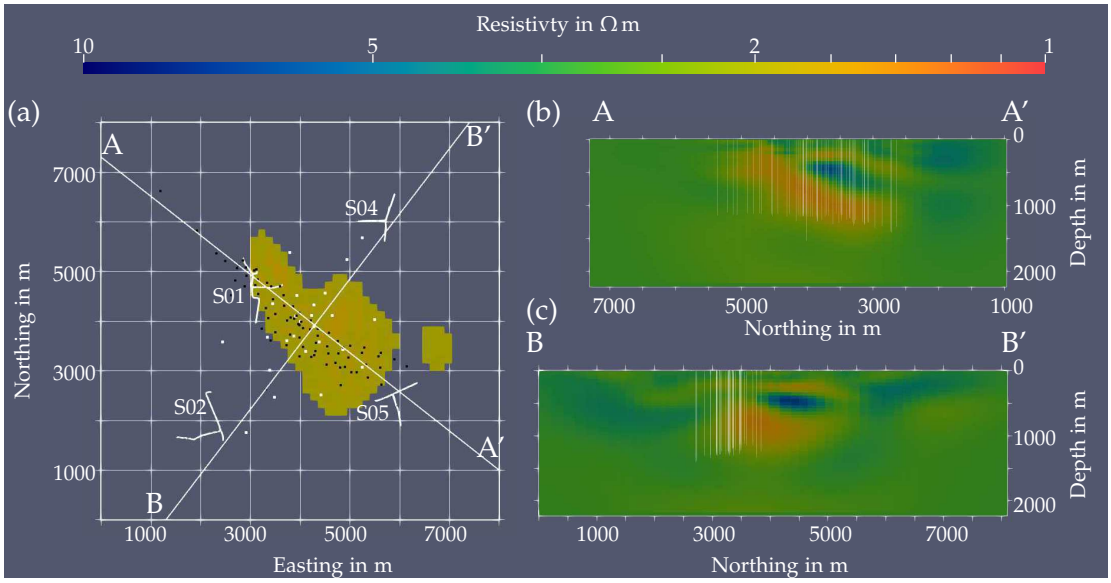

Figure 4.9: Final model of inversion of synthetic data neglecting presence of wells after 20 iterations. a) Map view showing all cells with anomalous resistivity value below 2 Ω m. Black dots mark positions of steel-cased wells, white lines transmitter locations and white dots the receiver positions. b) Slice along profile A in strike direction of borehole cluster. c) Slice along profile B perpendicular to strike direction of borehole cluster.

cluster. Furthermore the depth the conductor strongly correlates with the maximum of the current amplitudes on the casings. Especially for data related to transmitters S01 which is situated inside the borehole cluster, the depth of the maximum current on each well is controlled be the distance to the transmitter. Just next to the transmitter strongest currents are found near the surface, while the maximum position is moving further down with increasing distance to the transmitter. This may suggest that the exact position and shape of the conductive artefact strongly correlates with the chosen source receiver setup.

4.4.2 Sensitivity Study

Considering steel-cased wells during an inversion leads to a redistribution of the electric field in the subsurface which in turn also affects the sensitivity distribution during the inversion. Since sensitivity is the key parameter relating changes in conductivity to changes in the predicted data, it is of great importance to study how it is influenced by the presence of steel-cased wells.
The following example shows how the cumulative sensitivity is affected due to the presence of metal casings. Cumulative sensitivity is given by the sum of squared sensitivities for all data components considered in the inversion.

$$J_i^{cum} = \frac{1}{N}\sqrt{\sum_{j=1}^{N} |W_{d,j}J_{i,j}|^2} \tag{4.13}$$

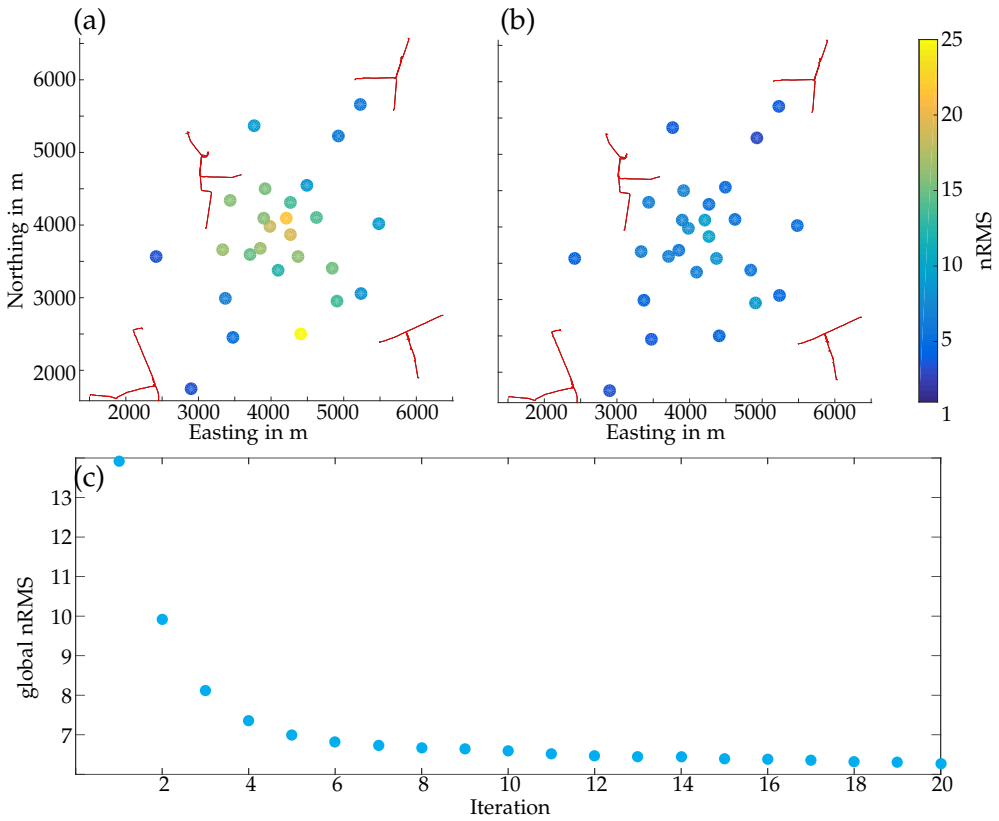

Figure 4.10: Obtained misfit during the inversion as nRMS according to eq. 2.16. a-b) Map view of misfit distribution by receiver stations for the initial and final model respectively. All data points of all frequencies, transmitters, polarisations and field components are combined individually for each receiver station. c) Evolution of global nRMS during each inversion iteration.

$J_{i,j}$ is one element of the sensitivity matrix relating changes in model cell i with changes in the predicted data point j. $W_{d,j}$ is the corresponding data weight from eq. 2.10.

To study how an inversion of the collected data from the Bockstedt oil field might be influenced I calculated the change of the cumulative sensitivity using the source receiver setup from the 2014 field survey for a $3\,\Omega\,\mathrm{m}$ halfspace. For transmitter S01 the alternative setup without galvanic connection to the casing of the abandoned well is used. The location and depth of 78 steel-cased wells drilled in the Bockstedt oil field was provided by Wintershall. Fig. 4.11 shows the obtained changes of the sensitivity. In general one can observe a decreasing sensitivity near the surface (blue colours in a) while it is increasing at depth (red colours in b). Strongest changes in amplitudes are found below transmitter S01 which is the transmitter with the smallest distance to the casings. Overall largest increase correlates with the bottom of the steel-cased wells. Note that the shown results consider cumulative sensitivities of all source receiver combinations. Similar to results shown before the influence on single TF is highly variable.

In summary, inductively coupled steel casings redistribute energy in the subsurface by acting as current channels to greater depth effectively moving energy from surface to deeper layers and thereby enhancing sensitivity and thus resolution at depth. In-

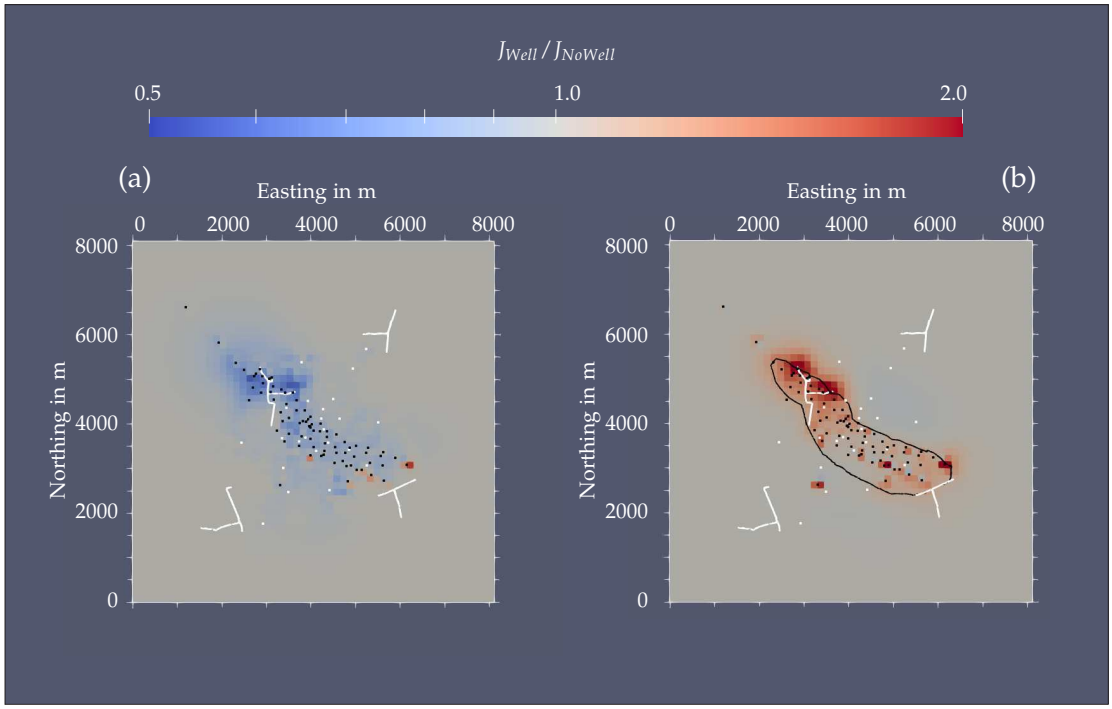

Figure 4.11: Change of the cumulative sensitivity due to presence of 78 wells using the source receiver setup from the 2014 field survey for a 3 Ω m halfspace. For transmitter S01 the alternative setup without galvanic connection to the casing of the abandoned well Bockstedt 23 is used. Only one frequency of 1 Hz is used. (a) Change in sensitivity near the surface (50 m) (b) Change in sensitivity at reservoir depth (1200 m) Transmitter and receiver positions marked as white points and lines and the position of boreholes and the outline of the Bockstedt oil field as black points and line respectively

crease is largest just at the bottom of the casings and in the vicinity of casings closest to the transmitter where currents are expected to be strongest. In an active oil field most casings can be expected to end inside or just below the reservoir layer, hence their influence on detectability and resolution towards changes in fluid saturation can be regarded positively despite being challenging to include into modelling and inversion.

4.4.3 Influence on reservoir resolution

Here I am demonstrating the beneficial effects of using existing steel-cased wells as galvanically coupled source extensions on the resolution of a resistive reservoir. Again synthetic data have been created for the CSEM field setup from the surveys across the Bockstedt oil field. The true model as well the source receiver setup is shown in Fig. 4.12. The background resistivity structure is a layered halfspace based on a magnetotelluric study across the Bockstedt oil field (see Tietze et al., 2015) and will be referred to as the *canonical layered halfspace* model in the future. At surface the resistivity is 12 Ω m and is decreasing with depth. From 200 m to 300 m depth is a

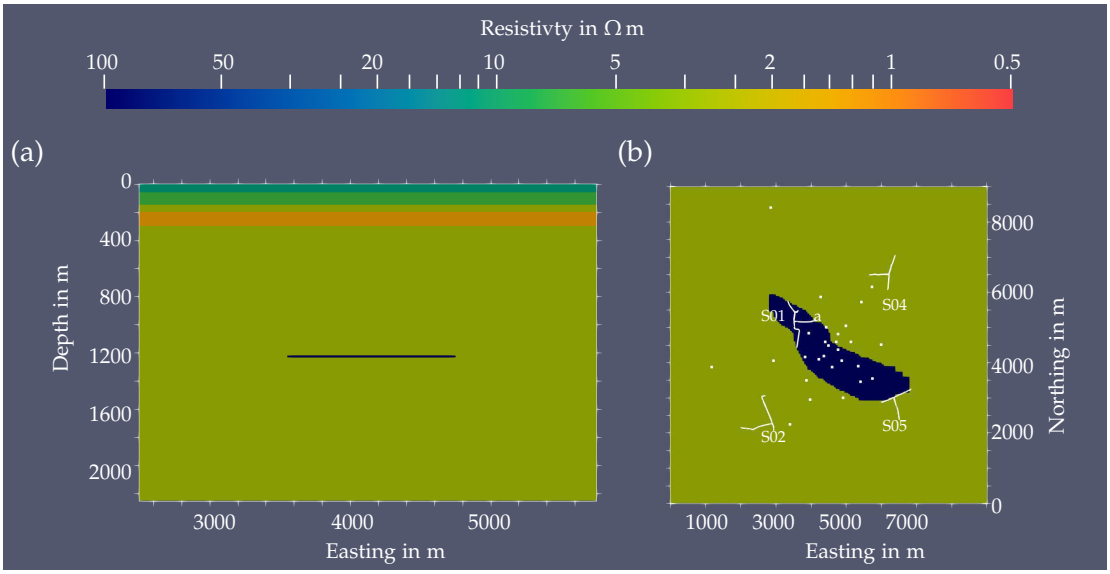

Figure 4.12: Horizontal and vertical slices through through a 3D resistivity model used to generate synthetic data. (a) East-depth slice through model at $x = 4500\,\text{m}$. (b) Horizontal slice at reservoir depth $z = 1200\,\text{m}$. Lateral positions of transmitters are marked by white lines and receiver positions by white dots. The 1.3 km long steel-cased well replaces the *a*-electrode of transmitter S01.

highly conductive layer of $1\,\Omega\,\text{m}$. The conductive layer is followed by a $3\,\Omega\,\text{m}$ half-space. Into the *canonical layered halfspace* a 30 m thin resistor of $100\,\Omega\,\text{m}$ is added at 1200 m depth. The outline of this resistor corresponds to the outline of the Bockstedt oil field. TFs of horizontal electric fields for ten logarithmically spaced frequencies between 0.0156 and 98.59 Hz have been generated and contaminated by 3% Gaussian noise. Two datasets have been created one neglecting presence of steel-cased wells. And a second where one 1.3 km deep well is galvanically attached to transmitter S01, resembling the abandoned well from the field surveys (see section 3).
For the inversion the same grid as in the inversion before has been used with grid cells of $150 \times 150 \times 50\,\text{m}^3$. Both datasets have been inverted using the same inversion setup using Tikhonov regularisation (see section 6.3). Assuming to have good knowledge of the general background structure the true layered background has been used as starting and reference model during the inversion. An additional model weighting scheme (see section 6.5) has been applied in order increase the sensitivity towards the reservoir. The weight of all cells below 1300 and above 1100 m (100 m above and below the reservoir) has been reduced to 0.5 while weights of all other cells is set to 1. Results are shown in Fig. 4.13.
The final model of both inversions is shown in Fig 4.13 a,c). Both inversions mapped a resistive structure laterally within the reservoir. However both inversions could not recover the true dimensions of the resistive reservoir. The inversion without any borehole resolved the central part of the reservoir (approximately in the middle of the source receiver setup) best, while it failed to resolve the target in the north-western and south-eastern edges. This can be easily explained by the missing data coverage of these reservoir regions, as the source receiver setup applied in the field surveys

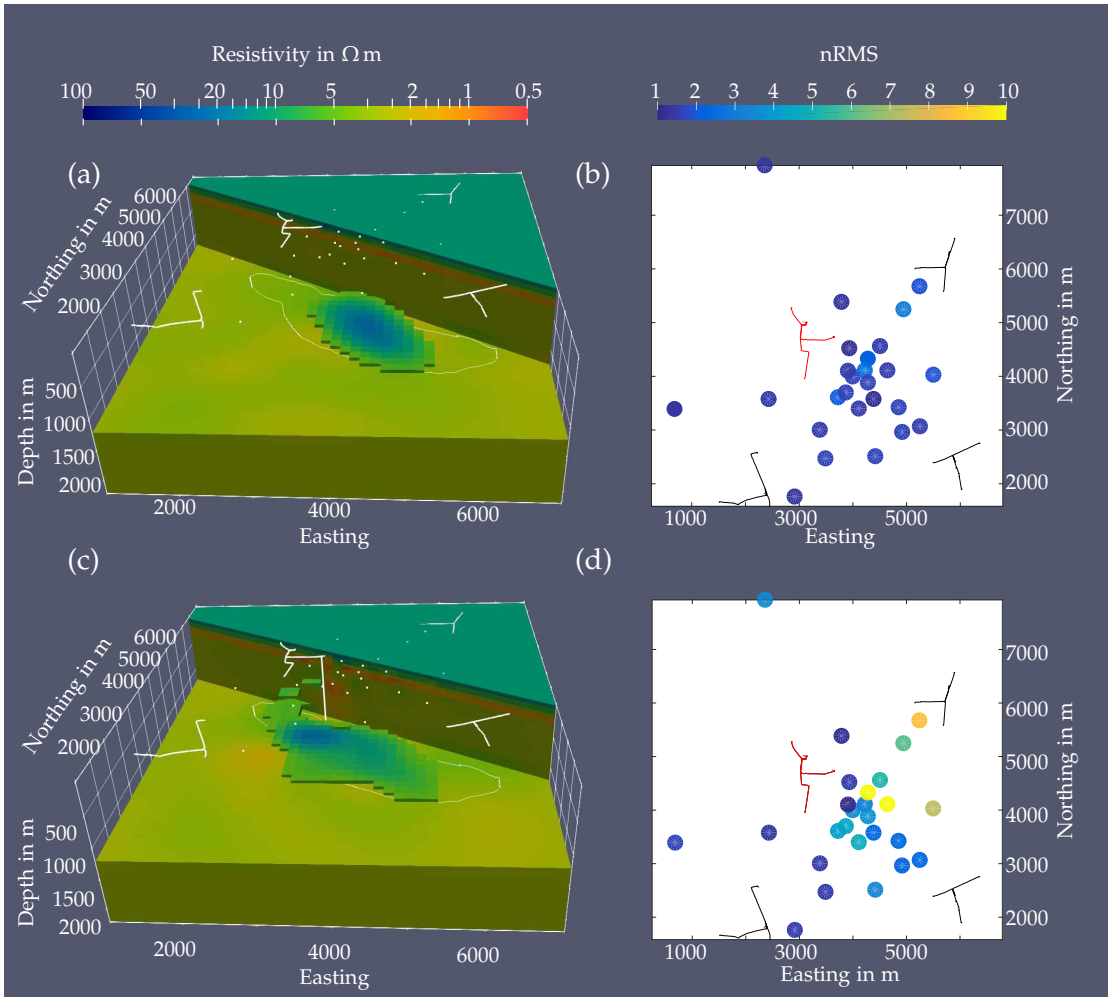

Figure 4.13: a, c) Final inversion models of two synthetic data-sets for the true model shown in Fig. 4.12. Transmitter positions and reservoir outline are marked by white lines and receiver positions by white dots. All cells above 5 Ω m are kept visible. a) Final model using dataset without any steel-cased wells after 25 iterations. nRMS decreased to 1.33 (-44%). c) Final model using dataset including one galvanically attached steel casing after 25 iterations. Borehole position is marked as white line. nRMS decreased to 1.37 (-51%). b, d) Map view of misfit distribution by receiver stations for the initial model for the datasets from (a) and (c) respectively. Misfits are obtained according to eq. 2.16. Only data of the borehole transmitter (marked in red) are considered. All data points of all frequencies, polarisations and field components are combined individually for each receiver station.

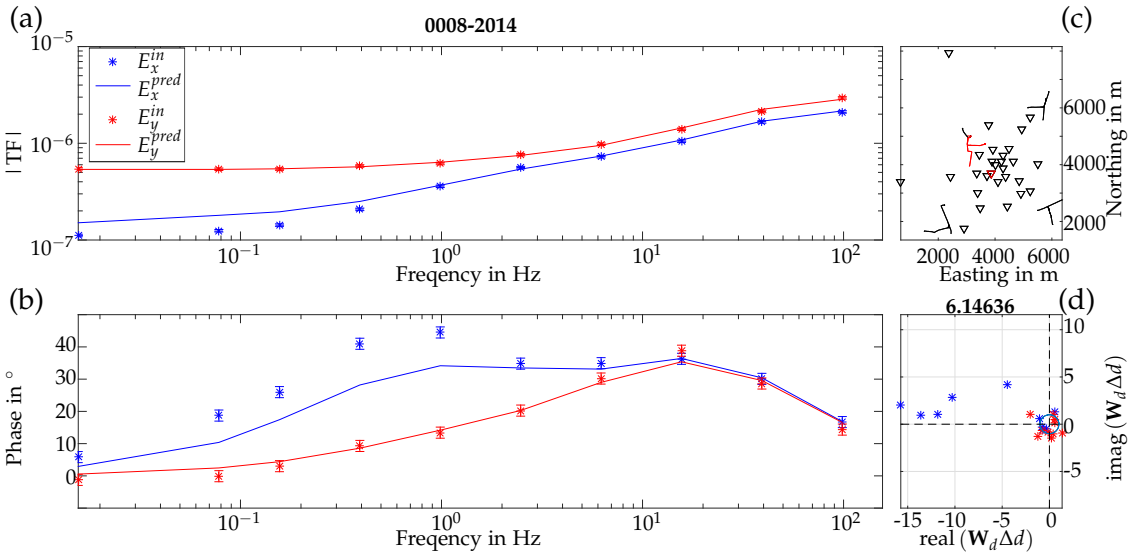

Figure 4.14: Initial misfit of the inversion including steel casing shown in Fig. 4.13 d) (a) Amplitude and (b) phase of TFs over frequency of input data and model response of a single receiver station. (c) Map view showing source receiver orientation. Active wires and the corresponding receiver are marked in red. (d) Normalised misfit of each individual data point in a) and b) in the complex plain. Colours correspond to the field components in (a) and (b). The total nRMS for all for all shown data points is given above. The blue circle marks the target misfit corresponding to an nRMS of 1.

was designed to maximise resolution in the centre of the reservoir. In contrast the best resolved region of the reservoir moves towards the north-west when considering the second inversion including the actively coupled borehole. Furthermore the volume of elevated resistivity at reservoir depth compared to the starting model is larger than for the inversion without any steel-cased wells. Since boreholes act as additional sources, and sensitivity is largest in the vicinity of sources and receivers resolution power increases near the borehole.

This can also be see seen by means of the initial misfit (see Fig. 4.13 b and d). Shown is the nRMS using a subset of data points for each receiver station, combining all polarisations field components and frequencies of one transmitter (marked in red). Only the misfit for the borehole transmitter is shown, since only for this transmitter differences between the two inversions are visible. While the nRMS is distributed evenly among all transmitters for the inversion without any boreholes (an example is shown in Fig. 4.13 b). Initial misfits are 3-4 times higher in the scenario including the actively coupled borehole. Since the only difference between the true model and the starting model is the presence of the resistive reservoir one can clearly see that sensitivity towards the reservoir structure is highly increased when using the steel casing of a borehole for current injection.

Finally in order to show the reduction of misfit on individual data points the datafit for the initial and the final model of the inversion with borehole is shown in Fig. 4.14 and 4.15. Shown are amplitude (a) and phase (b) curves of the two electric field components over frequencies of input and predicted data of one TF of a single source

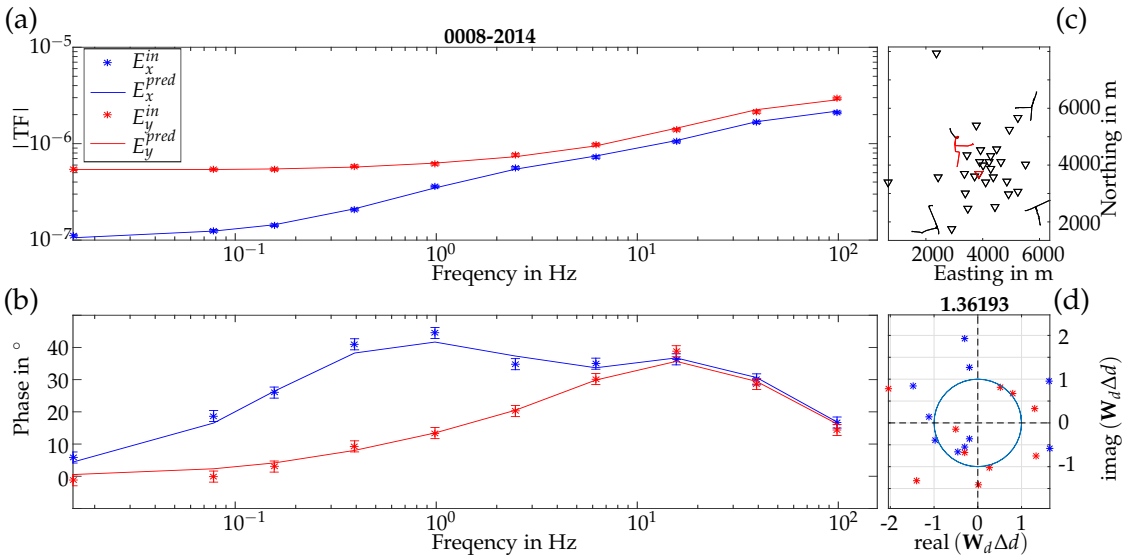

Figure 4.15: Final misfit after 25 iterations of the inversion including steel casing shown in Fig. 4.13 d) (a) Amplitude and (b) phase of TFs over frequency of input data and model response of a single receiver station. (c) Map view showing source receiver orientation. Active wires and the corresponding receiver are marked in red. (d) Normalised misfit of each individual data point in a) and b) in the complex plain. Colours correspond to the field components in (a) and (b). The total nRMS for all for all shown data points is given above. The blue circle marks the target misfit corresponding to an nRMS of 1.

receiver combination. The source-receiver geometry is marked in c). For each data point in a) and b) the real and imaginary part of the normalised misfit ($W_{d,i}\Delta d_i$, see eq.2.10) is shown in the complex plane in Fig. d). The target misfit of 1 is shown as blue circle.
The initial misfit shown in Fig. 4.14 shows that misfit is generally small for frequencies above 5 Hz. Which is in accordance to the skin effect, as the true model and the starting model only differed by the presence of the reservoir. Highest misfits are found for the E_x component for frequencies below 5 Hz. In addition the heterogeneous behaviour of the different EM-field components becomes eminent as the data fit of the E_y-component is much smaller over the entire frequency range than the E_x-component. This can also be seen in the scatter plot of normalised misfits in the complex plane shown in d). Especially the real part of E_x-component shows large misfits up to 15 times the target misfit. This highlights that different field components for the same source receiver setup will be differently influenced due to the presence of steel-cased wells.
Misfit for the model after 25 iterations (see Fig. 4.15) decreased significantly. Amplitude and phase curves (a,b) show now frequency or component dependency. Similarly the misfit scatter plot d) shows a similar distribution for both components around the target misfit of 1.

4.4.4 Application to field data

Finally I am showing two inversions of the field data collected in the Bockstedt oil field in the 2014 survey under the influence of steel-cased wells. As the focus of my work was on the numerical implementation of steel casings no interpretation of the obtained models is made. The results are taken from Tietze et al. (2016). Inversions used TFs of horizontal electric field data of all four transmitters. In total 13 logarithmically equidistant frequencies between 0.0156 Hz and 6.22 Hz have been used. In this study we aimed at estimating the maximum influence of metal casings. Thus based on the considerations shown in Fig. 4.8 we choose for each transmitter those polarisations where influence of the wells is expected to be largest.
Inversion started from a homogeneous $3\,\Omega\,$m halfspace using the same $150 \times 150 \times 50\,\mathrm{m}^3$ modelling grid as before. Regularisation is chosen to be smoothness constraint. Again two scenarios have been tested, one ignoring presence of steel-cased wells and one where we considered a subset of 11 casings.
The final model after 25 iterations of the inversion neglecting steel-cased wells is shown in Fig. 4.16 a) and while the final model considering 11 casings is shown in Fig. 4.16 c). Final misfits of all TFs of the y-component of the electric field for transmitter S01 (marked as red line) are shown in b) (neglecting casings) and d) (considering casings) respectively. Misfits are evaluated for each receiver station independently and is shown as scatter plot. Grey triangles mark the position of all steel-cased wells present within the study area. Black triangles mark those boreholes that have been considered during the inversion.
Due to its close proximity to many boreholes the North-western transmitter S01 is the one that is most influenced by the 78 casings present in the oil field. Currents along boreholes are large especially for those casings close to the grounding points

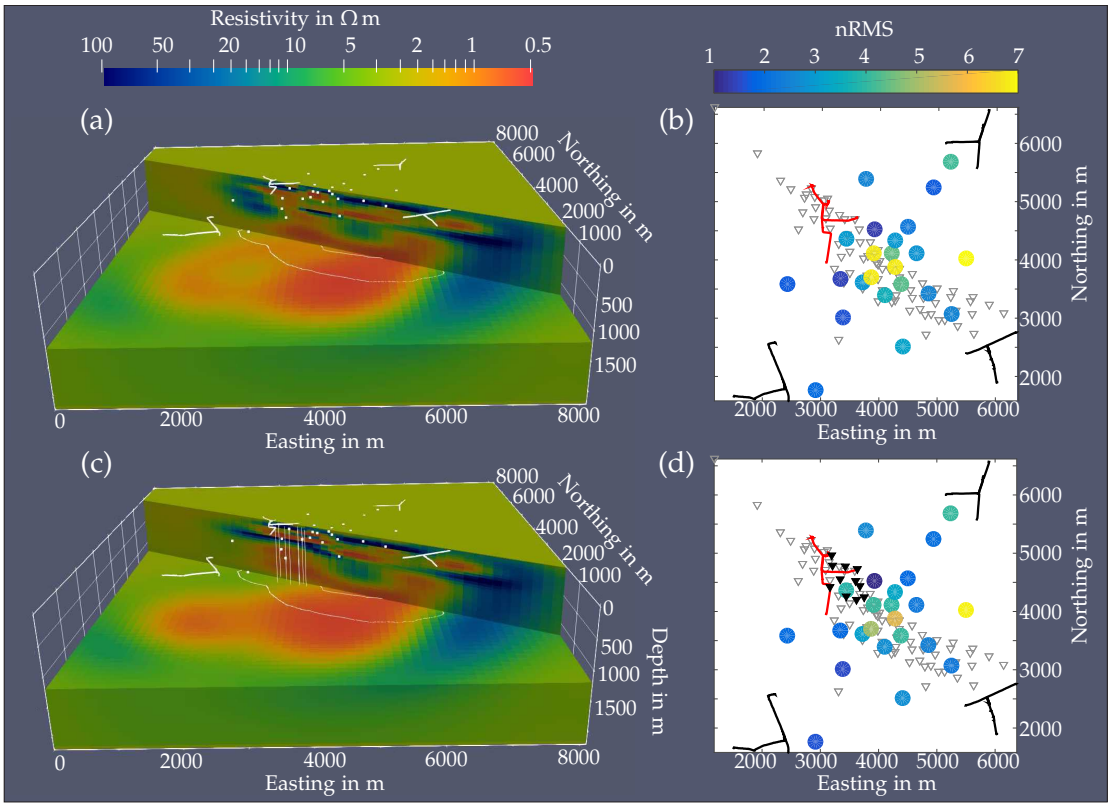

Figure 4.16: Inversion results of field data inversion under the influence of steel-cased wells, taken from Tietze et al. (2016). (a) Final model after 25 iteration for an inversion not considering any borehole. (b) Map view of misfit distribution by receiver stations for the E_y component of all data of transmitter S01 for the final model shown in a). The location of all known boreholes is marked by grey triangles. (c) Final model after 25 iteration for an inversion considering 11 boreholes in the vicinity of transmitter S01. Boreholes that have been considered are marked as white lines. (d) Map view of misfit distribution by receiver stations for the E_y component of all data of transmitter S01 for the final model shown in c). The location of all known boreholes is marked by grey triangles. Boreholes that have been considered are marked as black triangles.

of the transmitter S01. Thus we included those 11 casings that are in close proximity to transmitter S01. The distance of the included boreholes to any of the grounding points of transmitter S01 varies between 12 m and 968 m.

On large scales both inversions results show similar features. Within the upper 500 m a mainly layered conductivity structure is obtained with alternating layers of high (50 Ω m) and low resistivities (1 Ω m) including a conductive layer in approximately 250 m depth. A large conductive feature (>1 Ω m) has been imaged at reservoir depth in 1200 m for both inversions. At large distances to the considered casings (mainly in the south eastern part of the model) models do not differ. Differences appear in regions where boreholes have been once considered and once ignored. The conductive layer imaged at near the surface and the large conductor at reservoir depth appear to be connected just below transmitter S01, if steel-cased wells are not considered

during the inversion (Fig. 4.16 a). Taking boreholes into account however, results in a separation of the two conductive units by a highly resistive layer with resistivities above 50 Ω m (Fig. 4.16 c). As sub-vertical conductors are likely to be substitute structures placed by the inversion to mimic the effect of thin, long and extremely conductive steel casings (cf. Fig.4.9) obtaining a more layered structure is more likely to be close to the true conductivity structure. Additionally resistivity increased in the North-western part of the reservoir. This can be justified by a decreasing misfit for the receiver stations in the centre part of the model (see Fig. 4.16 b,d). Neglecting steel casings during the inversion results in large misfits up to an nRMS of 7 for the stations in the centre of the model. Taking the boreholes into account reduces misfits for those stations up to 50 %.
These results highlight that boreholes have to be taken into account even when they are not galvanically connected to the transmitter. Not considering them lead to poorer data fit and models that are less likely to represent reality. At this point one has to mention that we choose to show the effect for those polarisations where influence of steel casings is expected to be highest. In reality one may choose polarisations according to data quality thus reducing the influence of metal casings on the inversions. Often the influence of casings is strongest for those polarisation where amplitudes of the primary field produced by the transmitter is weakest and thus the lowest signal to noise ratio. In addition 3D inversion as well as interpretation of the obtained field data was not the focus of my thesis and work with the data is still ongoing, thus detailed analysis of these results is not part of this thesis.

4.5 Discussion and conclusions

To this point the presence of steel-cased wells has been a challenge in terms of modelling the propagation of EM fields in the subsurface. Due to their spatially unfavourable dimension it is numerically prohibitively costly to include these structures into the modelling grid even for finite element modelling. Therefore metal casings are described as additional substitute sources, taken their effect into account during the primary field calculation and subsequently transferring their influence to the secondary field approach for 3D modelling and inversion in a straight forward manner. This makes the approach independent and transferable to other implementations of a secondary field formalisms not only limited to FD modelling but also to finite element modelling.
The general algorithm is following an approach from Tang et al. (2015) and has been extended to take the mutual interaction between multiple wells into account. It is independent in terms of location and type of the used transmitter. Hence, not only passive metal casings (excited by pure induction) but also active wells (galvanically connected to the transmitter) can be considered in the same way.
Despite being challenging for modelling and inversion, the presence of steel-cased wells also provides a number beneficial effects. As described in section 3 resolving hydrocarbon reservoirs usually requires to resolve thin resistive structures in a conductive overburden. The use of VED transmitters provides the highest sensitivity of all EM source types to such structures. Since vertical steel-cased wells can be regarded

as VED sources they help increasing sensitivity towards these resistive layers with any additional effort during the field surveys, hence increasing resolution power to such structures. In addition they act as additional EM sources at depth effectively moving the sources closer to the reservoir further increasing sensitivity at depth.
In order to maximize the beneficial effects of metal casings one should aim to maximize current strength along the wells. Of course most beneficial would be to attach the CSEM transmitter galvanically to the casing. If this is not possible due to logistical, or safety requirements one could still obtain large currents along the well by simply setting up the transmitter as close as possible to the casing using it as inductively coupled source extensions.
However, some minor and two major simplifications are made limiting this approach to first order effects only. First of all, the method of moments approach that is used as framework requires integration over Green's tensors. Since steel casings are several orders of magnitude longer than wide and at least for land based scenarios mostly vertical, deviations from verticality are neglected and integration is limited to the Γ_{zz} component of the Green's tensor. The second major limitation is considering the conductivity distribution in the subsurface. Analytic expressions of the Green's tensor do only exists for a homogeneous or layered halfspace. The latter usually relies on the recursive evaluation of reflection and transmission coefficients between the layers (Streich and Becken, 2011b). These coefficients are depended on source and receiver position, making analytic integration over various source depths difficult. Therefore the background conductivity distribution is limited to a halfspace approach. These two assumptions allows the integrals to be solved analytically. To overcome these assumptions one could evaluate the integrals numerically which would than allow for deviated wells in layered halfspaces which has been published by Kohnke et al. (2017). This would also allow this algorithm to include other steel infrastructure such as pipelines within the same framework. However, for large scale applications numerical evaluation of these integrals may be computationally expensive.
Furthermore steel is usually considered to have high magnetic permeabilities, however magnetic properties of steel have not been considered. In future application one might follow a similar strategy by replacing casings by a series of magnetic dipole sources.
A complete alternative approach overcoming most of the shortcomings of the presented algorithms would be implementing an approach given by Weiss (2017). There a hierarchical approach where conductivities inside the modelling domain are defined is realised. Mostly conductivities are defined on the volume of each grid cell. However it is also possible to define conductivities on edges or faces of the grid. By mixing these two approaches steel casings can be easily incorporated by aligning edges of the grid with the borehole position and assigning the edge corresponding to the casing a different conductivity then the adjacent cells. Although it was originally developed for finite element modelling it can be incorporated into FD modelling too. However, due to the inflexible mesh-design of FD including many boreholes or deviated wells will be impractical to impossible.
In any situation the presence of steel-cased wells has to be considered already in the planing phase before any CSEM experiment and also in the following modelling and inversion steps.

Chapter 5

Elongated receivers and its application to horizontal and vertical electric fields

Controlled Source Electromagnetics (CSEM) as many other electromagnetic (EM) methods relies on measurement of electric fields at discrete points at the earth's surface or in boreholes. Especially for hydrocarbon monitoring applications, the inline horizontal electric field at surface and the vertical electric field measured in shallow observation wells provide the highest sensitivity of all EM-field components towards thin resistive structures commonly associated with hydrocarbon reservoirs (see section 3.2 or Streich, 2016). Thus GFZ has developed a novel vertical electric field sensor which has been installed in a specially drilled shallow observation well (see section 3.3 or Tietze et al., 2018b).
Most modelling and inversion algorithms assume the electric field to be measured at a single point (Miensopust, 2017). However, it is not possible to measure electric fields directly. Instead, voltage difference U between two electrodes at a and b is measured and normalised by the electrode separation (dipole length, d) to obtain units of the electric field (Poll et al., 1989).

$$E = \frac{U_{ab}}{d} \tag{5.1}$$

The electric field at a point-dipole and measured over a finite length dipole are only identical if the electric field does not vary between the electrodes. Therefore two implicit assumptions are commonly made during modelling and inversion. 1) Variation of the electric field between the two electrodes is negligible. And 2) the physical dimensions of the receiver are small compared to the underlying modelling grid.
These assumptions are violated when vertical electric fields are measured in shallow observation boreholes. They are usually two orders of magnitude smaller than the corresponding horizontal electric fields at surface. This requires rather long dipole lengths ($\gtrapprox 100\,\mathrm{m}$) in order to increase the signal-to-noise-ratio above the noise floor.
Due to the large conductivity contrast (air-rock) at the earth's surface there exists a strong gradient of the vertical electric field close to the surface violating the first assumption. Furthermore due to the long dipole length and rather small required vertical discretisation near the surface ($\approx 5\,\mathrm{m}$) the receiver would span several Finite

Difference (FD) cells in vertical direction. In addition varying conductivity within the near surface will result in a discontinuous electric field. Such varying conductivities along the receiver could not be accounted before in the modelling and inversion algorithm of Grayver et al. (2013).
In contrast to receivers it is common practise to consider the true layout of kilometre long electric sources (e.g. Streich and Becken, 2011a), mainly because they are much larger and affect the response in the entire survey area. Whereas typical dipole length for classical land based horizontal electric field measurements in CSEM and Magnetotelluric (MT) are in the order of 10 to 100 m (Simpson and Bahr, 2005).
Hence, in the framework of my thesis I implemented a flexible approach allowing to consider true electric field receiver layout into the existing modelling and inversion codes.

5.1 Implementation

As shown in Streich and Becken (2011a) responses for elongated wire sources are obtained by integration of unit dipole responses over the entire length of the wire. Due to the reciprocity principle this must also be true for receivers. Therefore, the measured voltage between two electrodes at point a and b is equal to line integral of the electric field along the wire connecting the electrodes (e.g. Poll et al., 1989).

$$U_{ab} = \int_a^b \mathbf{E} \cdot \, \mathrm{d}\mathbf{s} \tag{5.2}$$

Clearly the assumptions mentioned before hold exactly only if the electric field between the electrodes does not vary. For DC-applications the obtained voltages becomes independent of the chosen path of integration. In the general AC-case however, induction effects inside the wire might alter the response depending on the wire trajectory. In order to mimic the procedure of obtaining the electric field during field surveys within the modelling and inversion, eq. 5.2 is normalised by the distance d between the two electrodes.
Assuming that one can evaluate the electric field at any point along the wire trajectory one can approximate the integral in equation 5.2 as illustrated in Fig. 5.1 by a summation of the dot product of the electric field and the wire trajectory at a number of sampling points $\mathbf{E}_{P_i}$.

$$E_{rec} = \frac{\int_a^b \mathbf{E} \cdot \, \mathrm{d}\mathbf{s}}{d} \approx \mathbf{Q}_{elong}\mathbf{E}_P \tag{5.3}$$

This summation can be expressed as matrix vector product of the electric field $\mathbf{E}_P$ and the matrix $\mathbf{Q}_{elong}$. The operator $\mathbf{Q}_{elong}$ encapsulates the wire geometry of the receiver and only needs to be evaluated once. In the case of multiple elongated receivers $\mathbf{Q}_{elong}$ becomes a sparse matrix. There will be as many rows as there are elongated receivers and the number of columns would be equal to the total number of sampling points for all receivers. The number of columns does also equal the total number of non-zeros in the matrix. Implementing a combination of classical point dipole receivers and elongated receivers is straightforward.
As shown in section 2 the total response at a single point is given as the sum of the

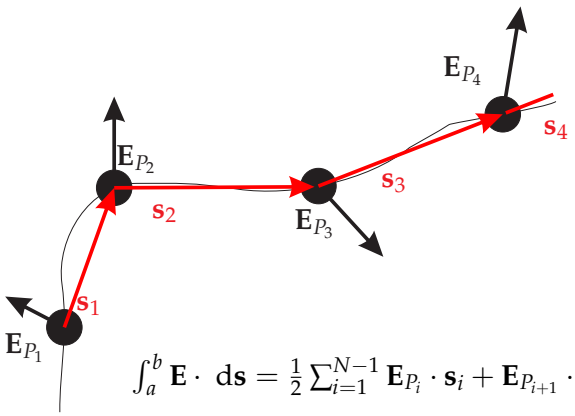

Figure 5.1: Sketch illustrating the summation operator (taken from Patzer et al., 2019)

primary field E_p and the secondary field E_s. While the primary field can be computed analytically, the secondary field is obtained by interpolation of the response on the modelling grid to the receiver position using the interpolation operator $\mathbf{Q}_E$ (see eq. 2.7). Hence, the total response of a number of elongated receivers is given by

$$\mathbf{E}_{rec} = \mathbf{Q}_{elong}\mathbf{Q}_E\mathbf{E}_{s,grid} + \mathbf{Q}_{elong}\mathbf{E}_{P,point}. \tag{5.4}$$

The product $\mathbf{Q}_{elong}\mathbf{Q}_E$ is only dependent on the geometry of the receiver itself and thus only has to be evaluated once during the entire inversion. In order to obtain sensitivities required during the inversion, equation 2.14 is multiplied with the summation operator $\mathbf{Q}_{elong}$

$$\mathbf{J} = \mathbf{Q}_{elong}\mathbf{Q}_E\mathbf{A}^{-1}\mathbf{G}. \tag{5.5}$$

5.1.1 Calculation of summation operator

To evaluate the entries of the summation operator the integral along the path is split into a sum of integrals between each two neighbouring sampling points P_i

$$\frac{\int_a^b \mathbf{E} \cdot \, \mathrm{d}\mathbf{s}}{d} = \frac{\sum_{i=1}^{N-1} \int_{P_i}^{P_{i+1}} \mathbf{E} \cdot \, \mathrm{d}\mathbf{s}}{d}. \tag{5.6}$$

Assuming only linear variation of the electric field between two sampling points and a straight wire between them one can rewrite the integral as

$$\int_{P_i}^{P_{i+1}} \mathbf{E} \cdot \, \mathrm{d}\mathbf{s} = \int_{x_i}^{x_{i+1}} E_x \, \mathrm{d}x + \int_{y_i}^{y_{i+1}} E_y \, \mathrm{d}y + \int_{z_i}^{z_{i+1}} E_z \, \mathrm{d}z. \tag{5.7}$$

For each direction the integral can be evaluated as follows

$$\int_{v_i}^{v_{i+1}} E_v \, \mathrm{d}v = \int_0^1 \left(\left(E_{v_{i+1}} - E_{v_i} \right) t + E_{v_i} \right) \left(v_{i+1} - v_i \right) \, \mathrm{d}t \, , v \in (x, y, z). \tag{5.8}$$

Where E_{v_i} and $E_{v_{i+1}}$ are the values of the electric field at the two sampling points in v direction while v_i and v_{i+1} are the corresponding coordinates of the sampling points. Finally this reduces to the following scalar product, which corresponds to the well known Newton-Cotes formula of degree 1.

$$\int_{v_i}^{v_{i+1}} E_v \, \mathrm{d}v = \frac{v_{i+1} - v_i}{2} \begin{bmatrix} 1 & 1 \end{bmatrix} \begin{bmatrix} E_{v_i} \\ E_{v_{i+1}} \end{bmatrix} , v \in (x, y, z) \tag{5.9}$$

The summation operator for one field component is then given by

$$Q_v = \frac{1}{2d} \left[\; v_2 - v_1 \quad v_3 - v_1 \quad \cdots \quad v_{i+1} - v_{i-1} \quad \cdots \quad v_{N-1} - v_N \; \right]. \tag{5.10}$$

5.2 Modelling Examples

In the following, different aspects of elongated receivers are demonstrated by a series of modelling studies. Most scenarios are based on the source-receiver setup from the field surveys across the Bockstedt oil field.

5.2.1 Horizontal Field Receivers

At first, modelling results of point dipoles and elongated dipoles are compared for a variety of scenarios. The first example shows a comparison of the responses of point dipole receivers and elongated receivers applied to surface based horizontal electric dipole (HED).

Based on the field set-up from the 2014 survey in the Bockstedt oil field the distribution of the horizontal electric field at the surface of a $3\,\Omega\,\mathrm{m}$ halfspace had been calculated for a number of frequencies and each transmitter. Figs. 5.2 a) and b) show the absolute value of the E_x-component for two different transmitters (active wires are marked by purple lines) and a frequency of 4 Hz. Clearly the typical radiation pattern of electric dipole sources is visible (see Fig. 2.5) including pronounced zero crossings where the electric field vanishes. Fig. 5.2 c) and d) show amplitudes as well as phases obtained for one receiver for a range of frequencies between 10^{-2} Hz and 10^2 Hz. The location of the receiver is marked by purple asterisk in a) and b). Responses are once calculated for a point dipole receiver (blue line in c and d) and once using an elongated receiver (orange asterisks in c and d) of 66 m length with its centre point coinciding with the position of the point dipole solution. In addition the relative difference of the absolute value between point dipole and elongated receiver is shown.

Differences between point dipole and elongated receiver are small for the first scenario shown in a) and c). They remain below 0.5 % over the entire frequency range from 10^{-2} Hz to 10^2 Hz. In the second example similar results are obtained for frequencies below 1 Hz. However, for frequencies above 1 Hz differences increase up to 7 %. These different behaviours are solely caused by the source-receiver geometry and the radiation pattern of the transmitter. In the first scenario (Fig. 5.2 a) the receiver is positioned far away from one of the zero crossings of the electric field and thus the spatial gradient of the electric field is small and the common assumptions made for point dipole receivers hold. In the second scenario shown in Fig. 5.2 b) the receiver is positioned right at one zero crossing of the electric field. This strong spatial gradient violates the assumptions made for point dipole receivers thus causing large differences. As the exact location of the zero crossing is frequency dependent (not shown here) not all frequencies are affected equally. Only for frequencies above 1 Hz the line of the zero crossing is intersecting the line spanned by the elongated receiver. Hence, high frequencies are more disturbed.

This first example shows that for classical HED-receivers dimensions can be neglected

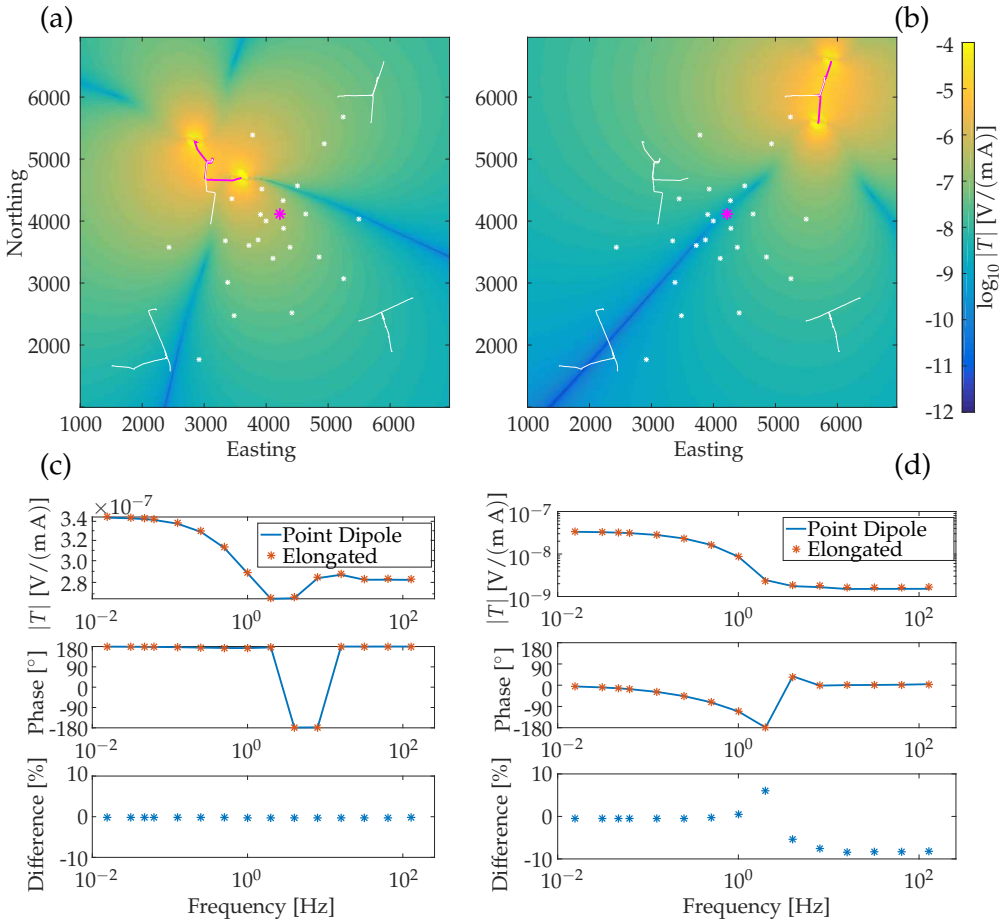

Figure 5.2: Two different scenarios comparing classical point HED solution and responses obtained for horizontal elongated receivers (taken from Patzer et al., 2019). a-b) Distribution of the absolute value of the T^{E_x}-component at surface. Active wire is marked as purple line. Responses are obtained for a 3 Ω m halfspace and a frequency of 4 Hz. c-d) Responses for a number of frequencies obtained at the corresponding receiver position (marked by purple asterisk in a) and b) for a point dipole receiver and a 66 m long elongated receiver. Centre point of the elongated receiver coincides with the position of the point dipole receiver.

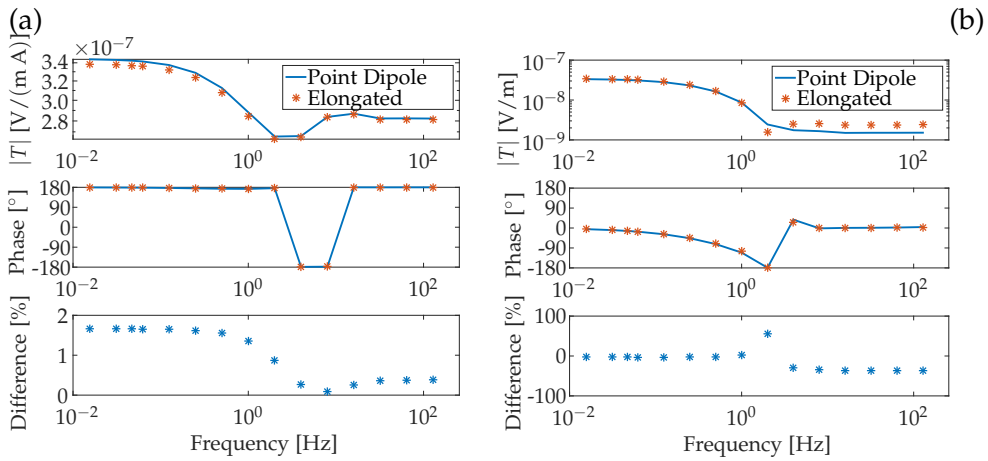

Figure 5.3: As before but now the elongated receiver is rotated by 1° from x-direction. Note the different scales in the difference panels.

during modelling and inversion if one avoids receiver positions at or close to one of the zero crossings. As these regions are rather narrow bands only a small subset of source-receiver configurations will be affected. Amplitude values are, in such situations, several orders of magnitude lower (as can be seen in Fig. 5.2 d) and thus more likely to be affected by noise. Therefore such data points have been commonly excluded from an inversion process.

Deviation from measurement axis

When setting up electric field receivers in the field, directions are commonly obtained by the use of magnetic bearing. As for any measurement the obtained directions will never be exact. As soon as the orientation of the measurement dipole deviates from the desired direction, undesired field components will be projected into the recorded signal. This is an additional effect that is implicitly considered when working with elongated receivers instead of point dipole receivers. Fig. 5.3 shows a similar study as before but now the elongated receiver is assumed to deviate by 1° from the x-direction. Again as shown in Fig. 5.3 a) the difference between the two receiver types is small when the electric field is measured far away from the zero crossings. However, differences are much larger compared to the scenario when the elongated receiver is perfectly aligned with the x-direction, varying between 0.1 and 1.6 %. Much larger differences occur when the receiver is positioned at the zero crossings. Since zero-crossings of the E_x-component coincide with the maximum of the E_y-component the projected undesired y-component can be as large as the desired x-component. Thus differences between the ideal x-oriented point dipole and the elongated receiver reach -36 % for the higher frequencies. This mapping of undesired field components into the measured signal becomes even more severe when considering vertical receivers as will be shown in a following section.

Galvanic Distortion in MT and CSEM

Due to the accumulation of charges at conductivity boundaries, the normal component of the electric field across such boundaries is discontinuous. Thus, in case that the

electric field receiver is spanning across such discontinuities the assumptions made for point dipole receivers are violated. An effect extensively studied in MT applications and commonly known as galvanic distortion or static shift (e.g. Jones, 1988; Jiracek, 1990; Chave and Smith, 1994). The following example illustrates that considering true receiver dimensions in MT can help mitigate some effects of galvanic distortion or static shift.
I used the Finite Element modelling software COMSOL to simulate the 2D MT response over two adjacent quarter-spaces of 10 and 100 Ω m (see Fig. 5.4 a). As only the E_y component will show discontinuous behaviour across the boundary only TM-mode simulations have been performed. Once the distribution of the y-component of the electric field has been computed, it has been exported and subsequently feed into the my interpolation scheme to obtain the electric field response of an elongated receiver in y-direction. Fig. 5.4 b) shows the obtained responses for the point dipole and the elongated receiver as apparent resistivity and phase curves over period. As expected, a frequency independent shift in ρ_a between the two receivers can be seen, while phases remain unaffected. This phenomenon has been extensively studied and various methodologies have been developed to mitigate this effect. Simply taking receiver dimensions into account during modelling and inversion could help to avoid these effects altogether. The only limiting assumption would be that it must be possible to make the underlying modelling grid small enough to be able to describe such small scale conductivity contrasts. Similar effects from obtaining disturbed electric field values due to lateral conductivity contrasts at surface are likely to be present in CSEM measurements too, however no studies investigating this effect have been published so far.

5.2.2 Vertical receivers

Finally different examples illustrating some aspects relevant for vertical electric field receivers are shown. At first the necessity of using elongated receivers when working with shallow vertical electric fields is highlighted. As discussed previously within the framework of the Enhanced Oil Recovery (EOR) project, a novel vertical electric field sensor has been developed and installed in the Bockstedt oil field (see section 3). Hence, most examples are based on the configuration of that particular receiver. Technical details of the receiver can be found in Tietze et al. (2018b). Three electrodes at three different depths (92, 140 and 188 m) are all measuring voltage differences against a reference electrode at surface. A sketch of the sensor configuration as it has been installed is shown in Fig. 5.5 a). The plastic casing of the borehole is slotted at the installation depths of the sensors allowing for galvanic connection to the surrounding rock formations.
For the *canonical layered halfspace model* (red line in b) the vertical electric field with depth is calculated in 1000 m distance in inline direction to an HED transmitter at surface. The blue line in Fig. 5.5 b) shows the distribution of the vertical electric field with depth. Green dots mark the responses obtained for elongated receivers spanning from surface to the corresponding installation depth of the lower electrode. The green line marks responses obtained for continuous installation depths.
The distribution of the electric field with depth indicates that the problems previ-

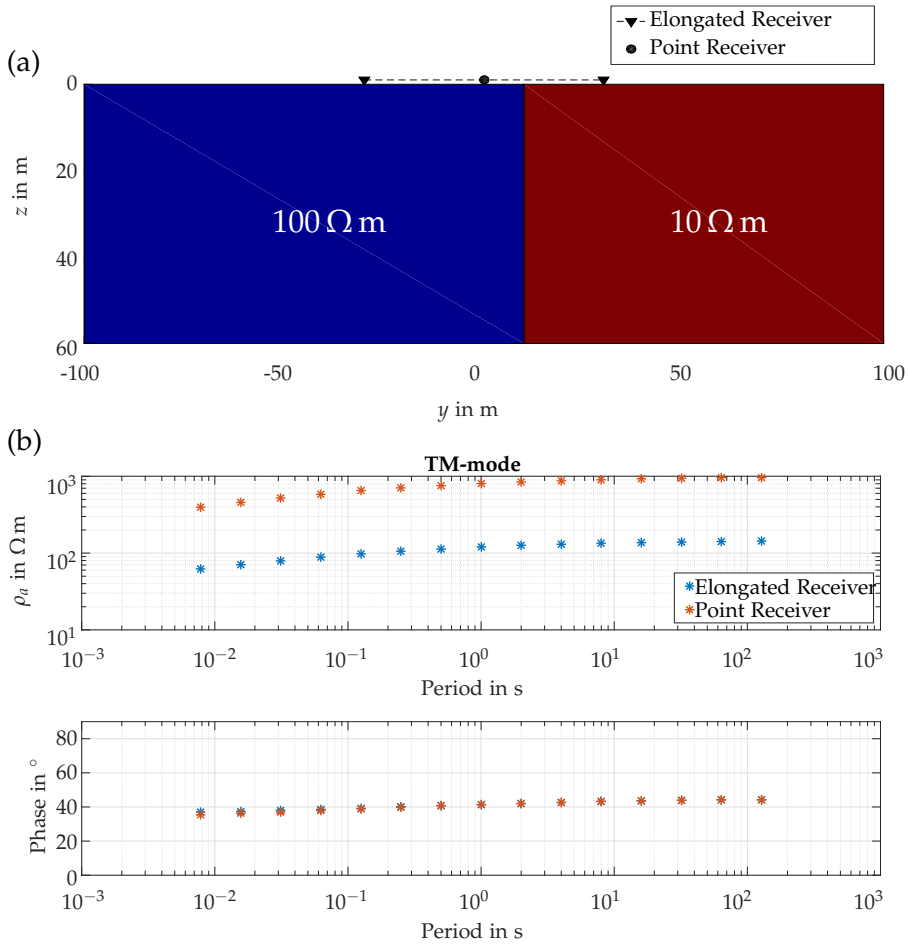

Figure 5.4: (a) Model used to calculate the 2D MT response using the finite element modelling software package Comsol. Electric and magnetic field values have been computed at the earth's surface for a number of periods and subsequently exported to compute MT impedances at the position of the marked point receiver. Electric fields have been once evaluated for a point dipole and once for an 60 m long elongated receiver spanning across the conductivity discontinuity. (b) MT responses as apparent resistivity and phase curves over period for the two different receivers. Only TM-mode responses are shown as only the TM-mode will be affected by galvanic distortion (taken from Patzer et al., 2019).

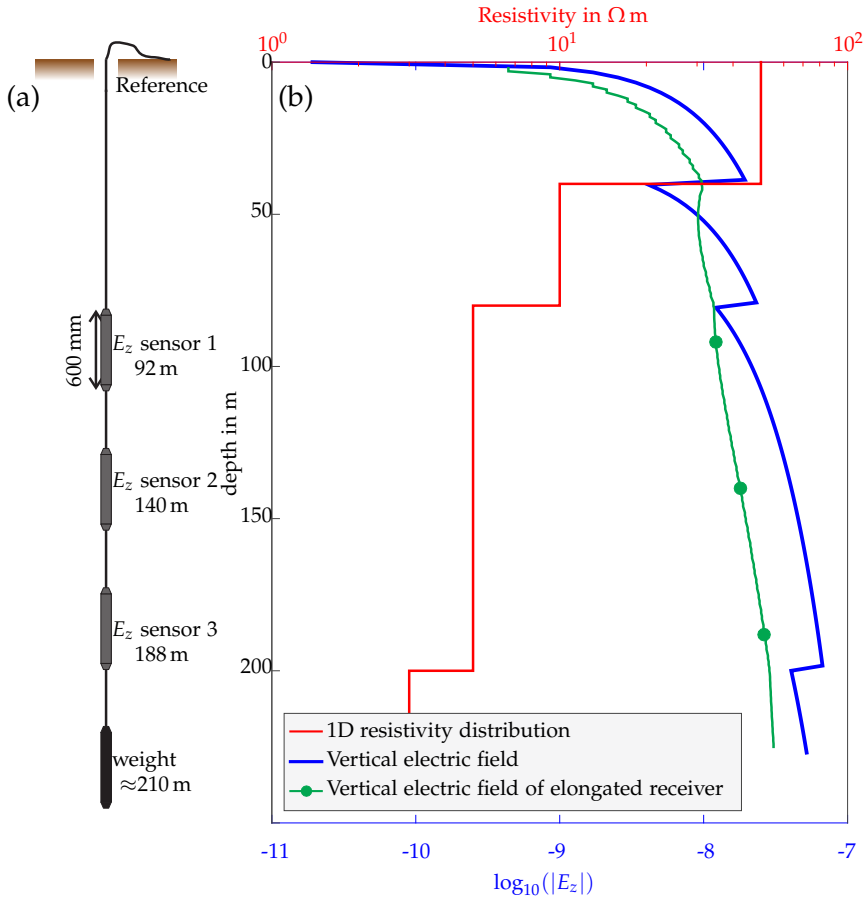

Figure 5.5: (a) Schematic setup of the vertical electric field receiver installed in the Bockstedt oil field. Three sensors in different depths measure voltages against a reference electrode at surface. (b) Distribution of the vertical electric field with depth (blue line) obtained for a 1 km long grounded HED transmitter in 1 km distance in inline configuration at a frequency of 1 Hz. The underlying layered conductivity distribution is shown by the red line. The green line shows the obtained responses for an elongated receiver spanning from surface to the corresponding depth. Green dots mark the depths of the three installed sensors in the shallow observation well drilled above the Bockstedt oil field (taken from Patzer et al., 2019).

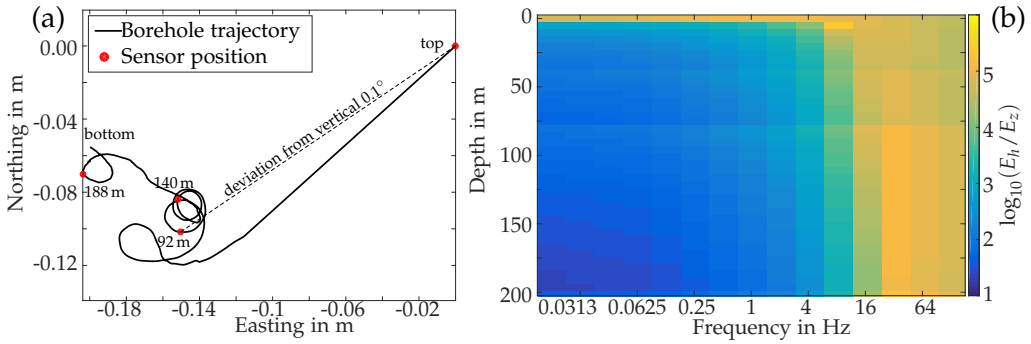

Figure 5.6: (a) Map view of the borehole deviation of the Bockstedt E_z receiver. Red dots mark the lateral position of the installed sensors. The label at each dot state the installation depth. (b) Ratio of the absolute value of the horizontal and vertical electric field with depth for a number of frequencies. Assuming the layered halfspace as well as transmitter orientation from Fig. 5.5 (see also Patzer et al., 2019).

ously discussed for horizontal field receivers are even more relevant for vertical field receivers. Assumptions for point dipole receivers are violated close to surface where the amplitude decreases to zero exponentially. In addition the electric field is discontinuous across layer boundaries. Considering that the response for elongated receivers is an integrative value, it varies smoothly with varying installation depth of the lower electrode. Naturally variations become weaker with increasing receiver length. Due to the small values of the electric field close to surface (less than $10^{-9}\,\mathrm{V\,m^{-1}}$) the obtained response of the elongated receiver is almost always smaller than the electric field at the depth of the lower electrode.

Verticality

In a similar fashion as the imperfect alignment in North-South and East-West direction of horizontal electric field receivers results in mapping of undesired field components into the measured signal (see Fig. 5.3), vertical field receivers will be susceptible to deviations from verticality. As any borehole deviates to some degree from verticality this effect of mapping of horizontal field components into the desired vertical component does always occur. Naturally one should aim to drill as vertical as possible if the well is thought to be used for vertical electric field measurements.

Fig. 5.6 a) shows the deviation from verticality of the shallow observation borehole installed in the Bockstedt oil field. Over the entire length of the well deviation is extremely small ($\approx$ 18 cm over 150 m). Considering the shortest dipole installed in the well, measuring from surface to 92 m depth, the average deviation is 0.1°. By most drilling standards this is considered as perfectly vertical.

Amplitudes of horizontal and vertical fields differ by many orders of magnitude (Tietze et al., 2015). Fig. 5.6 b) shows the ratio of the absolute values of the vertical and the horizontal electric field with depth and frequency for the upper 200 m along the receiver from the scenario shown in Fig. 5.5. In average the horizontal electric field is two orders of magnitude larger than the vertical field. At 200 m depth amplitudes are equal for the frequencies below 0.0625 Hz while they differ by five orders

of magnitude and more for high frequencies (> 64 Hz). Differences generally increase with frequency and decrease with depth. Especially close to surface differences reach again five orders of magnitude. Directly at surface the vertical electric vanishes while horizontal electric fields reach their maximum value.
This indicates that even such minuscule deviations of only 0.1° may alter the response compared to receivers being perfectly vertical especially for higher frequencies.

Comparison to Field Data
After discussing possible effects of deviations from vertical, based on modelling studies this is now examined for the obtained field data based on two different source-receiver configurations. Both examples show a comparison of transfer functions (TFs) of the field data from the 2015 survey for the shortest E_z-receiver (92 m dipole) and two model responses. Responses are obtained again for the *canonical layered halfspace* which had been shown to be a good 1D approximation for data obtained from horizontal field receivers.
The first scenario, shown in Fig. 5.7, resembles an inline configuration between the transmitter and the receiver. The two model responses were once obtained for a perfectly vertical elongated receiver (blue lines) and an elongated receiver taking the deviation from verticality into account (red lines). For frequencies below 1 Hz differences between the measured and both model responses in amplitude (see Fig. 5.7 a) as well as phase (see Fig. 5.7 b) are small. This shows that the used layered halfspace is a reasonable 1D approximation of the real 3D subsurface conductivity distribution. However, for frequencies above 1 Hz neglecting the deviation from vertical results in large amplitude differences of half an order of magnitude between measured data and model response. Amplitudes are explained however if the deviation is taken into account (red curve in Fig. 5.7 a). Nevertheless phases are still not explained for higher frequencies.
The second example (shown in Fig. 5.8) resembles a broadside configuration. Phases (shown in b) are explained well for both model responses at frequencies below 0.1 Hz. In order to explain the phases of measured data for higher frequencies the deviation has to be taken into account. If the deviation is not considered large phase differences up to 180° are observed. Regarding the amplitudes a frequency independent shift towards lower amplitudes is observed. For frequencies below 1 Hz amplitudes of the model response are approximately 2× smaller than the measured data if the tilt is taken into account and more than 3 times smaller if the deviation is not considered. Between 1 and 10 Hz amplitudes for the vertical receiver (blue line) decrease drastically by 2 orders of magnitude while the measured data increase. Considering the receiver tilt of 0.1° allows at least to follow the general shape of the curve.
These significant differences between the inline and the broadside configuration are mainly caused be the radiation pattern of the transmitter which resembles an HED. As shown in Fig. 2.5 the amplitude of the vertical electric field reaches its maximum value in inline direction to an HED transmitter, while it becomes zero in broadside direction. Hence, small deviations from vertical will affect broadside configurations more severely as the horizontal electric field component mapped into the desired vertical component has higher influence even for such minuscule deviations of only 0.1°.
Although the shown 1D modelling results were able to capture general aspects of

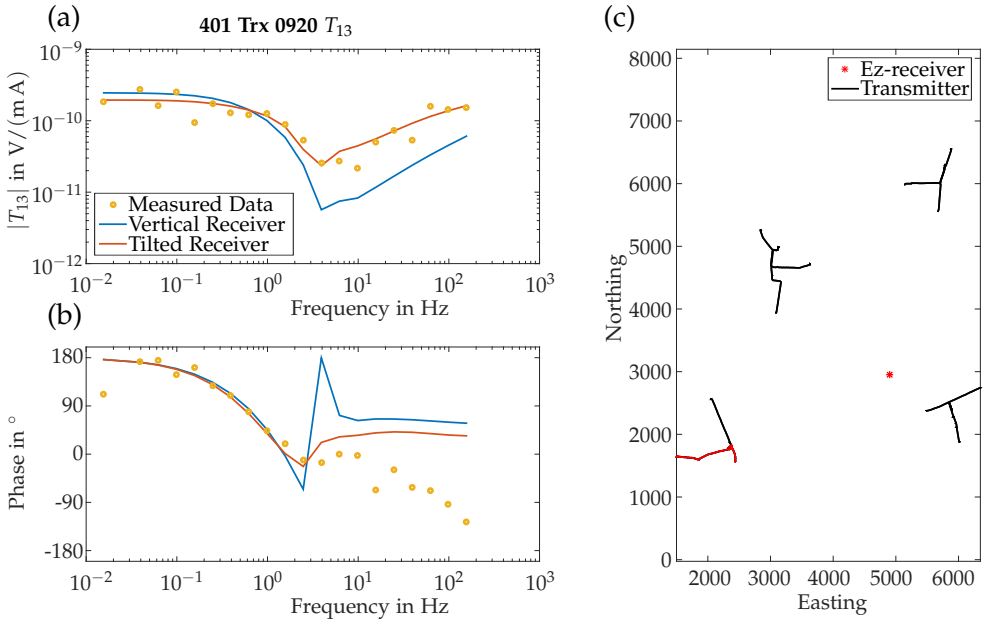

Figure 5.7: Comparison of field data from the 2015 survey (yellow circles) and modelled data assuming perfectly vertical elongated receiver (blue lines) and an elongated receiver taking the deviation into account (red lines) (taken from Patzer et al., 2019). Shown are results for the shortest dipole (92 m) of the three installed receivers. (a) Absolute value of one TF over frequency for one transmitter. (b) Phases of the same TF over frequency (c) Map view showing the source-receiver configuration. The two active wires of the transmitter corresponding to the TF are marked by red lines. Transmitter and receiver roughly follow an inline configuration. Modelling results are based on the layered halfspace background model obtained from MT measurement across the oil field, see section 3.2.

the measured data some differences between modelled and measured data remain. Differences may be caused by small scale conductivity heterogeneities which could not be captured by the *canonical layered halfspace* conductivity model. Especially high frequencies are likely to be affected by inhomogeneities near the receiver.

5.3 Inversion Examples

Finally different aspects of 3D inversion using elongated vertical receivers are shown. For this, synthetic data have been generated using the setup and resistivity model shown in Fig. 5.9. Again the setup is adopted from the CSEM field survey 2014. In contrast to the setup from the previous section all horizontal electric field receivers are exchanged by vertical electric field receivers and no steel casings are considered. As another complication each receiver deviates from vertical by a random angle between 0 and 1° with also random azimuth. The conductivity model is identical to the conductivity model used in section 4.4, with the *canonical layered halfspace* as background and a 30 m thick resistive (100 Ω m) reservoir in 1200 m depth.

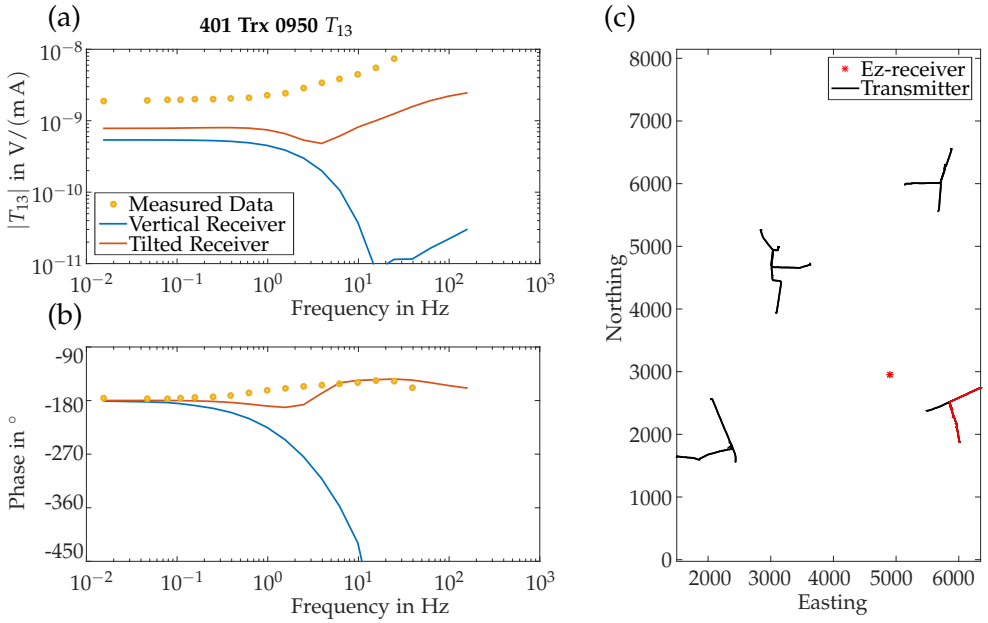

Figure 5.8: Comparison of field data (yellow circles) and modelled data assuming perfectly vertical elongated receiver (blue lines) and an elongated receiver taking the deviation into account (red lines) (taken from Patzer et al., 2019). Shown are results for the shortest dipole (92 m) of the three installed receivers. (a) Absolute value of one TF over frequency for one transmitter. (b) Phases of the same TF over frequency (c) Map view showing the source-receiver configuration. The two active wires of the transmitter corresponding to the TF are marked by red lines. Transmitter and receiver roughly follow a broadside configuration. Modelling results are based on the layered halfspace background model obtained from MT measurement across the oil field, see section 3.2.

5.3.1 Sensitivity

The resolution capabilities of any inversion is mainly controlled by the sensitivity. It is therefore worthwhile to show differences in the sensitivity pattern between HED receivers and elongated vertical electric dipole (VED) receivers before discussing the inversion results. Fig. 5.10 shows the normalised sensitivity for one source-receiver combination (transmitter and receiver position marked in purple) of the setup shown before. Sensitivity has been calculated using the *canonical layered background* model. Shown is the sensitivity pattern at 900 m depth for a) an HED receiver and b) shows the sensitivity distribution if the receiver would be replaced by a randomly tilted VED receiver.

In general sensitivity is spread out over larger areas throughout the model domain for the HED case than in the VED scenario (more greenish colours in a) compared to the more blueish colours in b). Over large parts of the model differences are about one order of magnitude. In both scenarios maximum sensitivity is reached below the transmitter and the receiver (yellow colours) and is decreasing with increasing distance to either transmitter or receiver. While the maximum values below transmitter and receiver are of similar amplitude in the HED scenario a), amplitudes below the

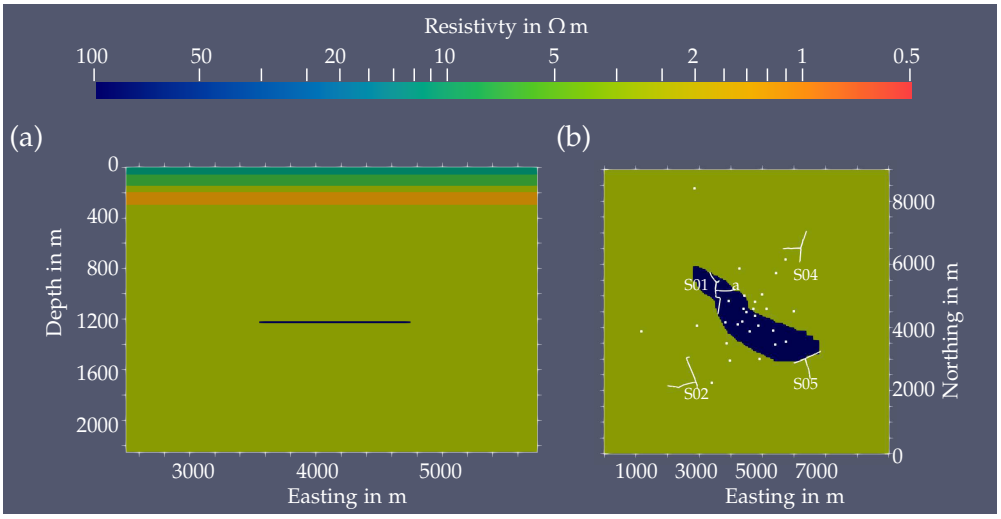

Figure 5.9: True Model for the following inversion (as shown in Patzer et al., 2019). The model as well as source-receiver orientation is identical to the scenario shown in Fig. 4.12. Difference is that instead of horizontal electric field receivers, vertical electric field receivers are used. Each receiver spans from surface to 200 m depth. In addition each receiver deviates from vertical by a random angle between 0 and 1° with random azimuth.

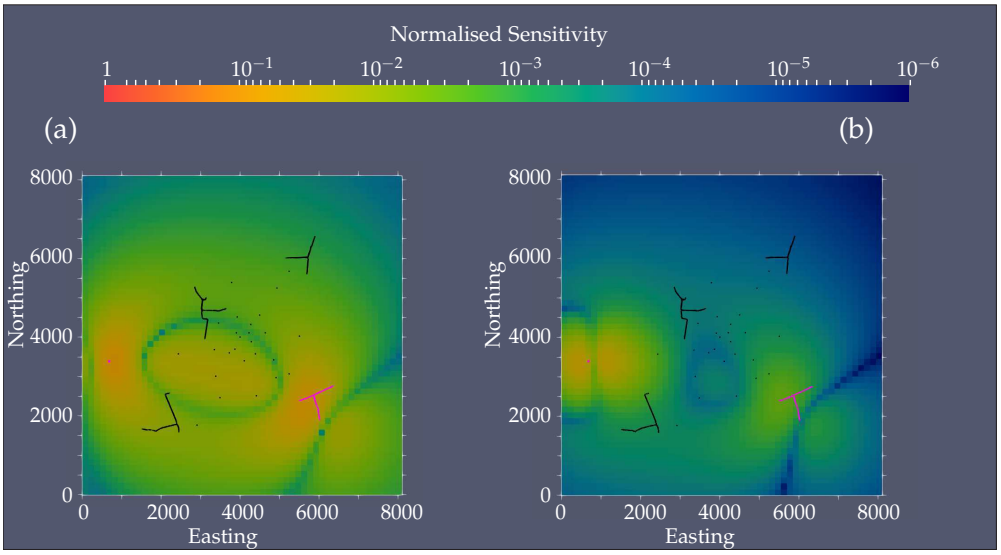

Figure 5.10: Comparison of the distribution of normalised sensitivity for (a) HED receiver and (b)VED receiver. Shown is a horizontal slice at 900 m depth (taken from Patzer et al., 2019).

receiver are approximately one order of magnitude higher than below the transmitter in the VED scenario.
As this observation generally holds for all source-receiver combinations one can conclude that sensitivity will be more focused below the receiver when using vertical receivers while it is more spread out over larger volumes for classical surface based horizontal electric field receivers. As a consequence one can say that horizontal receivers allow to sense larger volumes than vertical receivers. However due to the focused sensitivity distribution, E_z-receivers may be more suitable to resolve small lateral resistivity variations if situated just above the resistivity contrast. This allows E_z-receivers to be of particular use for monitoring applications where only small scale resistivity variations in rather small localised areas are expected, while horizontal receivers may be of particular use in exploration campaigns and in obtaining the baseline model for any time-lapse study.

5.3.2 Inversion result

For each source-receiver combination the two strongest TF have been used in the following inversion. All data have been contaminated with 3 % Gaussian noise. Six logarithmically spaced frequencies between 0.0156 Hz to 2.4764 Hz have been used. In case of 27 shallow observation boreholes one can assume to have good knowledge of the general background structure and in particular of the shallow subsurface structure. Hence, the starting model was as before the true *canonical layered halfspace* background model. In order to evaluate the influence of vertical receivers on the inversion compared to classical HED receivers, inversion results using both receiver types are shown in Fig. 5.11. For both scenarios the setup shown in Fig. 5.9 was used which resembles the layout of the CSEM field surveys.
Both inversions use the same parameters that have already been used in the inversion example discussing the effect of steel-cased wells (see section 4.4), including Tikhonov regularisation and in order to increase sensitivity towards the reservoir the same additional model weighting scheme (see section 6) has been applied. The weight of all cells below 1300 and above 1100 m (100 m above and below the reservoir) has been reduced to 0.5 while weights of all other cells is set to 1. The discretisation is the same as before with cells of $150 \times 150 \times 50\,\mathrm{m}^3$ at depth.

Fig. 5.11 a) and b) show the final models for both scenarios while c) and d) show initial and final misfit as histogram respectively. In general both inversions were able to recover the central part of the reservoir well, while the resolution decreases towards the edges. In both cases the absolute value of the resistivity is generally underestimated. In the central part of the reservoir resistivity is largest $< 50\,\Omega\,\mathrm{m}$. Due to data coverage the north-western part could not be resolved in either of the two scenarios, while the south-eastern edge could not be recovered by the use of horizontal receivers. Using vertical receivers, a second resistive feature is imaged resembling more the true model. This second resistive feature is situated just below two south-eastern most vertical receivers. The two inversion results differ further in the horizontal extent of the imaged reservoir perpendicular to the strike direction. Especially the north-eastern edge of the reservoir seems to be better resolved using E_z-receivers while it is not as well confined within the outline of the reservoir for horizontal field receivers. Due to

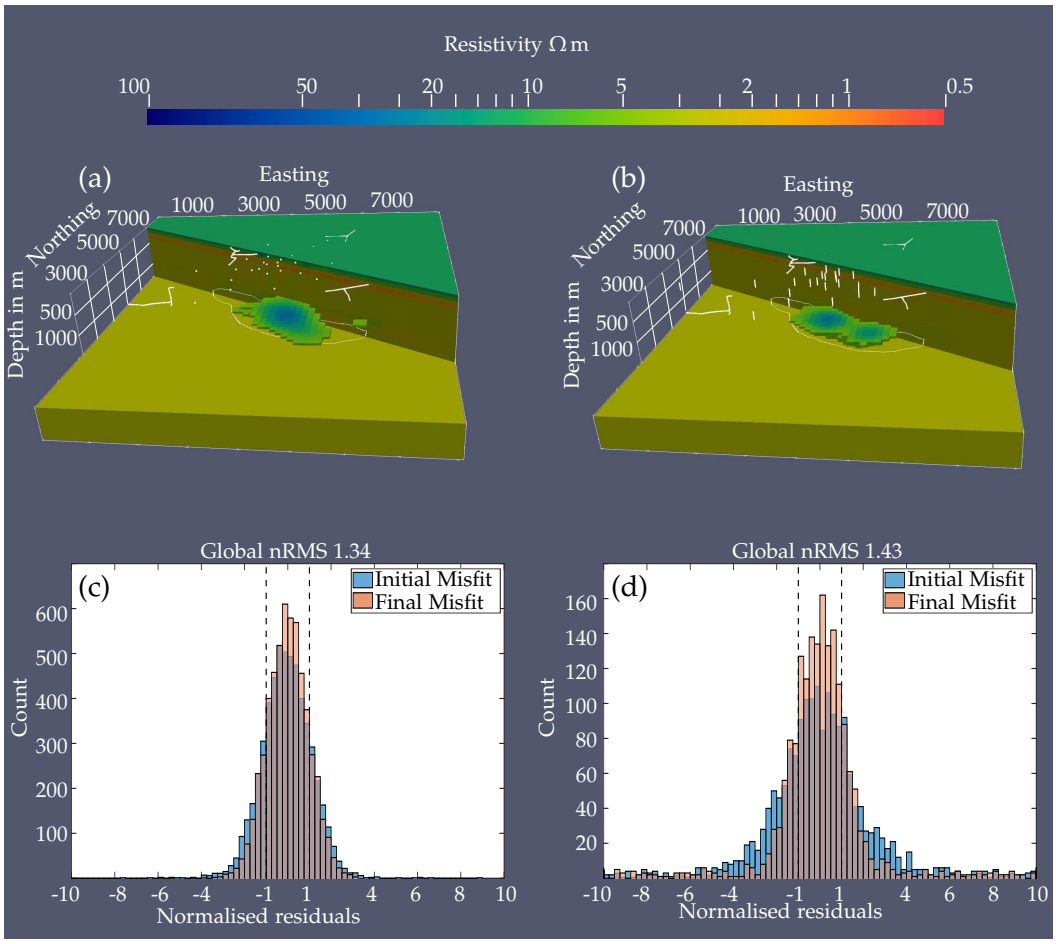

Figure 5.11: Inversion results as comparison between classical HED receivers and elongated VED receivers. True model for both inversions is shown in Fig. 5.9. All inversion parameters are kept the same. The only difference is the type of receiver. (a) Final model after 25 iterations for the HED scenario. (b) Final model after 25 iterations for the VED scenario. Below 600 m all cells above 5 Ω m are kept visible. (c,d) Histogram of normalised residuals distribution for all data points for the initial and final model for the HED and the VED scenario respectively. Greyish colours show where histograms overlap. Target misfit of ±1 is marked as black dashed line (see also Patzer et al., 2019).

the spotlight-like sensitivity distribution of vertical receivers in contrast to the more spread out distribution of horizontal receivers, it is easy to understand the better lateral resolution of the inversion result shown in Fig. 5.11 b).
Final and initial misfit for both scenarios are shown Fig. 5.11 c) and d). As true model and starting model only differ by the presence of the resistive reservoir, the initial misfit is an indicator of the sensitivity of the chosen setup towards the reservoir. Especially for the horizontal electric field receivers (Fig. 5.11 c) most of the normalised residuals are within the target misfit of ±1 already for the starting model, suggesting only little sensitivity to the actual reservoir. In contrast the spread of the distribution is larger for vertical receivers. This is another indication for the superior resolution

capacities of vertical receivers for a thin resistive reservoir.
At this point one has to point out that the source-receiver layout was simply adopted from the field surveys. Survey design for the field measurements had been optimised for detecting small scale resistivity variations in the centre part of the model, hence the poor resolution towards the edges of the reservoir. In order to compare different resolution characteristics between HED- and VED-receivers I simply exchanged all horizontal receivers by vertical receivers. Due to the different sensitivity characteristics and resolution capabilities both receiver types will require different survey layouts to obtain highest resolution capabilities. In addition measuring vertical electric fields require expensive drilling operations including unconventional plastic casings and require high demands on the verticality of the drilled wells. Thus in reality working with 27 vertical field receivers separated by each other by only a few 100 m may not be feasible.

5.4 Summary and Discussion

The traditional way of measuring the electric field over finite dipoles and subsequent assignment of the obtained response to a single point, implies two assumptions on the behaviour of the electric field between the electrodes and the underlying modelling grid. Receiver dimensions are negligible if the variation of the electric field between the electrodes is small compared to the receiver dimensions. And the dimensions of the underlying modelling grid is larger than the electrode separation. Especially vertical electric field measurements require long dipoles (≈ 100 m) in order to increase the signal-to-noise ratio above the noise floor, violating these assumptions.
The newly implemented description of electric field receivers now allows interpretation and inversion of vertical electric field data measured over long dipoles. The approach is flexible and allows handling of arbitrarily oriented and shaped receivers and can be applied as such also for conventional HED receivers. As it requires mainly one additional product of sparse matrices the numerical overhead is rather limited. The general approach is not limited to land based CSEM applications but may be transported to other electromagnetic (EM) methods easily. Furthermore it is not limited to frequency domain applications but can be used in time-domain applications as well.
It has been shown that for most conventional HED receivers neglecting the dimensions of the measurement dipole is feasible except in certain unfavourable source-receiver orientations. The fields generated by HED transmitters typically exhibit narrow regions of strong gradients of the electric field (cf. Fig. 2.5). Those source-receiver configurations where it can not be neglected usually coincide with such zero crossings of the corresponding electric field component. In addition fields measured at such locations suffer from poor signal to noise ratio. Hence data obtained for these configurations are more likely to be affected by noise and have been traditionally excluded from further inversion processes. As these zero crossings are confined within narrow bands only a small amount of source-receiver combinations is usually effected by this. However by incorporating the receiver dimensions into the inversion it is now possible to include data that would have been previously neglected during the follow-

ing inversion. In order to allow for consideration of receiver geometry, positions of electrodes have to be documented during the field survey.
Strong gradients in the electric field also occur across conductivity boundaries. Receivers spanning across such discontinuities causes distortion effects commonly known as galvanic distortion or static shift in MT. I have shown in Fig. 5.4 that considering receiver dimensions in Magnetotelluric modelling may help to prevent some effects of galvanic distortion or static shift. Similar effects may occur in CSEM but have gained only little attention so far.
Similar effects are of even greater importance for vertical electric field measurements. As the vertical electric field is small, long dipoles (>100 m) are required. As the modelling grid near the surface has to be made rather small in vertical direction near the surface ($\approx$ 5 m) the receiver inevitably spans several grid cells. This is combined with a large gradient of the vertical electric field close to surface due to the air-rock boundary. In addition conductivity of the shallow strata is expected to vary due to the penetration of aquifers and other mainly layered sediments.
These findings are predominantly relevant for land based or airborne measurements applications as in marine environments electric fields are measured inside the water column away from any discontinuities in the electric resistivity.
In addition the implemented algorithm considers the projection of undesired field components into the measured signal once the receiver is not perfectly aligned with the direction of the desired field components. Again this is especially important for vertical electric field measurements. As boreholes are never perfectly vertical but will always deviate from verticality to some degree, mapping of the undesired horizontal components into the measured signal can not be neglected, especially in combination with the large mismatch in amplitudes of horizontal and vertical field components. Fig. 5.7 and 5.8 show the significance of this effect based on field data from the Bockstedt oil field, although the installed Ez-receiver deviates by only 0.1° from verticality. Not being able to consider these effects would effectively prohibit the use of vertical electric field data in inversion.
Although less prominent similar effects also occur for conventional HED receivers. As shown in Fig. 5.3 deviations of 1° of a 60 m long horizontal receiver may alter the response by 2 % for favourable source-receiver geometries compared to the case where deviation is not considered. This effect becomes larger (several tens of %) if the receiver is positioned at or nearby the previously mentioned zero crossings.
Finally I showed the correctness of the implementation within the inversion using synthetic data. It has been demonstrated that vertical electric field receivers do provide higher resolution towards a thin resistive reservoir. A sensitivity study comparing the sensitivity distribution of horizontal and vertical electric field receivers (see Fig. 5.10) has been carried out. For horizontal field receivers sensitivity is in general distributed over larger areas showing maximum sensitivity below the transmitter and the receiver. While for VED it appears to be much more focused in smaller volumes mainly below the receiver showing a "spotlight"-like characteristic. This suggests higher resolution capability for vertical receivers which can be exploited in particular for monitoring applications. As installing Ez-receivers on land requires expensive drilling operation the distribution of sensitivity is of great importance to optimise the source-receiver geometry.

Chapter 6

Time-lapse inversion

In monitoring applications usually a series of datasets at the same location at discrete times, in the following referred to as time-steps, is obtained. The aim of time-lapse inversion is to obtain a series of 3D conductivity models for these datasets which represent individual snapshots in time of the conductivity structure at each time-step. Comparison of these snapshots allows to track changes in the subsurface conductivity structure (e.g. as a result of oil production or brine flushing).

6.1 A reference time-lapse dataset

In the following a synthetic reference time-lapse dataset is introduced which is used for all numerical examples shown in this section. It is based on the source receiver setup from the field surveys across the Bockstedt oil field as shown in section 3.3. And has already been used to highlight the influence of steel-cased wells on 3D Controlled Source Electromagnetics (CSEM) inversion (see section 4.4) and in some variations to highlight the benefits of using vertical electric field receivers for resolving thin resistive structures at depth (see section 5.3).
The corresponding true models of both time-steps are shown in Fig. 6.1. As background model for both time steps the *canonical layered halfspace* is used. Resistivity at surface is 12 Ω m and decreases with depth. In 300 m depth there is a highly conductive layer of 1 Ω m and 100 m thickness. The conductive layer is followed by a 3 Ω m halfspace. The model of time-step 1 is identical to the true model shown in Fig. 4.12. In 1200 m depth a 15 m thick reservoir is situated following roughly the outline of the Bockstedt oil field. In the first or initial time-step (Fig. 6.1 a) the reservoir is assumed to be completely oil-filled and thus has a resistivity of 100 Ω m. In the second time-step (Fig. 6.1 b) half of the reservoir has been partly produced and thus resistivity decreased to 16 Ω m. In addition the galvanically connected 1500 m deep steel casing is added in most scenarios considered. In total four transmitters are used together with 27 receivers for horizontal electric fields.
For both time-steps synthetic transfer functions (TFs) have been calculated. In order to highlight the difficulties involved in resolving changes in such a deep and thin structure in a conductive overburden a comparison between the two datasets is shown in Fig. 6.2. Shown are the obtained differences of TFs for one polarisation of transmitter S05 for all receivers as well as all frequencies. The corresponding active wires of the

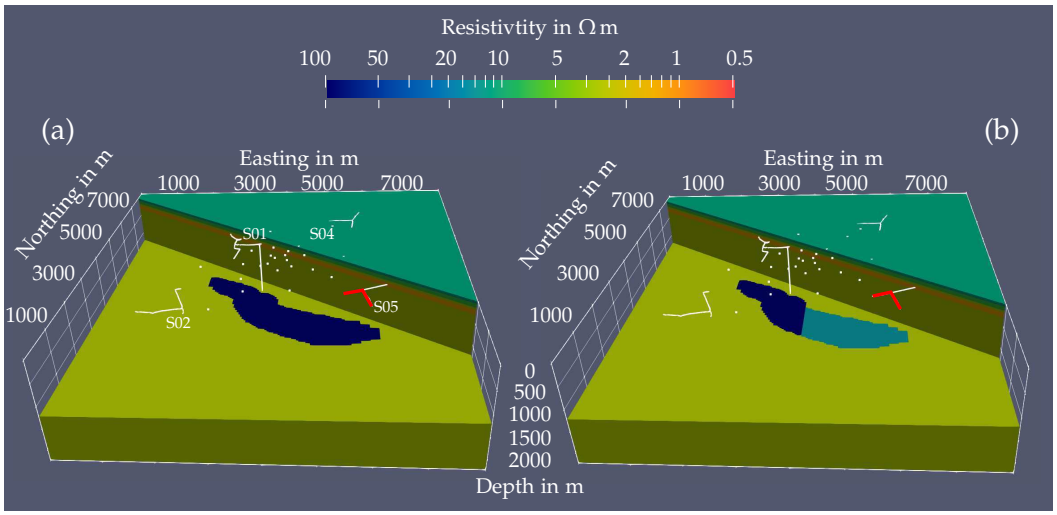

Figure 6.1: True models of synthetic time-lapse dataset used to test various inversions settings. a) Model corresponding to time-step 1 representing a fully oil filled resistive (100 Ω m) reservoir. b) Model corresponding to time-step 2 representing a partially produced reservoir. Resistivity decreased to 16 Ω m in south-eastern half of the reservoir. Reservoir outline follows the outline of the Bockstedt oil field. Source receiver layout is taken from the 2014 field survey. Background conductivity model for both time-steps is the *canonical layered halfspace*. The two marked wires of transmitter S05 correspond to T_{23} for which differences of time-lapse data are shown in Fig. 6.2.

shown TF are marked in red in Fig. 6.1. Shown is the relative difference of amplitudes between both time-steps in Fig. 6.2 a) as well as the absolute difference in phase in Fig. 6.2 b). Positive deviations are marked by blue colours and negative deviation by red colour. In general changes are only visible for lower frequencies as indicated by the colour saturation or lack thereof for higher frequencies. Changes in TF amplitudes are generally not visible for frequencies above 5 Hz. Below 1 Hz however, a small decrease in amplitude is visible for almost all shown source-receiver-configurations. Nevertheless changes are small not reaching 5 % for most combinations. Similarly phases do not change for high frequencies above 5 Hz. In addition phases are only affected by the change in the reservoir resistivity within a narrow frequency band of approximately one decade. As due to the skin effect high frequency signals decay faster with distance to the source, thus only signals of frequencies below a certain threshold value of approximately 5 Hz are sensitive towards changes in the reservoir which confirms findings of other authors like Tietze et al. (2015).
The shown example marks the transmitter response which is most influenced by the change in resistivity. Changes obtained for the other transmitters are even smaller. The presented differences are obtained for noise-free data. After adding 3 % Gaussian noise to both datasets the challenge of resolving changes in data of less than 5 % in only a small sub set of data becomes apparent. This indicates that one is operating close to the resolution limit for this particular setup.

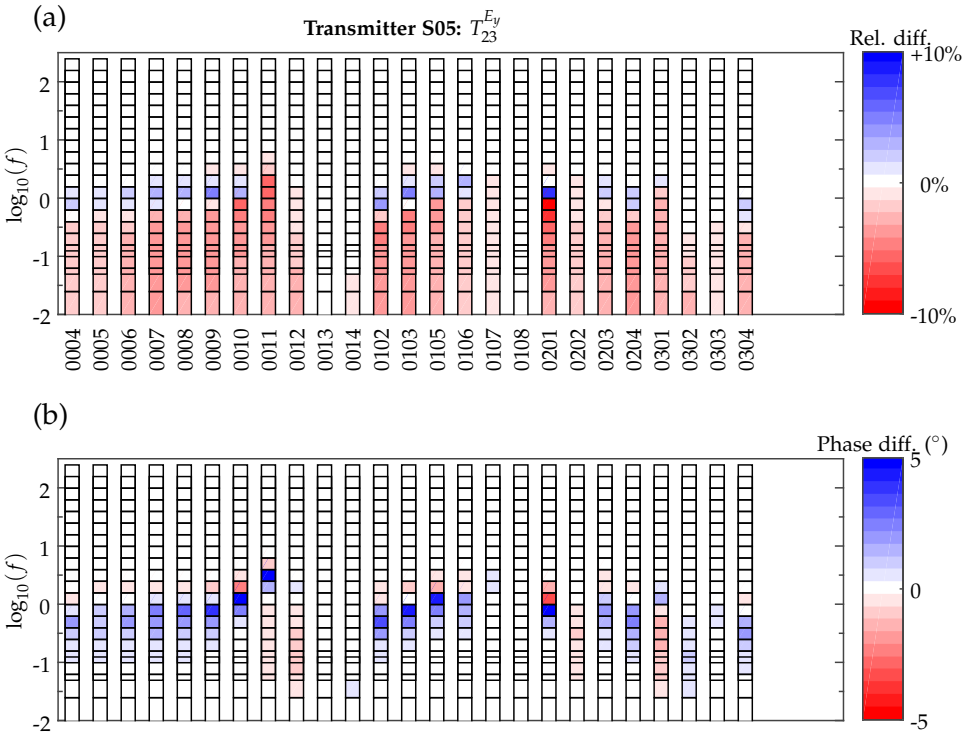

Figure 6.2: Time-lapse difference of synthetic data for the two time-steps shown in Fig 6.1, for the south-eastern transmitter S05, one TF and field component and all receivers and all frequencies. One column represents all values obtained for one receiver while each box shows values obtained for one receiver and one frequency. (a) Shows changes in amplitude as relative changes in (%) while (b) shows changes in phase as absolute changes in (°).

6.2 Choice of time-lapse methodologies

In principle snapshots of each time-lapse dataset can be achieved by applying an individual 3D inversion to each dataset and subsequently comparing individual 3D models. Such a procedure, however, does not exploit the temporal correlation between datasets and conductivity models. The obtained images typically result in huge ambiguity in the solution space and generally poor resolution of conductivity changes over time. Hence, various techniques have been developed to transfer temporal relations between datasets and conductivity structures into mathematical constraints for 3D time-lapse-inversion.

6.2.1 Data space approaches

Data-space techniques reduce dimensionality of a problem by linear mapping of the data to a lower-dimensional space in such a way that the variance of the data in the low-dimensional representation is maximized.
The most commonly used time-lapse methodology is referred to as difference inversion. Although most suitable for linear inverse problems like travel-time tomography

(e.g. Ajo-Franklin et al., 2007) the difference inversion approach has been used successfully for non-linear problems like ERT (LaBrecque and Yang, 2001) and even joint inversion of ERT and GPR (Doetsch et al., 2010). There the change between two datasets of two time-steps is used as input into the inversion and it is attempted to explain these differences by changes in the underlying conductivity distribution. Since input for this technique is the difference of datasets between two time-steps, repeated systematic errors in the measured data are removed from the time-lapse inversion process.
However, due to the non-linearity of the CSEM inverse problem errors introduced into the modelling and inversion may result in different responses depending on the resistivity distribution. E.g. improper modelling of steel-cased wells as discussed in section 4 may result in different EM-field responses due to the non-linear coupling with the conductivity of the surrounding formations. In addition as for example stated by Dadashpour et al. (2008) for seismic time-lapse difference inversion this method is generally very dependent on the quality of the starting/baseline model.
More importantly this approach is inherently unable to deal with a changing source-receiver setup between the time-lapse surveys. Especially if one is considering that repositioning errors of the sources or receivers of only 10 m can result in differences in TF amplitude of more than 20 % and phase differences of more than 10°, which are entirely unrelated to changes of subsurface structures, as discussed in Tietze et al. (2018b). This means that the expected time-lapse differences are much smaller than possible differences introduced due to relocation errors between surveys. Ideally sources and receivers should be installed permanently to overcome this issue. In the framework of the EOR-project (see chapter 3) however, sources and receivers had to be redeployed between surveys (see section 3.3). Other data space approaches like the ratio inversion proposed by Daily et al. (1992) suffer from similar shortcomings. I therefore disregarded the difference inversion in particular and all data space approaches in general from possible time-lapse methodologies.

6.2.2 Model space approaches

Approaches in model-space enforce temporal coherency of 3D models at individual time-steps by applying constraints on the set of models.
Hayley et al. (2011) proposed a Simultaneous inversion. There for each time-step 3D inversions can be run in parallel where an additional regularisation term is applied which forces the models of each time-step to stay "similar" to each other. The approach is based on the assumption that underground structures do not change "wildly" over time but gradually and/or localised. Note that, the regularisation works in time domain and acts like an acausal filter. This means side-effects can occur where data of the future can alter the model of the past. Since there is no correlation between the data of different time-steps directly evaluated, changing source receiver setup is taken into account in a straight forward manner. On the downside, this approach requires huge amounts of computational resources as 3D inversions for all time-steps have to be run in parallel and updates of each time-step is coupled with updates of all other time-steps. A single 3D CSEM inversion requires already approximately 100 GB of memory and 4 days computing time on a high performance cluster using 64

parallel processes.

Cascaded inversion
Based on the above considerations, I focused my work on a cascaded inversion approach. The general idea of this methodology is to constrain the inversion at any time-step by using the final model of the previous time-step as starting and reference model for the inversion of the current dataset. Causality of this method is ensured inherently and computational demands are kept at manageable levels. Since individual inversions are only linked by the final/starting models changes in source-receiver setup can be taken into account in a straight forward manner. A problem of the method is that artefacts tend to propagate from one inversion to the next. Once introduced, they become part of the a-priori information, which is fed into all subsequent time-steps. To identify suitable time-lapse inversion workflows and inversion parameter settings, the cascaded inversion approach was extensively tested based on the synthetic reference time-lapse dataset.

6.3 Regularisations

Any inversion is inherently mathematically ill-posed (Tikhonov and Arsenin, 1977). Therefore an additional regularisation is added as shown in 2.9. As the model regularisation term can be regarded as constraints towards the model, it can be used to force the model to obey specific assumptions. The following regularisations have been tested if they are suitable for time-lapse inversion.

6.3.1 Smoothness constraint regularisation

The most commonly used assumption is that conductivity values should vary continuously in space. An assumption commonly referred to as *Occam's razor*. A smoothness constrained inversion seeks to keep transition between areas of high and low resistivity continuous. The functional was introduced by Constable et al. (1987) and is given by

$$R(\mathbf{m} - \mathbf{m}_{ref}) = ||\nabla^2 \left(\mathbf{m} - \mathbf{m}_{ref}\right)||^2. \tag{6.1}$$

By adding an additional reference model, sharp contrasts between neighbouring cells can be introduced as a-priori information. In addition weights for the smoothing in the three Cartesian directions can be given to decrease or increase smoothing in certain directions, e.g. higher weights in the horizontal direction and lower weight in vertical direction will result in more layered structured models. However, if not part of the reference model smooth inversion is inherently unable to resolve sharp contrasts of conductivity changes which are ubiquitous in nature (e.g. faults separating different geologic units, well defined mineral deposits in the surrounding host rock, confined aquifers etc.). In the case of hydrocarbon reservoirs one can assume the resistive reservoir to have well defined boundaries to the surrounding rock formations.

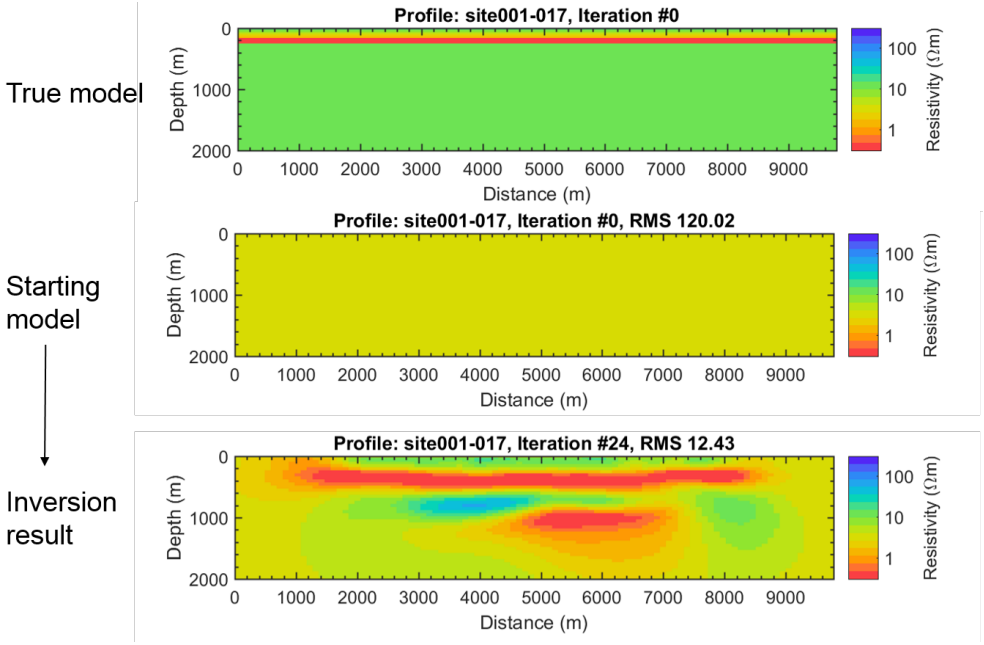

Figure 6.3: Inversion model using smooth inversion showing overshooting effect

Oscillatory behaviour

Most notably, when working with smoothness constraint inversion, I had observed that it tends to produce artificial layering, oscillating between high and low resistivity. An example based on synthetic data illustrating this effect is shown Fig. 6.3. Synthetic data have been created for the true model shown in the upper panel. The true model similar to the *canonical layered halfspace* but with genrally increased resistivity values. The source-receiver layout is again taken from the 2014 field survey across the Bockstedt oil field.

A smoothness constraint inversion has been carried out starting from a 10 Ω m halfspace (middle panel). The final model after 24 iterations is shown in the lowermost panel. The highly conductive layer near the surface could be recovered well. But The conductive layer is followed by artificial resistive layer followed again by an artificial conductive structure at 1000 m depth.

This effect can been seen for different source receiver geometries and could also be reproduced using Occam 1D Magnetotelluric (MT) inversions. For a given dataset one can find a regularisation parameter such that the final model contained arbitrarily large unrealistic oscillations. Similar behaviour of smoothness constraint using l_2-norm has been observed by Rosas Carbajal et al. (2012).

Thus, due to this oscillatory behaviour in addition with the inability to resolve sharp resistivity contrasts smoothness constraint inversion may not be suitable for time-lapse inversion. I therefore tested different alternative regularisation strategies.

6.3.2 Tikhonov

One way of reducing this oscillatory behaviour and not explicitly penalising sharp conductivity contrasts is by using a damped version of the Gauss-Newton approach

$$R(\mathbf{m}_{j+1} - \mathbf{m}_j) = ||\mathbf{m}_{j+1} - \mathbf{m}_j||^2. \tag{6.2}$$

Here j stands for the model at iteration j. As only the difference in conductivity between individual model cells is evaluated, no additional coupling between neighbouring cells is included preventing the inversion from artificial oscillations. It is further aimed to keep model updates in each iteration small. Here $\mathbf{P}$ is simply the identity matrix. As no explicit smoothing is enforced by the regularisation, sharp contrasts of neighbouring cells are not penalised. Therefore, this method is more suitable if one wants to resolve sharp contrasts.

6.3.3 Minimum support

Various other regularisation techniques have been developed some aiming to focus model updates within small confined areas. A popular version of these focusing regularisations was introduced in Portniaguine and Zhdanov (1999) and is referred to as Minimum Support regularisation. The functional is given as follows

$$R(\mathbf{m} - \mathbf{m}_{ref}) = \sum_{j=1}^{N} \frac{\left(m_j - m_{ref,j}\right)^2}{\left(m_j - m_{ref,j}\right)^2 + \epsilon^2}, \tag{6.3}$$

where ϵ is a small number preventing the denominator of becoming zero and controls how fast each summand converges to 1 for increasing differences to the reference model. Thus for differences above some threshold the difference between current model and reference model is not of importance. Instead the number of model cells deviating from the reference model is penalised. Thus Minimum Support regularisation aims to keep deviations from the reference model in as few cells as possible.
As R is a non-linear function of $\mathbf{m}$, the diagonal matrix $\mathbf{P}$ has to be evaluated new within each iteration. Its entries are given by (see Grayver et al., 2013)

$$P_{ii} = \sqrt{\frac{2\epsilon^2}{\left[\left(m_i - m_{ref,i}\right)^2 + \epsilon^2\right]^2}}\,. \tag{6.4}$$

6.3.4 Cauchy

Another regularisation that aims to keep as few number of cells deviating from a given reference model is the Cauchy functional (Sacchi and Ulrych, 1996)

$$R(\mathbf{m} - \mathbf{m}_{ref}) = \sum_{j=1}^{N} \ln\left(1 + \left(\frac{m_j - m_{j,ref}}{\epsilon}\right)^2\right)\,. \tag{6.5}$$

Here I followed the implementation given by Rosas Carbajal et al. (2012) with $\mathbf{P}$ given by

$$P_{ii} = \sqrt{\frac{1}{\left(m_i - m_{ref,i}\right)^2 + \epsilon^2}}\,. \tag{6.6}$$

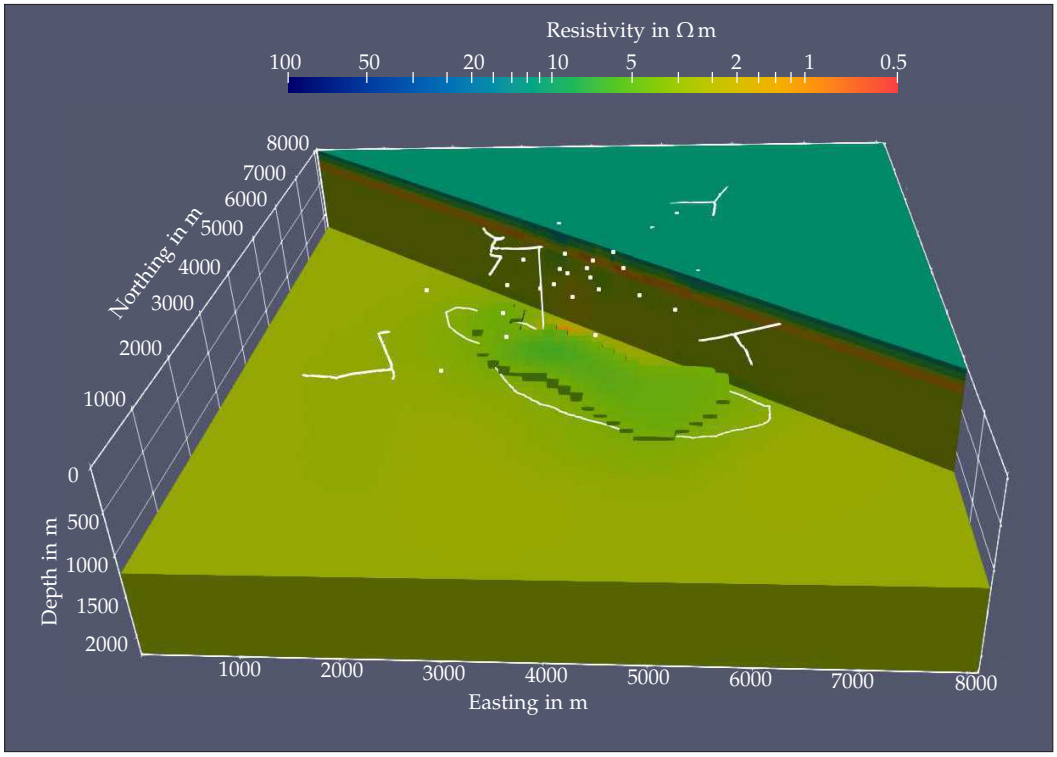

Figure 6.4: 3D inversion result for time-step 1, with Tikhonov regularisation without any additional constraints. The Final nRMS is 1.39 (-53%). Below 700 m all cells with resistivity of 4 Ω m and above are highlighted.

Again ϵ controls the fraction and amplitude of cells deviating from the reference model.

6.4 An unconstrained inversion example

In order to be able to compare inversion results an unconstrained inversion of the first time-step of the reference dataset using Tikhonov regularisation is shown first. Starting model has been the true *canonical layered halfspace* background structure. The Final model after 25 iterations is shown in Fig. 6.4.

The model generally contains only a weak impression of a reservoir with slightly elevated resistivity inside the reservoir of 4-5 Ω m compared to the 3 Ω m background structure.

Initial and final misfit of one TF for all frequencies is shown in Fig. 6.5 and Fig. 6.6 respectively. The initial misfit is identical to the misfit shown in Fig. 4.14. High initial misfits are only found in the E_x-component below 3 Hz. After 25 iterations misfit decreased significantly. Approximately half of the data points are explained within the error bars (cf. 6.6 a, and b) which is also expressed in d) where half of the residuals are within the target value of 1.

Although the misfit decreased significantly by more than 50% the resistive reservoir could not be recovered. It is easy to see that if the inversion struggles to find the

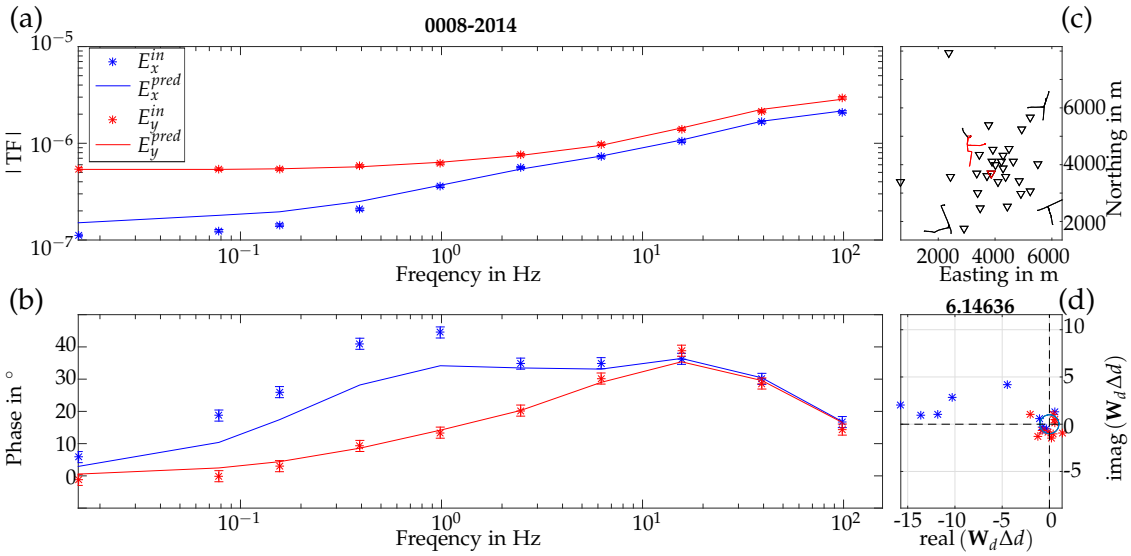

Figure 6.5: Initial misfit of the unconstrained inversion of time-step 1 of the reference dataset. (a) Amplitude and (b) phase of TFs over frequency of input data and model response of a single receiver station. (c) Map view showing source receiver orientation. Active wires and the corresponding receiver are marked in red. (d) Normalised misfit of each individual data point in a) and b) in the complex plain. Colours correspond to the field components in (a) and (b). The total nRMS for all for all shown data points is given above. The blue circle marks the target misfit corresponding to an nRMS of 1.

completely oil filled reservoir of time-step 1 it will be even more difficult to obtain an image of the second time-step where oil saturation has decreased. Thus additional constraints have to be used to increase resolution towards the reservoir.

6.5 Implementation of additional constraints

As shown just before unconstrained 3D inversion often results in poorly resolved images. During monitoring applications one can assume to have good knowledge about the general background structure from exploration and the development of the oil field before and during production. Such knowledge among others can be feed into the inversion as constraints and a-priori knowledge, reducing the ambiguity and thereby allowing for better resolved images. Within this thesis the effects of the following constraints have been investigated.

6.5.1 Starting and reference models

The easiest and most straight forward option is given by the choice of the starting and or reference model of the inversion and is already exploited by the cascaded inversion approach. Especially when a-priori information is known these can be incorporated into the starting model. Most inversions assume the reference model to be equal to the starting model, thus keeping deviations from the starting model as small a possible, however these two models do not necessarily be the same.

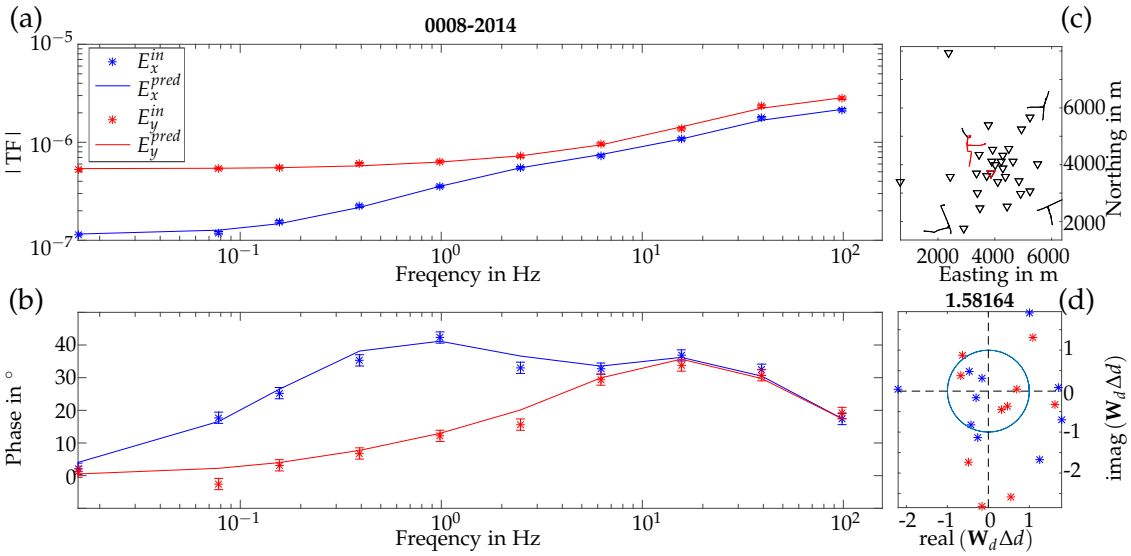

Figure 6.6: Final misfit after 25 iterations of the unconstrained inversion of time-step 1 of the reference dataset. (a) Amplitude and (b) phase of TFs over frequency of input data and model response of a single receiver station. (c) Map view showing source receiver orientation. Active wires and the corresponding receiver are marked in red. (d) Normalised misfit of each individual data point in a) and b) in the complex plain. Colours correspond to the field components in (a) and (b). The total nRMS for all for all shown data points is given above. The blue circle marks the target misfit corresponding to an nRMS of 1.

6.5.2 Model weighting

By applying an additional model weighting scheme following Candansayar (2008) model updates will be preferably allocated within user defined regions. Assuming the forward operator is given by $f(\mathbf{W}_m^{-1}\mathbf{m})$, with the diagonal model weighting matrix $\mathbf{W}_m$, then the normal equations change by using the weighted sensitivity matrix.

$$\hat{\mathbf{J}} = \mathbf{J}\mathbf{W}_m \tag{6.7}$$

Thus model updates are obtained by the modified normal equations given by

$$\left[\Re\{\hat{\mathbf{J}}^H\mathbf{W}_d^T\mathbf{W}_d\hat{\mathbf{J}} + \lambda\mathbf{P}^T\mathbf{P}\right]\mathbf{W}_m^{-1}\Delta\mathbf{m} = \Re\{\hat{\mathbf{J}}^H\mathbf{W}_d^T\mathbf{W}_d\Delta\mathbf{d}\} - \lambda\mathbf{P}^T\mathbf{P}\left(\mathbf{m} - \mathbf{m}_{ref}\right). \tag{6.8}$$

As one usually expects changes between time-steps within certain areas, cells in those regions of expected changes can be allocated with higher weights than cells outside, thus increasing resolution to certain regions.
Whenever it is mentioned that a model weighting scheme is used within this thesis, the scheme shown in Fig. 6.7 was applied. The model weighting was used in a conservative manner. Weights have not been constrained laterally but only vertically. In reservoir depth at 1200 m including 150 m below and above, weights have been set to 1, following one cell layer of 50 m with weights of 0.6. 200 m above and below the reservoir weights have been decreased even further to 0.3. Thus the inversion should aim to allocate updates within a 400 m layer surrounding the reservoir.

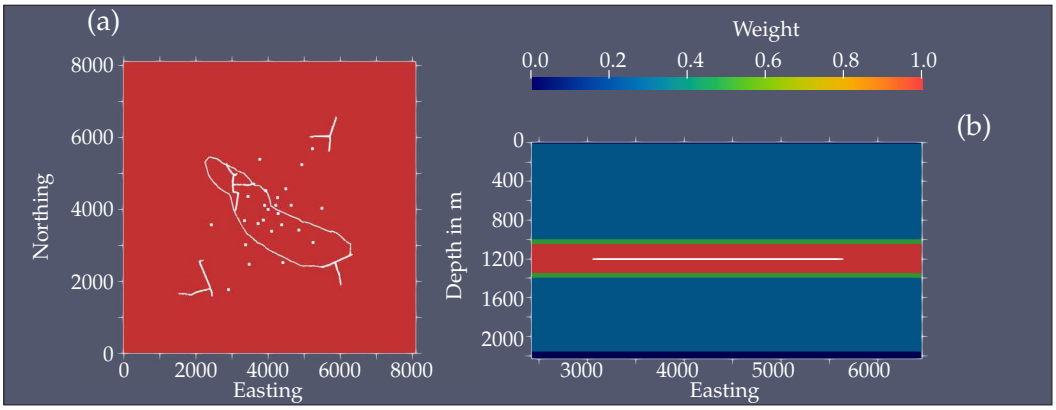

Figure 6.7: Distribution of model weights applied to all inversions within this study. (a) Horizontal slice at reservoir depth. Source receiver configuration is shown by white lines (transmitters) and white dots (receivers). The outline of the reservoir is indicated as white line too. (b) Vertical slice showing distribution of weights with depth. Reservoir position is marked by the thick white horizontal line.

6.5.3 Bounded conductivity transformation

During reservoir monitoring it is usually assumed that resistivity is only decreasing over time as resistive oil gets replaced by conductive brines. This knowledge can be incorporated by guiding the model update into the desired direction. This can be achieved by the use of a parameter transformation. The most common transformation is a simple log-transform where model parameters are assumed to be the natural logarithm of the conductivity thus preventing it of becoming negative.
Choosing a continuous monotonous transformation function $x(m)$ that tends to upper and lower values if m approaches $\pm\infty$ allows to constrain the resistivity within these boundaries. As this function is not restricted to be equal for each model cell one can allow for different upper and lower limits in each cell. Regarding its application to time-lapse inversion one can force model parameters to only decrease (or increase) in a certain time-step by applying upper (or lower) boundaries in all cells close to the starting model of the inversion. The transformation function that has been already implemented by Grayver et al. (2013) was introduced by Kim and Kim (2011) and is given by

$$x_k(m) = \frac{1}{p} \ln\left(\frac{m_k - a_k}{b_k - m_k}\right), \; a_k < m_k < b_k, \tag{6.9}$$

where a_k and b_k are the upper and lower bounds of each model cell. p controls the steepness of the transformation function. An exemplary graph with upper boundary of 2 and lower boundary of 10^{-2} and the steepness control factor p of 2 is shown in Fig. 6.8.

6.6 Time-lapse inversion results

Within the Enhanced Oil Recovery (EOR)-project time-lapse data of three consecutive years have been collected in the Bockstedt oil field. A detailed analysis of the meas-

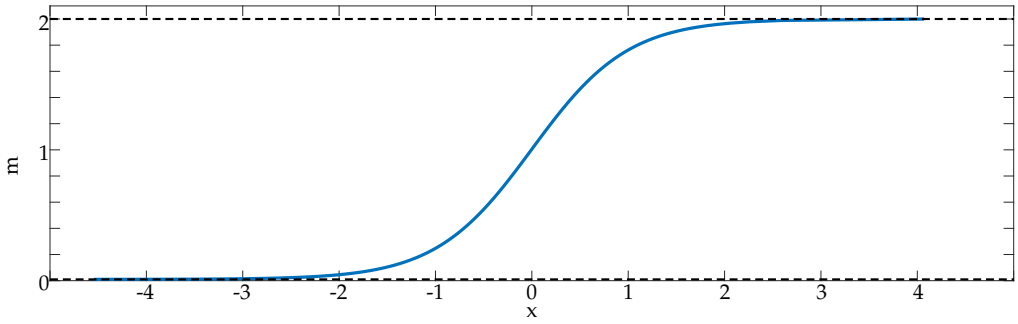

Figure 6.8: Model transformation function with lower and upper bounds of 10^{-2} and 2 and $p = 2$.

ured data (see Tietze et al., 2018b) had shown no significant time-lapse difference between data of consecutive years related to changes in the subsurface. As the produced fluids contains mostly saline brines and only little amount of oil it is believed that changes inside the reservoir are minor and thus not be resolvable by surface based CSEM. Therefore this study focuses on synthetic data only.
All the different regularisations and constraints have been extensively tested using various different combinations. In the following time-lapse inversion results for some selected settings and configurations are shown. In order to keep the number parameters at manageable levels inversions for both time-steps use identical settings. The Finite Difference (FD)-grid is the same in each shown inversion. Horizontal discretisation is 150 m $\times$ 150 m. At surface thickness is 10 m and is increasing with depth. Below a depth of 150 m thickness stays constant at 50 m.

6.6.1 Tikhonov + Modelweighting

At first I am showing results obtained using Tikhonov regularisation in combination with the presented model weighting strategy.
Fig. 6.9 shows the final inversion models of both time-steps of the reference time-lapse dataset. The model obtained for time-step 1 (Fig. 6.9 a) was shown already in section 4.4 to highlight the effect of the galvanically attached steel-cased well. The reservoir is generally imaged at the right lateral position. However the absolute value of the resistivity of the reservoir is mostly underestimated. Only in the central area resistivities are close to the true model of 100 Ω m. Due to the data coverage resolution generally decreases to the edges. Especially the north-western and south-eastern edges could not be resolved. In addition the reservoir is imaged 200 m too shallow.
Following now the cascaded inversion procedure, a) is used as starting model for the second time-step whose final model is shown in b). Clearly the unchanged resistive north-western part of the reservoir is imaged well. Again resistivity is generally underestimated especially in the south-eastern part where in the true model resistivity has decreased between time-steps to 16 Ω m. In the obtained image resistivity does not differ from the 3 Ω m background.
Comparing both time-steps one can clearly identify in which part of the reservoir resistivity has decreased between the time-steps, however one can not estimate the

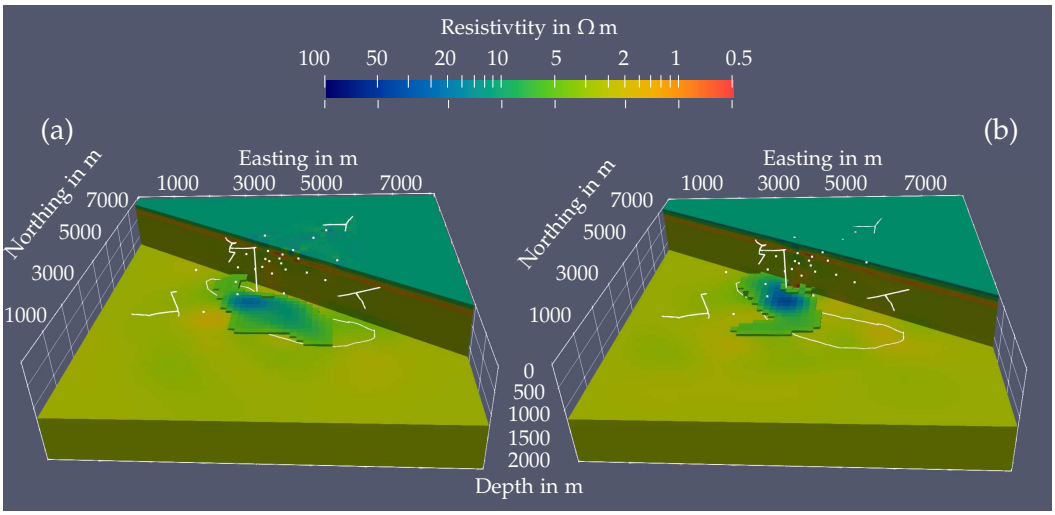

Figure 6.9: Inversion models of the reference dataset for (a) time-step 1 after 25 iterations and (b) time-step 2 after 25 iterations. Below 700 m all cells with resistivity of 5 Ω m or more are highlighted.

correct amplitude of resistivity reduction. In addition the unchanged north-western part that has been poorly resolved in time-step 1 is much better resolved after the second time-step. Thus, if the original model would not be known resistivity seems to have increased in this area. This can be explained by a changing sensitivity pattern once the resistivity is changing. As CSEM is sensitive to horizontal resistive layers, sensitivity focuses to the north-western area as the resistivity in the south-eastern area decreases during the inversion.
Distribution of misfits per receiver station for both models including the initial misfit for time-step 2 are shown in Fig. 6.10, with a) being final misfit of time-step 1, b) initial misfit of time-step 2 and c) the final misfit of time-step 2. The total nRMS for each scenario is given above. In both time-steps it decreased to 1.37 and below, showing approximately similar data fit for both time-steps. Naturally reduction in nRMS is larger for time-step 1 as the initial model for time-step 2 explains the data already to a much higher degree. Careful observation of misfits shown in Fig. 6.10 a) and c) suggests that stations just south-east of transmitter S01 have higher misfits after time-step 1 than after time-step 2. Their lateral position correlates well with the at time-step 1 poorly resolved north-western part of the of the reservoir, which is much better resolved in time-step 2.

6.6.2 Tikhonov + Model Weighting + Conductivity Boundaries

As shown before one can use bounded model parameter transformation to guide model updates towards a certain direction. Thus this idea has been tested by guiding model updates for the second time-step towards higher conductivities. As before I used the final model of time-step 1 (see Fig. 6.9 a) as starting and reference model for the inversion of the second dataset. In addition lower boundaries in conductivity have been applied. Boundaries are set for each cell individually. While the maximum value of the conductivity was kept the same for all cells at 100 S m^{-1}, lower boundaries have

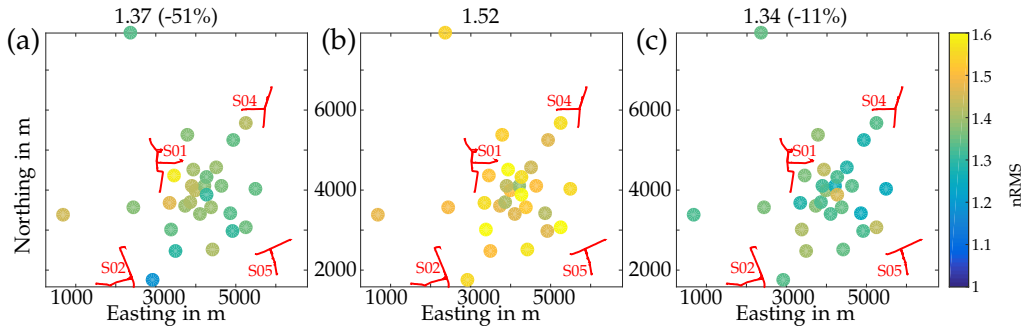

Figure 6.10: Distribution of misfits per receiver station for the time-lapse inversion models shown in Fig. 6.9. Distribution is shown as map view where all data points of one receiver are combined into a single nRMS and subsequently colour coded. (a) Final misfit distribution for time-step 1 after 25 iterations. (b) Initial distribution of misfits for time-step 2. (c) Final misfit for time-step 2 after 25 iterations. The total nRMS including their reduction from the initial value for each scenario is given above.

been set to 90 % the value of the starting model.
Fig. 6.11 shows an intermediate model of time-step 2 after 6 iterations in a) and the final model after 25 iterations in b). At the intermediate state of the inversion one can clearly see that resistivity decreased in the south-eastern part of the reservoir, while it remains unchanged in the north-western half, which fits well to the true model. However, once inversion continues, strong small scale conductive artefacts appear which can be seen in the final inversion model (Fig. 6.11 b). As shown in the previous time-lapse inversion without constraints on conductivity (Fig. 6.9), the north-western part of the reservoir is poorly resolved in time-step 1 and due to changing sensitivity pattern better resolved in time-step 2. Thus, resistivity had to increase in that area between time-steps. As increasing resistivity has been prohibited in this scenario, inversion had to place artificial conductors in other areas to counter this effect.

Again misfit distribution per receiver station is shown for both models in Fig. 6.12. Visual inspection of the nRMS distribution for the intermediate model (Fig. 6.12 a) shows no significant regional clustering of high nRMS. Residuals for the final model (Fig. 6.12 b) are generally lower. Although misfits reduce to similar levels as in the inversion without bounded conductivity the model shows severe artefacts unrelated to the true conductivity distribution. The aim of this study is to highlight that usage of the bounded conductivity transformation as constraints is a viable tool to increase resolution capabilities and reduce the uncertainty in model space, however they must be used with care. At this point one should mention that varying conductivity bounds may result in unexpected consequences due to its interaction with the regularisation. Regularisation is directly applied to the parameters in the transformed model space. Thus transformation of each model parameter is dependent on the chosen boundaries in that particular cell may lead to unforeseeable consequences. This especially prohibits the use of a smoothness constraints regularisation or any other regularisation that evaluates differences between neighbouring cells.

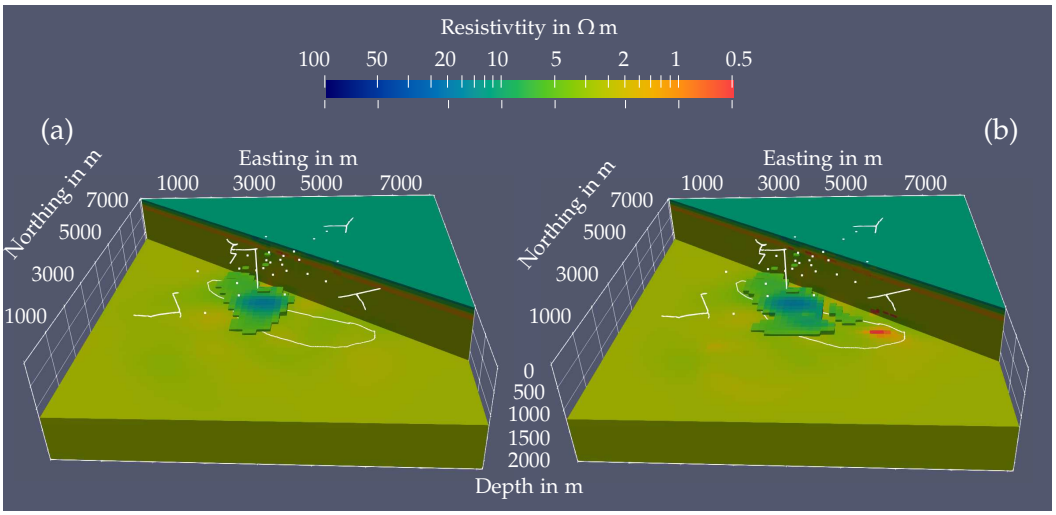

Figure 6.11: Inversion models of the reference dataset for (a) time-step 2 after 6 iterations with a total nRMS of 1.40 (-7%) and (b) time-step 2 after 25 iterations with a total nRMS of 1.35 (-11%). Below 700 m all cells with resistivity of 5 Ω m or more are highlighted.

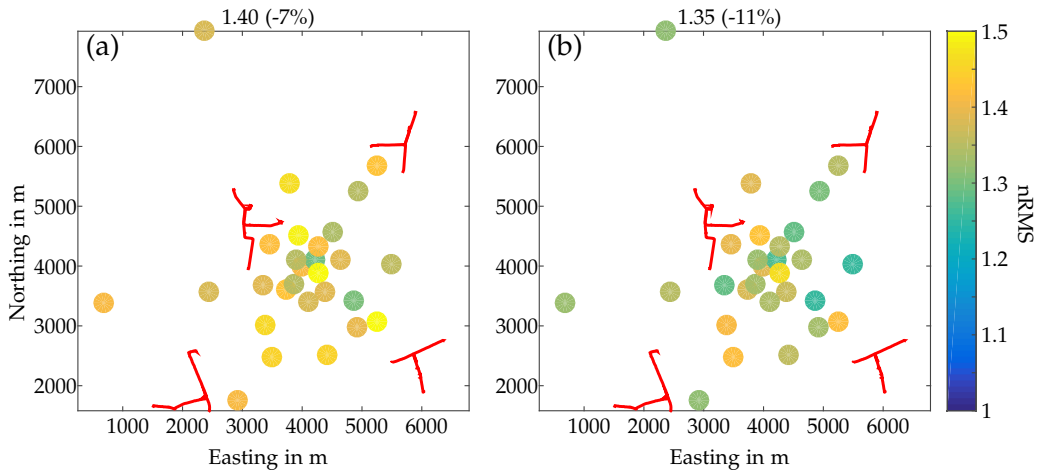

Figure 6.12: Distribution of misfits per receiver station for the iterations shown in Fig. 6.11. Distribution is shown as map view where all data points of one receiver are combined into a single nRMS and subsequently colour coded. (a) Misfits after 6 iterations and (b) final misfits after 25 iterations. Total nRMS including reduction from starting nRMS is given above for both iterations.

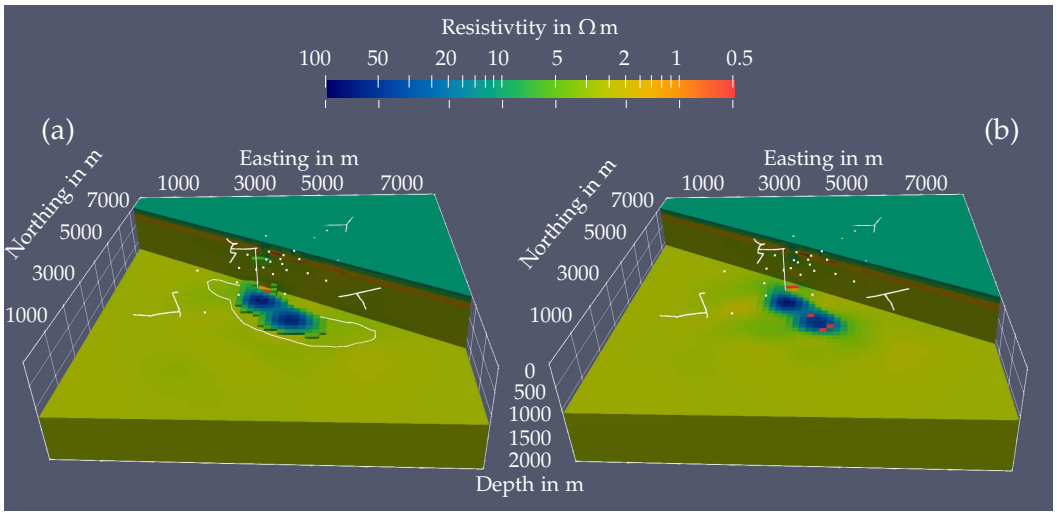

Figure 6.13: Inversion models of the reference dataset using Minimum support regularisation and model weighting scheme. (a) Model for time-step 1 after 25 iterations and (b) time-step 2 after 25 iterations. Below 700 m all cells with resistivity of 5 Ω m and above are highlighted.

6.6.3 Minimum Support + Model weighting

Here results obtained for a Minimum Support regularisation together with the model weighting strategy are discussed. As before settings between time-steps have not been changed to reduce the number of degrees of freedom the user has to provide for the time-lapse inversion. The final model for both time-steps is shown in Fig. 6.13.
The imaged reservoir after time-step 1 (Fig. 6.13 a) is again mapped laterally at the right location but vertical 200 m to shallow. As it is typical for Minimum Support regularisation its outline is well defined by sharp boundaries to the surrounding background structure. Absolute values of the resistivity inside the reservoir are higher than in the Tikhonov regularisation example but still underestimated ranging mainly between 10 and 50 Ω m. The north-western as well as the south-eastern edge are not resolved similarly to the inversion results shown before.

The second time-step shown in Fig. 6.13 b) shows much greater differences to the Tikhonov inversion example. Instead of changing the resistivity in the entire half of the reservoir, updates are focused within three cells with extremely low resistivities of 0.5 Ω m and below. In fact during the first inversion iterations updates are spread out over larger volumes, while updates are revoked again in large parts of the model the longer the inversion is running. This effect has also been seen in the Cauchy regularisation and is discussed in more detail in the following section.
Again misfit distributions of the final model of time-step 1 and 2 including the starting misfit for time-step 2 are shown in Fig. 6.14. Misfits between the Minimum Support (Fig. 6.14)and the Tikhonv inversion (Fig. 6.10) do not differ significantly. Global nRMS differ by less than 0.02. Largest differences in global as well as local nRMS between the two is found for the final model of time-step 2 (see 6.14 c). Together with the unrealistically focused inversion result this indicates a superior inversion result for the Tikhonv regularisation example.

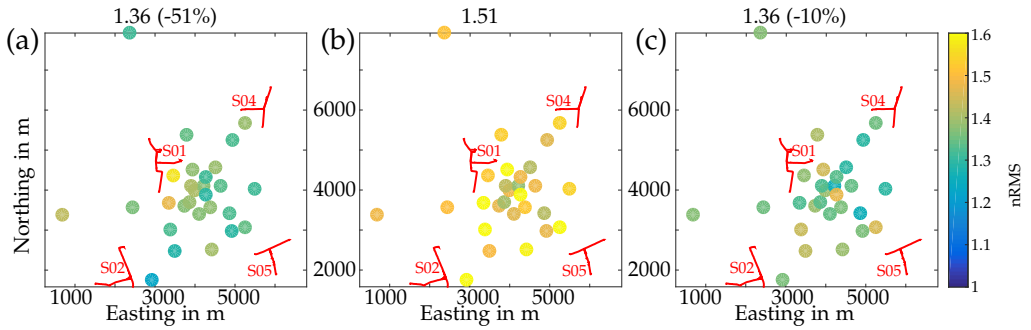

Figure 6.14: Distribution of misfits per receiver station for the Minimum Support time-lapse inversion models shown in Fig. 6.13. Distribution is shown as map view where all data points of one receiver are combined into a single nRMS and subsequently colour coded. (a) Final misfit for time-step 1 after 25 iterations. (b) Initial misfit for time-step 2. (c) Final misfit for time-step 2 after 25 iterations. The total nRMS including the reduction from the initial misfit is given above each plot.

6.6.4 Cauchy + Model weighting

The second focusing regularisation that has been tested is the Cauchy regularisation. Horizontal slices at 1060 m depth for different inversion iterations are shown in Fig. 6.15. The final model of time-step 1 is shown in Fig. 6.15 a), while the final model of time-step 2 is shown in Fig. 6.15 c). Fig. 6.15 b) shows an intermediate model of time-step 2 after 12 iterations.

Results are in general similar to the Minimum Support inversion result. The reservoir is imaged laterally at the right position after time-step 1, but vertical again 200 m too shallow (the reservoir is at 1200 m depth while the shown slice is at 1060 m). The north-western and the south-eastern edges are again not resolved. Resistivity in the central area is higher than in the Tikhonov example ranging between 10 Ω m and 50 Ω m. The nature of the focusing regularisation techniques becomes again eminent in the final inversion model of time-step 2 (Fig. 6.15 c). Mainly all changes in resistivity structure inside the reservoir are focused to two cells with extreme values below 1 Ω m. This effect is not visible in the intermediate model of the inversion of time-step 2 shown in Fig. 6.15 b). As given by the true model of time-step 2 (cf. Fig. 6.1 b) the eastern half of the reservoir changed resistivity towards higher conductivity. The focusing effect only starts to come into play after the 12th iteration of the inversion.
The reduction of global nRMS during the inversion of the second time-step with iterations is shown in Fig.6.16. The rate of misfit reduction decreases with the number of iterations. During the first iteration misfit reduces by 0.08 or -5% while the reduction is less than 0.0006 (-0.05%) during the last iteration. Misfit distribution per receiver station generally does not differ from the Minimum Support regularisation example shown in Fig. 6.14.

6.6.5 Tikhonov + Modelweighting + Ez

As discussed in section 5.3 vertical electric field receivers may particularly be useful for monitoring studies as they have a more focused sensitivity distribution, allowing

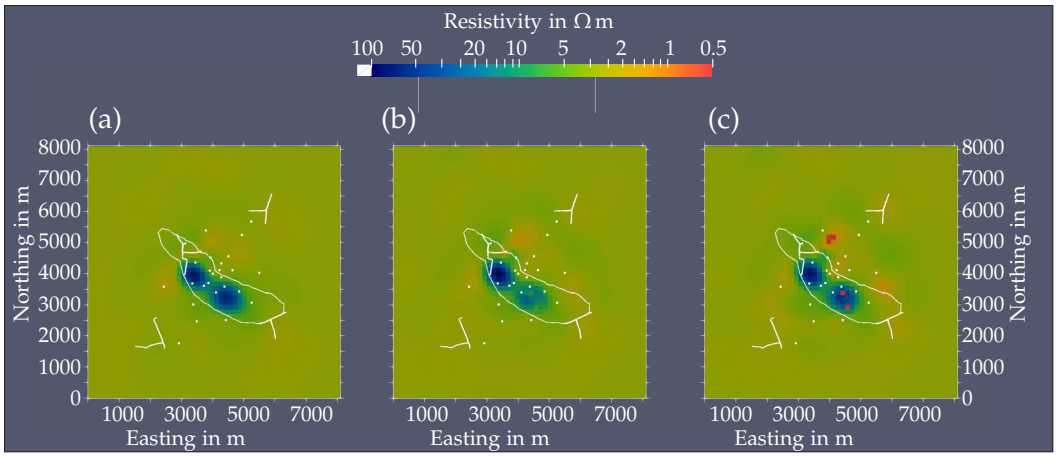

Figure 6.15: Map view of horizontal slice at 1060 m depth for time-lapse inversion result using Cauchy regularisation for (a) the final model of time-step 1, (b) intermediate model of the inversion of time-step 2 after 12 iterations and (c) the final model of time-step 2 after 25 iterations.

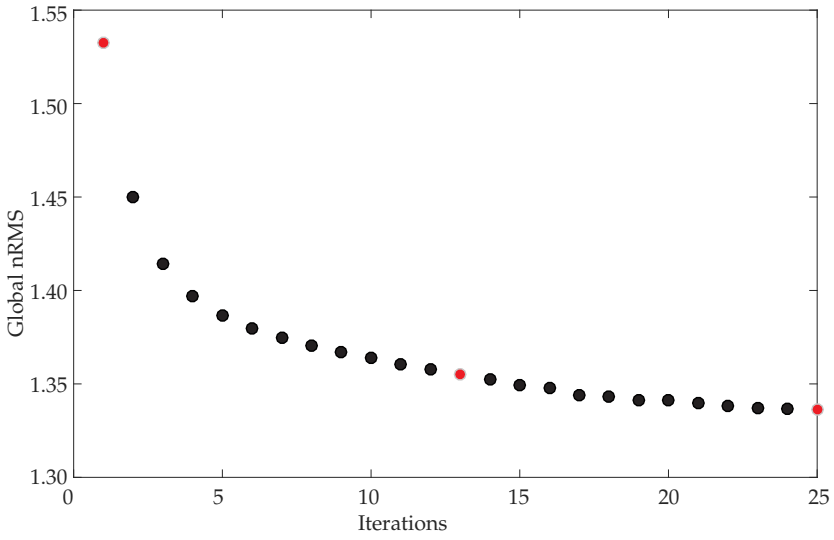

Figure 6.16: Development of nRMS over the iterations for the inversion of time-step 2 using Cauchy regularisation. Iterations whose models are shown in Fig. 6.15 are marked in red.

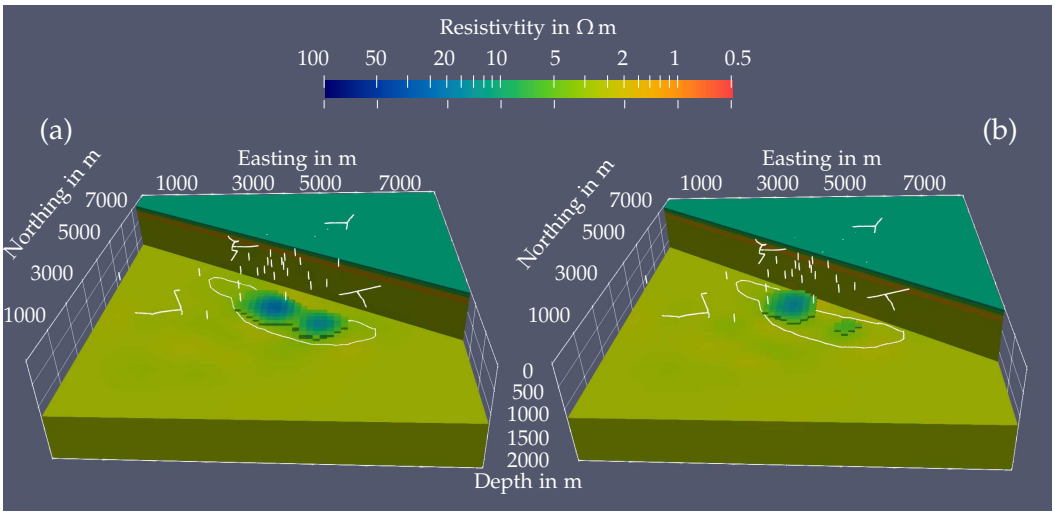

Figure 6.17: Time-lapse inversion models of modified reference dataset. All classical surface based receivers have been exchanged by 200 m long vertical elongated receivers as described in section 5.3. Steel-cased wells have not been taken into account. (a) time-step 1 after 25 iterations and (b) time-step 2 after 25 iterations. Below 700 m all cells with resistivity of 5 Ω m and above are highlighted.

for better lateral resolution. Thus I obtained time-lapse inversion results using vertical electric field receivers only. The true model is identical to the true model of the time-lapse reference dataset. In contrast to the reference dataset all horizontal electric field receivers are exchanged by 200 m long elongated vertical electric field receivers. Each receiver spans from surface to depth. However receivers are not oriented perfectly vertical. Instead each receiver is tilted by a random angle between 0 and 1° out of the vertical axis in also random azimuth. This setup has already been used to show the correctness of the implementation of elongated receivers in the CSEM inversion and the beneficial resolution characteristics in 3D inversion. No steel-cased wells are added into this example. Synthetic data for six frequencies between 0.0156 Hz have been 2.4764 Hz generated.

Again Tikhonov regularisation and the same model weighting strategy as before have been used. The final model of time-step 1 shown in Fig. 6.17 a) has been already discussed in section 5.3. As the inversions shown before, lateral position of the reservoir could be recovered well. Especially the north-eastern edge is well resolved. Again due to poor data coverage the north-western part is not recovered. As in the examples shown before, resistivity is mostly underestimated. A comparison with the final model of time-step 2 (Fig. 6.17 b) clearly shows the reduction in resistivity in the eastern half of the reservoir. Distributions of misfits by receiver site is shown again as map views for the final model of time-step 1 (Fig. 6.18 a), the initial misfit of time-step 2 (Fig. 6.18 b) and the final misfit of time-step 2 (Fig. 6.18 c). Misfits are genrally higher than for horizontal receivers. Most receiver sites show a final misfit between 1.4 and 1.5 after time-step 1. Misfits are spread over all receiver sites with no significant clusters of high nRMS values. Initial misfits for time-step 2 increase to values of approximately 1.9. Final misfits after the second time-step decrease to lower

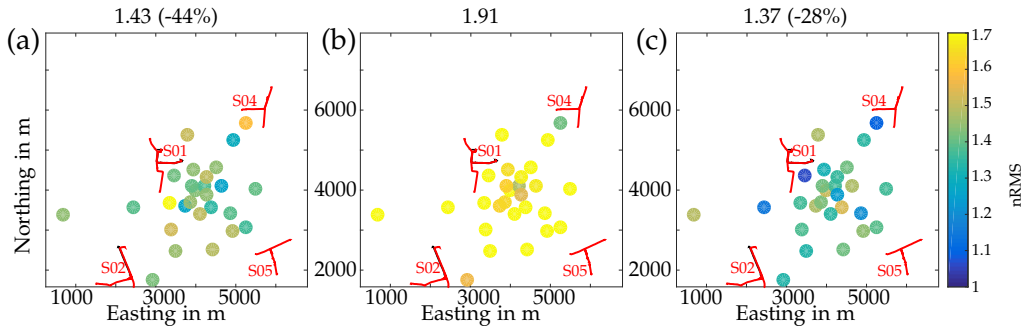

Figure 6.18: Distribution of misfits for the time-lapse inversion models shown in Fig. 6.17 for receiver station. Distribution is shown as map view where all data points of one receiver are combined into a single nRMS and subsequently colour coded. (a) Final misfit for time-step 1 after 25 iterations. (b) Initial misfit for time-step 2. (c) Final misfit for time-step 2 after 25 iterations. Total nRMS including the reduction from the initial value is given above each plot.

values than after time-step 1 with values between 1.3 and 1.4. The reduction in the nRMS in the second inversion is higher than for all shown horizontal field data inversions (-28% instead of -11%). This is another indication of the increased sensitivity of vertical electric field receivers.

6.6.6 Choice of the starting Model

Finally I am showing how the choice of the starting model can be used to help focus inversion updates towards the reservoir by adding additional Information. As shown and discussed before all previously shown inversion models imaged the reservoir laterally at the right position, but vertically they were all imaged approximately 200 m to shallow. This coincides perfectly with the top of the increased model weighting, indicating rather limited depth resolution.
In many cases the true depth of the reservoir is known due to exploration and well logging. Such constraints can be added into the starting model to pinpoint the reservoir at the right depth. Thus, I included this constraint in a conservative manner by adding a 5 Ω m layer at reservoir level to the starting model used for the inversion of time-step 1, but keeping the reference model equal to the true background structure (the starting model of the previous inversion results). The modified starting model is shown in Fig 6.19 a). Note that the vertical grid dimension at reservoir level is 50 m thus being significantly larger than the true reservoir thickness of 15 metre. The 5 Ω m layer consists of two 2 layers of cells thus being 100 m thick. The layer structure of the starting model is shown as blue line in Fig. 6.19 b). The resistivity distribution with depth through the imaged reservoir is shown as yellow line for the Minimum Support inversion from section 6.6.3.
To test this approach I inverted the reference dataset using the same settings as before in the Minimum Support regularisation example. Fig. 6.19 b) shows the distribution of resistivity with depth for the starting model (blue line), the final model after time-step 1 (red line) and the less constrained model shown in Fig. 6.13 a). Clearly by providing the additional constraint the imaged reservoir appears at the right depth.

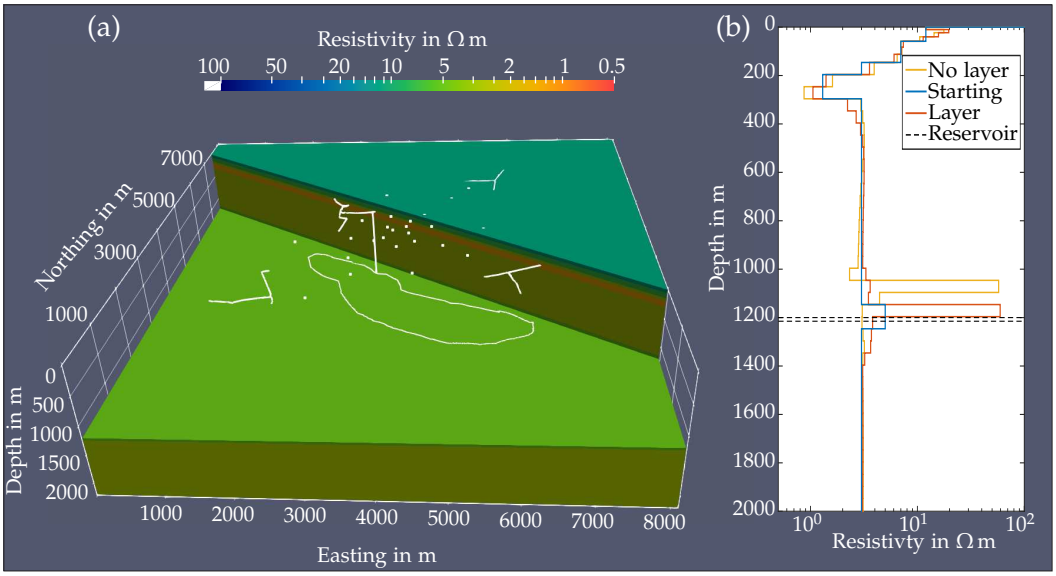

Figure 6.19: (a) Starting model used for the inversion of time-step 1. Only the starting model contains the additional 5 Ω m layer at reservoir depth. Reference model is kept the same as before without the additional resistive layer. (b) Resistivity distribution with depth at Northing = 3750 m and Easting = 4000 m for the model shown in Fig. 6.13 a) (yellow), the starting model including 5 Ω m layer at reservoir depth shown in (a) (blue) and the final inversion model with the resistive layer in the starting model shown in Fig. 6.20 a) (red).

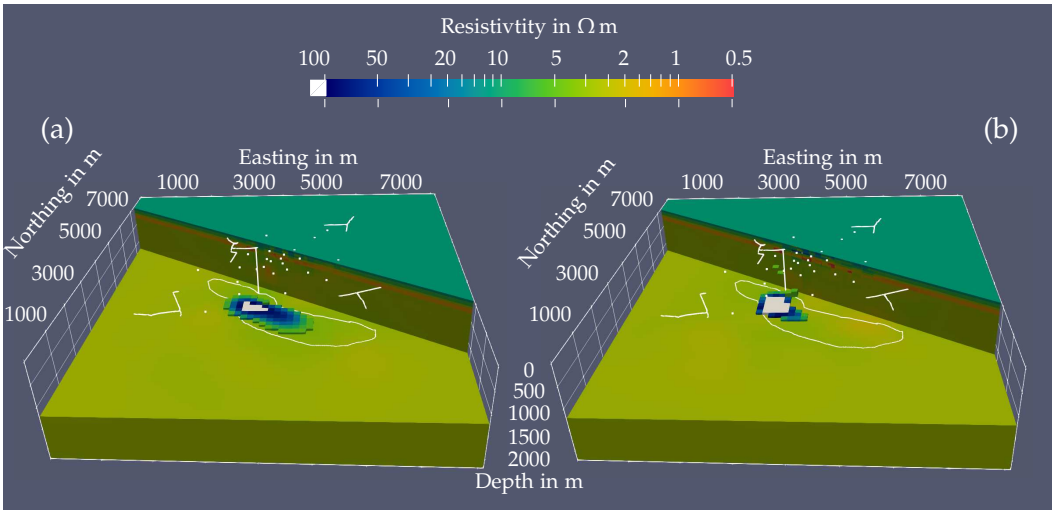

Figure 6.20: Inversion models of the reference dataset using Minimum support regularisation with $\epsilon = 0.6$ and model weighting scheme including the 5 Ω m layer at reservoir depth in the starting model of time-step 1 shown in Fig. 6.19. (a) Model for time-step 1 after 25 iterations and (b) time-step 2 after 25 iterations. Below 700 m all cells with resistivity of more than 5 Ω m are highlighted. Cells with resistivity above 100 Ω m are marked white.

Fig. 6.20 a) shows the obtained final model after 25 iterations. The lateral resolution is similar to the inversion results shown before. Except now resistivity just south of the added steel-cased well are slightly over estimated (≈ 150 instead of $100\,\Omega\,\mathrm{m}$, indicated by the white cells). All cells outside the reservoir where there is no sensitivity returned to $3\,\Omega\,\mathrm{m}$ background and reference model.
Once the reservoir is imaged at the right depth it stays at the right depth even in the inversion of the second time-step (Fig. 6.20 b). Similar effects shown and discussed in the Tikhonov inversion example (see Fig. 6.9) are also present here. Resistivity clearly decreased in the eastern half of reservoir. However, resistivity increased in the western half of the reservoir, where the true model did not change between time-steps. As expected by the minimum support regularisation changes appear to be more focused in smaller volumes.
CSEM is generally sensitive to horizontal resistive structures. Thus by adding a resistive layer to the starting model, sensitivity is increased inside that layer during the first iteration. This increased sensitivity results in larger updates inside this layer obtaining even higher resistivity. Thus creating a positive feedback loop, attracting even more updates inside the resistive structure. Therefore by providing only slightly elevated resistivity at the expected depth of the reservoir in the starting model, one can guide the inversion to the exact depth.
Misfits are summarised in Fig. 6.21. Similar to the inversion results shown before, misfits decrease to approximately 1.33 for both time steps. Thus indicating similar data fits. Naturally reduction in data fit is higher for the inversion of time-step 1 as the starting model explains data to a lower degree. Comparing the data fit per receiver station (Fig. 6.21 a vs. c) shows a better data fit (more blue/greenish colours) for the inversion of time-step 2 than the result for time-step 1, especially for the north-western half of the receiver stations. This correlates well with the poor resolved north-western half of the reservoir after time-step 1. Thus this shows that the presence of the resistive north-western part of the reservoir is detectable using the given source-receicer layout. However a lack of resolution prevents it from being imaged correctly.
This example illustrates the importance of choosing the right starting model not only to provide the exact depth information. Moreover it also highlights an important difference between detectability towards a certain structure and the sensitivity towards it in non-linear inversion problems. Detectability only infers that the presence or absence of a specific structure influences the model response. While sensitivity implies influence of certain regions on the inversion for a given resistivity distribution. Detectability can be seen as a necessary condition to image any structure, however it does not automatically imply sensitivity to the same structure during the inversion. The appropriate choice of a starting model is therefore crucial if one wants to resolve small scale structures or changes in resistivity structure over time.

6.7 Discussion and Conclusion

In order to be able to resolve subtle changes in the resistivity structure of a reservoir, several different time-lapse inversion strategies have been investigated. Within the

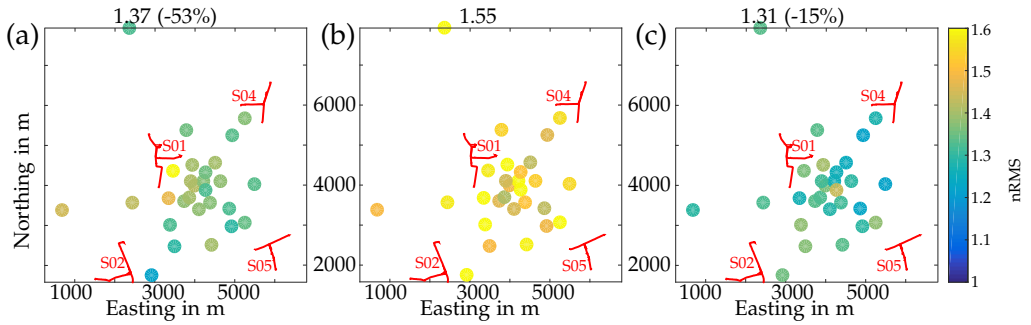

Figure 6.21: Distribution of misfits for the time-lapse inversion models shown in Fig. 6.20 for receiver station. Distribution is shown as map view where all data points of one receiver are combined into a single nRMS and subsequently colour coded. (a) Final misfit for time-step 1 after 25 iterations. (b) Initial misfit for time-step 2. (c) Final misfit for time-step 2 after 25 iterations. The total nRMS including the reduction from the initial misfit for each scenario is given above.

framework of this thesis I applied a cascaded inversion approach to synthetic time-lapse datasets. This method combines the flexibility of a changing source-receiver layout between time-steps together with manageable computational demands as well as temporal coherency. There the final model of the previous time-step is used as reference and/or starting model for the inversion of the current time-lapse dataset.
The datasets used in this study are based on source-receiver layouts from the CSEM field surveys across the Bockstedt oil field. A layered background model representative for the study area has been used together with the real outline of the 15 m thick oil field in 1200 m depth. For simplicity only two reservoir states have been considered. First the reservoir was assumed to be completely oil filled and thus resistive (100 Ω m). In a second stage half of the reservoir is assumed to be partly produced and thus resistivity decreased to 16 Ω m.
Many different inversion parameters and settings have been tested. There two distinct challenges/questions emerged, namely: (1) Are we able to resolve such a thin resistive fully oil-filled reservoir and if so how? (2) Once we are able to resolve the reservoir, how can we detect and localise the changes between the time-steps? As any time-lapse inversion is heavily dependent on the starting/baseline model, question (1) is mainly related to obtaining the right baseline model, while the latter is more related towards the actual time-lapse problem.
As both tasks face similar issues especially regarding resolution capabilities and in addition non-uniqueness of the inverse problem I aimed to face them using similar techniques. The presented results show that in general I was able to locate the resistive reservoir in general. And I was also able to laterally constrain changes between the two time-steps using the cascaded inversion approach. However, it required additional constraints as unconstrained inversion allows for to much ambiguity in the obtained images. First most EM inversion algorithms aim to find smooth models without continuous transition between resistivity contrasts. Thus instead of obtaining well defined and localised resistivity structures images tend to be softened and less well defined. In addition some artificial oscillatory behaviour has been observed. Alternative regularisation methods should be used that do not suffer from these short-

comings and which allow models to be more "blocky". Most of my work focused on three different regularisations, a simple Tikhonov and Minimum Support regularisation and a Cauchy regularisation.
Furthermore additional constraints have been tested. Due to previous exploration one can assume to have good knowledge of the regional resistivity background structure. Thus I used the true layered background as starting model for all inversions. Furthermore one usually has some knowledge about the depth and the lateral extents of the reservoir. Thus updates during the inversion are expected to be confined in certain areas. By adding a model weighting scheme one can guide the inversion to allocate updates mainly in certain regions. Application of the model weighting in a conservative manner (constrain updates only vertical within 400 m) resulted in a well resolved reservoir.
Although the reservoir was laterally imaged at the right position the depth was controlled by the top of the area with increased model weights in all inversions considered, indicating limiting depth resolution. CSEM is generally sensitive to resistors, thus when running different inversions I observed a positive feedback loop where in each iteration updates are predominantly allocated within regions of higher resistivities, increasing sensitivity even further. As the depth of the reservoir is usually well known from borehole logs this effect can be exploited by providing slightly elevated resistivities at reservoir level in the starting model while keeping the reference model unchanged. This effect can also be observed for conductive layers in magnetotelluric prospecting. Both of these constraints have been shown to be a viable tool for both questions of interests.
At this point one has to point out that in the presented synthetic scenarios I simply adopted the source-receiver layout from the CSEM field surveys. This layout was optimised to monitor fluid saturation in the central part of the reservoir. However in the true model one entire half the oil field changed resistivity between time-steps. Thus the edges of the reservoir in strike direction are generally not or only poorly resolved. It is likely that a more optimised survey layout can yield even better results. Despite these promising results there are still many aspects that can be potentially improved in the future, e.g. while locating the change in reservoir resistivity worked well, obtaining the right amplitudes remains challenging. In order to limit the number of inversions required for testing I choose to keep inversion settings between the time-steps fixed. However it might be beneficial to choose different settings between the time-steps. As it has been demonstrated using the focusing regularisation techniques. Results can be even further improved by using more than a single steel-cased well as galvanically coupled source extension. In addition one should consider a combination of vertical receivers and horizontal receivers together with steel-cased wells.

Possible future work
One major drawback especially when many time-steps are used is the rather long computation time. Most inversions results shown here took approximately 3-4 days computing time parallelised across 64 Intel Xenon E5 processors with 2.3 GHz. Some future work should therefore concern possible optimisation strategies. One promising strategy may be given by Jaysaval et al. (2014). Most inversions and in particular time-lapse inversion do not compute updates in the entire model domain (e.g. air layers).

Instead only for a small subset of model cells updates will be computed. Thus in each forward computation conductivity differs from the starting model only a potentially small subset of cells. The proposed usage of Schur Complements would make use of that fact as the expensive factorisation of matrix **A** in eq. 2.6 only has to be performed on a small subset during each forward computation thus reducing computation time as well as memory.
In addition to numerical improvements in computation time and memory consumption one should also implement additional constraints. An alternative conductivity boundary transform to the one that has been presented may be one option. Key (2016) proposed to use a bandpass transform which may help to avoid the unwanted interferences with the regularisation. However, both transforms face the problem that they are symmetric around the mean of lower and upper boundary value. Especially when lower and upper boundary differ by several orders of magnitude it may be advantageous to consider a modified bandpass transform which is symmetric to the geometric mean of lower and upper boundary.
Finally one may implement alternative regularisation methods. Rosas Carbajal et al. (2012) had found that $l1$-norm instead of the usually used $l2$-norm obtained well defined images with sharp boundaries.

Chapter 7

Summary

This thesis has been part of a larger research project aiming to use CSEM for reservoir monitoring (see section 3 for a description of the project). The main aim of this work has been the development of the time-lapse inversion which is essential to image fluid saturation changes in the subsurface. Naturally the work has been influenced by the results of the superordinated research project obtained before and during the start of this PhD work. Thus three main topics have been emerged during the development of this thesis.

Steel Casings are inevitable present in any hydrocarbon monitoring scenario. As steel is up to six orders of magnitude more conductive than the surrounding rock, their pure presence within the study area influences the measured data. Due to their spatially unfavourable dimensions (thin but extended in vertical direction) taking these effects into account is a non-trivial task. In the framework of this thesis I implemented the possibility to consider first order effects of steel-cased wells in the existing modelling and inversion programme.
The approach is able to consider the mutual interaction between wells and does not state any assumptions on the used transmitter. Thus it is capable of considering not only passive (coupled by pure induction) boreholes but also active (galvanic coupling/energised) boreholes. This has been crucial as within the larger researcher project data have been collected where the casing of a wellbore was used for current injection. Without the possibility to describe such sources within the inversion, interpretation of these data would not be possible.
In addition it has been shown that the pure presence of boreholes can be considered advantageous even if they are not directly connected to the transmitter. In general they act as current channels, thus moving energy into greater depth, increasing resolution capabilities at reservoir level. Furthermore, it is well known that responses obtained from vertical electric dipole sources are most sensitive towards thin resistive structures such as hydrocarbon reservoirs. As these steel casings act as additional vertical electric dipole sources, they increase resolution capabilities necessary for reservoir monitoring.
The most crucial parameter for determining their influence is the induced current strength along the casing trajectory. Thus most beneficial effects are obtained if the casing is galvanically attached to the transmitter. However if not possible due to

safety or logistical limitations currents are still significant if current is injected in the vicinity of the borehole (10-20 m). Thus their presence can be exploited cheaply by simply setting up the transmitter nearby a wellbore.
Although not the focus of this thesis inversion of field data considereing the effect of steel-cased wells had shown to be successful in terms of reduction of supposed artefacts as well as data misfit.

Elongated vertical receivers allow for consideration of the physical receiver dimensions when measuring electric fields over long dipoles. Most modern inversion algorithms neglect the dimensions of electric field receivers and assume that they have been measured at a single point. For classical surface based receivers this assumptions is usually valid, as the spatial variation of the electric field is rather small and the receiver lengths required is comparably short («100 m). However vertical electric fields measured in shallow observation boreholes require much longer dipoles and thus violate the assumptions made for point dipole receivers. As mentioned before vertical electric dipoles are known to be the most sensitive towards thin resitive structures such as hydrocarbon reservoirs. Thus one part of the larger research project has been the development of a vertical electric field receiver. In order to be able to consider these data in any inversion I had to develop a new methodology to be able to describe electric fields measured over finite dipoles.
The implemented approach is not limited to vertical electric receivers but is able to work with arbitrarily oriented and shaped receivers. The general methodology can be easily transported to other modelling and inversion codes as it is independent from the numerical method used to solve Maxwell's equations. The additional numerical overhead is rather limited as it requires mainly one additional product of sparse matrices. It is furthermore not limited to CSEM modelling but can be used for other EM methods like magnetotellurics too.
I showed that it is essential to consider the true receiver geometry for shallow vertical electric field receivers. In general vertical electric fields are two or more orders of magnitude smaller than horizontal electric fields. First of all this requires longer measurement dipoles for vertical field measurements ($\approx$ 150 m) to increase the signal to noise ratio above the local as well as system noise floor. Thus the receiver is larger than the typical grid dimensions of the underlying modelling grid (typically 5 m at surface and 50 m at greater depth). Second even minuscule deviations of the receiver from vertical results in significant projection of horizontal electric field components into the desired vertical components. I showed based on field data that deviations of only 0.1° may result in distorted responses by more than one order of magnitude if not considered. The distortion is strongest for high frequencies and shallow dipoles as well as broadside source-receiver configurations. Deep dipoles in inline direction and low frequencies are least affected.
A sensitivity study had shown that the distribution of sensitivity during the inversion differs significantly between horizontal and vertical electric field receivers. For horizontal receivers sensitivity is generally spread out over large areas with maximum values just below the transmitter and the receiver. The amplitude for both maxima is about the same. Vertical receivers however allow sensitivity to focus to much smaller volumes. Highest amplitudes are found just below the receiver resulting in a spot-

light-like sensitivity distribution. Thus vertical receivers are expected to give superior results when high lateral resolution in small areas is required, making them a promising tool for monitoring applications.
Finally I showed that taking receiver dimensions into account in magnetotelluric modelling can help to mitigate some effects of galvanic distortion. An effect likely to be present also in CSEM, although it gained only little attention in the literature so far.

Time-lapse inversion is the process of obtaining a series of subsurface models each representing a snapshot in time. Comparison of these snapshots allows for tracking of changes in fluid saturation over time. Within this thesis I used a cascaded inversion scheme where the inversion result of the previous time-step is used as reference and/or starting model for the inversion of the current time-step. This method has been used as it allows for changing source-receiver setups and steel-casing infrastructure. The computational demands are kept at manageable levels and the temporal coherency is enforced intrinsically.
The cascaded inversion has been tested on synthetic data using the source receiver layout of the surveys across the Bockstedt oil field and conceptual conductivity models representative for the study area.
For the particular scenario of the Bockstedt oil field —15 m thick reservoir in 1200 m depth in a highly conductive approximately 3 Ω m halfspace — one is operating close to the resolution limit of surface based CSEM. This results in two distinct challenges, which I aimed to solve using similar techniques. 1) Are we generally able to resolve such a deep and thin reservoir prior to any production? 2) Can one use the same techniques to image changes within the reservoir between time-steps?
Most of the work has been focussing on non-smoothness constraint regularisations. In monitoring applications one is usually expecting changes in resistivity distribution between time-steps to be confined within small and well localised areas. As smoothness constraint inversion is inherently unable to resolve sharp resistivity contrasts it is not suitable to be used for time-lapse inversion. In addition we have found that it may lead to a spurious layering structure oscillating between high and low resistivities even for synthetic data.
Three different alternative regularisation techniques have been tested, namely a Tikhonov, Minimum support and Cauchy regularisation. The latter two fall within a class called focusing regularisation, as they aim to keep deviations from a given reference model in small volumes.
However even for solving the first posed challenge, the use of additional constraints was required. For this two additional constraints have been tested. First a more sophisticated starting and reference model should be used, as one can assume to have good knowledge of the background structure from previous exploration. In addition one can also assume to have good knowledge of approximate lateral as well as horizontal position of the reservoir. Thus one can apply a model weighting scheme, with increased weights in the reservoir regions where changes are expected to occur.
The usage of the true background structure as starting model together with non-smoothing regularisation and a conservative model weighting strategy allowed me to locate the reservoir laterally at the right position and also to image changes in only a subset of the reservoir. However, I also showed that vertical resolution is rather poor

using surface based measurements. If the true depth of the reservoir is known one can exploit a positive feedback loop by adding a slightly resistive layer at reservoir depth into the starting model while keeping the reference model untouched. CSEM is generally sensitive to horizontal resistive structures, thus slightly higher resistive structures in the starting model will result in larger updates inside that layer, increasing sensitivity even further thus creating a positive feedback loop.

Recommendations for future monitoring projects

Within the larger research project and in particular working on this thesis the following recommendations for any future reservoir monitoring project can be made. In order to obtain a good background model a large scale exploration measurement should be performed before designing the actual source-receiver layout for the monitoring itself.
If possible one should use several steel-cased well as long electrode by galvanic connection to the CSEM transmitter. If galvanic connection is not possible, one should try to set up the transmitter as close as possible to the casing to make use of a strong inductive coupling of transmitter and casing. Idealy one may try to connect the transmitter at depth to the wellbore.
In addition one should try to install Ez receivers at more than one location to increase sensitivity even further.

Bibliography

Ajo-Franklin, Jonathan B., Burke J. Minsley and Thomas M. Daley (2007). "Applying compactness constraints to differential traveltime tomography". In: *Geophysics* 72.4, pp. 67–75. DOI: 10.1190/1.2742496.

Anderson, E. et al. (1999). *LAPACK Users' Guide*. Third. Philadelphia, PA: Society for Industrial and Applied Mathematics.

Archie, G. E. (1942). "The Electrical Resistivity Log as an Aid in Determining Some Reservoir Characteristics". In: 146, pp. 54–62. DOI: 10.2118/942054-g.

Betz, D. et al. (1987). "Evolution of the Lower Saxony Basin". In: *Tectonophysics* 137.1, pp. 127–170. DOI: 10.1016/0040-1951(87)90319-2.

Candansayar, M. Emin (2008). "Two-dimensional inversion of magnetotelluric data with consecutive use of conjugate gradient and least-squares solution with singular value decomposition algorithms". In: *Geophysical Prospecting* 56, pp. 141–157.

Chave, A. D. and J. T. Smith (1994). "On electric and magnetic galvanic distortion tensor decompositions". In: *Journal of Geophysical Research* 99.B3, pp. 4669–4682.

Commer, Michael, G. Michael Hoversten and Evan Schankee Um (2015). "Transient-electromagnetic finite-difference time-domain earth modeling over steel infrastructure". In: *GEOPHYSICS* 80.2, E147–E162. DOI: 10.1190/geo2014-0324.1.

Constable, Steven C. (2010). "Ten years of marine CSEM for hydrocarbon exploration". In: *Geophysics* 75.5, 75A67 –75A81.

Constable, Steven C., Robert L. Parker and Catherine G. Constable (1987). "Occam's inversion: A practical algorithm for generating smooth models from electromagnetic sounding data". In: *Geophysics* 52.3, pp. 289 –300.

Dadashpour, Mhsen, Martin Landrø and John Kleppe (2008). "Nonlinear inversion for estimating reservoir parameters from time-lapse seismic data". In: *Journal of Geophysics and Engineering* 5, pp. 54–66.

Daily, William et al. (1992). "Electrical Resitivity Tomography of Vadose Water Movement". In: *Water Resources Research* 28, pp. 1429–1442.

Doetsch, Joseph, Niklas Linde and Andrew Binley (2010). "Structural joint inversion of time-lapse crosshole ERT and GPR traveltime data". In: *Geophysical Research Letters* 37.

Grayver, A. V., R. Streich and O. Ritter (2013). "Three-dimensional parallel distributed inversion of CSEM data using a direct forward solver". In: *Geophysical Journal International* 193.3, pp. 1432–1446. DOI: 10.1093/gji/ggt055.

Harrington, Roger F (1968). "Field computation by method of moments". In: *NY Mc Millan*.

Hayley, Kevin, A. Pidlisecky and L.R. Bentley (2011). "Simultaneous time-lapse electrical resistivity inversion". In: *Journal of Applied Geophysics* 75, pp. 401–411.

Hibbs, A.D. et al. "Advances in Electromagnetic Survey Instrumentation and the Use of a Cased Borehole for Imaging a Deep Formations". In:

Jaysaval, Piyoosh, Daniil Shantsev and Sébastian de la Kethulle de Ryhove (2014). "Fast multimodel finite-difference controlled-source electromagnetic simulations based on a Schur complement approach". In: *Geophysics* 79.6, E315 –E327. DOI: 10.1190/GEO2014-0043.1.

Jiracek, George R. (1990). "Near-surface and topographic distortions in electromagentic induction". In: *Surveys in Geophysics* 11, pp. 163–203.

Jones, Alan G. (1988). "Static shift of magnetotelluric data and its removal in sedimentary basin environment". In: *Geophysics* 55.7, pp. 967–978.

Key, Kerry (2016). "MARE2DEM: a 2-D inversion code for controlled-source electromagnetic and magnetotelluric data". In: *Geophysical Journal International* 207.1, pp. 571–588. DOI: 10.1093/gji/ggw290.

Kim, Hee Joon and YoungHee Kim (2011). "A unified transformation function for lower and upper bounding constraints on model parameters in electrical and electromagnetic inversion". In: *Journal of Geophysics and Engineering* 8, pp. 21 –26.

Kohnke, Colton et al. (2017). "A method of moments approach to modeling the electromagnetic response of multiple steel casings in a layered earth". In: *GEOPHYSICS* 0.ja, pp. 1–72. DOI: 10.1190/geo2017-0303.1.

LaBrecque, Douglas J. and Xianjin Yang (2001). "Difference Inversion of ERT Data: a Fast Inversion Method for 3D- In Situ Monitoring". In: *Journal of Environmental and Engineering Geophysics* 6, pp. 83–89.

Miensopust, Marion P. (2017). "Application of 3-D Electromagnetic Inversion in Practice: Challenges, Pitfalls and Solution Approaches". In: *Surveys in Geophysics* 38.5, pp. 869–933. DOI: 10.1007/s10712-017-9435-1.

Orange, Arnold, Kerry Key and Steven Constable (2009). "The feasibility of reservoir monitoring using time-lapse marine CSEM". In: *Geophysics* 74.2, F21–F29. DOI: 10.1190/1.3059600.

Patzer, Cedric, Kristina Tietze and Oliver Ritter (2017b). "Steel-cased wells in 3-D controlled source EM modelling". In: *Geophysical Journal International* 209, pp. 813–826. DOI: 10.1093/gji/ggx049.

Patzer, Cedric, Kristina Tietze and Oliver Ritter (2019). "Elongated horizontal and verticalreceivers in three-dimensional electromagnetic modelling and inversion". In: *Geophysical Prospecting*. DOI: 10.1111/1365-2478.12830.

Poll, Helena E., J. T. Weaver and Alan G. Jones (1989). "Calculations of voltages for magnetotelluric modelling of a region with near-surface inhomogeneities". In: *Physics of the Earth and Planetary Interiors* 53, pp. 287 –297. DOI: 10.1016/0031-9201(89)90013-7.

Portniaguine, Oleg and Michael S. Zhdanov (1999). "Focusing geophysical inversion images". In: *Geophysics* 64, pp. 874–887.

Raiche, A. P. (1974). "An Integral Equation Approach to Three-Dimensional Modelling". In: *Geophysical Journal of the Royal Astronomical Society* 36, pp. 363–376. DOI: 10.1111/j.1365-246x.1974.tb03645.x.

Rosas-Carbajal, M. et al. (2015). "Probabilistic 3-D time-lapse inversion of magnetotelluric data: application to an enhanced geothermal system". In: *Geophysical Journal International* 203.3, pp. 1946–1960. DOI: 10.1093/gji/ggv406.

Rosas Carbajal, Marina, Niklas Linde and Thomas Kalscheuer (2012). "Focused time-lapse inversion of radio and audio magnetotelluric data". In: *Journal of Applied Geophysics* 84, pp. 29–38.

Sacchi, Mauricio D. and Tadeusz J. Ulrych (1996). "Estimation of the discrete Fourier transform, a linear inversion approach". In: *Geophysics* 61.4, p. 1128. DOI: 10.1190/1.1444033.

Schaller, Andreas (2018). "Land time-lapse CSEM Collecting, modeling and inversion of CSEM data for a steam-injected oil field". PhD thesis. TU Delft.

Schaller, Andreas et al. (2018). "A land-based controlled-source electromagnetic method for oil field exploration An example from the Schoonebeek oil field". In: *Geophysics* 83.2, WB1–WB17. DOI: 10.1190/geo2017-0022.1.

Schamper, C. et al. (2011). "Theoretical analysis of long offset time-lapse frequency domain controlled source electromagnetic signals using the method of moments: Application to the monitoring of a land oil reservoir". In: *Journal of Geophysical Research: Solid Earth* 116.B3. DOI: 10.1029/2009jb007114.

Simpson, Fiona and Karsten Bahr (2005). *Practical Magnetotellurics*. Cambridge University Press.

Streich, Rita (2009). "3Dfinite-difference frequency-domain modeling of controlled-source electromagnetic data: Direct solution and optimzation for high accuracy". In: *Geophysics* 74, pp. 95–105. DOI: 10.1190/1.3196241.

Streich, Rita (2016). "Controlled-Source Electromagnetic Approaches for Hydrocarbon Exploration and Monitoring on Land". In: *Surveys in Geophysics* 37, pp. 47–80.

Streich, Rita and Michael Becken (2011a). "Electromagnetic fields generated by finite-length wire source: comparison with point dipole solutions". In: *Geophysical Prospecting* 59, pp. 361–374.

Streich, Rita and Michael Becken (2011b). "Sensitivity of controlled-source electromagnetic fields in planarly layered media". In: *Geophysical Journal International* 187, pp. 705–728. DOI: 10.1111/j.1365-246x.2011.05203.x.

Streich, Rita, Michael Becken and Oliver Ritter (2010). "Imaging of CO2 storage sites, geothermal reservoirs and gas shales using controlled-source magnetotellurics: Modeling studies". In: *Chemie der Erde* 70, pp. 63–75.

Streich, Rita, Michael Becken and Oliver Ritter (2013). "Robust processing of noisy land-based controlled source electromagnetic data". In: *Geophysics* 78, pp. 237–247. DOI: 10.1190/geo2013-0026.1.

Tang, Wenwu et al. (2015). "Three-dimensional controlled-source electromagnetic modelling with a well casing as a grounded source: a hybrid method of moments and finite element scheme". In: *Geophysical Prospecting* 63.6, pp. 1491–1507. DOI: 10.1111/1365-2478.12330.

Tietze, K. et al. (2016). "3D inversion of controlled-source electromagnetic data in the presence of steel-cased wells". In: *23rd Workshop on Electromagnetic Induction in the Earth, Chiang Mai, Thailand, 14 - 20 August Poster presentation.*

Tietze, K., C. Patzer and O. Ritter (2018b). "Repeatability of Land Based CSEM data in high noise condition". In: *GJI* xxx, pp. xxx–xxx.

Tietze, Kristina, Oliver Ritter and Paul Veeken (2015). "Controlled-source electromagnetic monitoring of reservoir oil saturation using a novel borehole-to-surface configuration". In: *Geophysical Prospecting* 63.6, pp. 1468–1490. DOI: 10.1111/1365-2478.12322.

Tietze, Kristina, Oliver Ritter and Paul Veeken (2017). "Erratum: controlled-source electromagnetic monitoring of reservoir oil-saturation using a novel borehole-to-surface configuration". In: *Geophysical Prospecting* 65, pp. 317–321. DOI: 10.1111/1365-2478.12550.

Tikhonov, A. N. and V. IA. Arsenin (1977). *Solutions of ill-posed problems*. English. Vh Winston, xiii, 258 p. :

Vilamajó, E. et al. (2015). "A land controlled-source electromagnetic experiment using a deep vertical electric dipole: experimental settings, processing, and first data interpretation". In: *Geophysical Prospecting* 63.6, pp. 1527–1540. DOI: 10.1111/1365-2478.12331.

Wait, J.R. and D.A. Hill (1973). "Excitation of a homogeneous conductive cylinder of finite length by a prescribed axial current distribution". In: *Radio Sci.* 8.12, 1169–1176.

Weiss, Chester J. (2017). "Finite-element analysis for model parameters distributed on a hierarchy of geometric simplices". In: *Geophysics* 82.4, E155–E167. DOI: 10.1190/geo2017-0058.1.

Wirianto, M., W.A. Mulder and E.C.Slob (2010). "A feasibility study of land CSEM reservoir monitoring in a complex 3D- model". In: *Geophysical Journal International* 181, pp. 741–755. DOI: 10.1111/j.1365-246x.2010.04544.x.

Yang, Wei et al. (2009). "1D subsurface electromagnetic fields excited by energized steel casing". In: *GEOPHYSICS* 74.4, E159–E180. DOI: 10.1190/1.3131382.

Zhdanov, Michael S. (2010). "Electromagnetic geophysics: Notes from the past and the road ahead". In: *Geophysics* 75.5, 75A49 –75A66.

Acknowledgements

This work would not have been possible without the constant support of many different people.
First of all I would like to acknowledge the constant support of my supervisor Prof Dr. Oliver Ritter. During the entire time of this thesis he gave me the freedom to work on my ideas and I never had the feeling of being supervised but rather guided towards the completion of this work.
Furthermore I am great-full to have closely worked together with Dr. Kristina Tietze who was doing the bulk of the (literally daily) supervision. Thank you for the endless hours of fruitful discussions and recommendations, staying patient whenever new bugs in the developed software emerged, and helping in the writing of all the reports, abstracts and manuscripts.
Many thanks also go to Dr. Alexander Grayver whose work I build upon and who was willingly answering technical questions concerning his implementation. I could always ask for his opinions on certain ideas, before spending hours in the implementation.
I would like to thank Dr. Anna Platz for polishing large parts of this thesis as well as spending many hours discussing lots of my inversion results.
Furthermore I would like to express my gratitude to Dr. Paul Veeken and Dr. Meindert Dillen as well Bert Verboom and all the other people from Wintershall Holding both in Kassel as well as in Barnstorf who made this project possible by funding this work as well as providing constant support not only in the preparation of the field work but also outside.
I also appreciate to had the opportunity to work with all the different people from the EM-group of GFZ. It was a pleasure being part of this group. I highly enjoyed the joined meetings with the MT group of the FU Berlin and GFZ where I was able to present and discuss my results in an open and honest way.
Although not the main focus of my work field work would not have been possible with the equipment of the geophysical instrument pool of the GFZ and all the people that participated. The results from these measurements were of great value for the development of my thesis.
Finally I would like to thank my parents to whom I could always come and talk to and for providing the moral support during the entire time of this work.

Curriculum Vitae

For reasons of data protection, the curriculum vitae is not published in the electronic version.

Publications

Patzer, Cedric, Kristina Tietze and Oliver Ritter (2017b). "Steel-cased wells in 3-D controlled source EM modelling". In: *Geophysical Journal International* 209, pp. 813–826. DOI: 10.1093/gji/ggx049.

Patzer, Cedric, Kristina Tietze and Oliver Ritter (2019). "Elongated horizontal and verticalreceivers in three-dimensional electromagnetic modelling and inversion". In: *Geophysical Prospecting*. DOI: 10.1111/1365-2478.12830.

Conference Contributions

Patzer, C., K. Tietze and O. Ritter (2015). "Modelling the effect of steel cased boreholes on Controlled Source EM responses". In: *26th Schmucker Weidelt Colloquium on Electromagnetic Depth Sounding, Dassel, Germany, 21 - 25 September 2015. Oral presentation.*

Patzer, C., K. Tietze and O. Ritter (2016a). "3D CSEM forward modelling and inversion in the presence of steel cased wells". In: *23rd Workshop on Electromagnetic Induction in the Earth, Chiang Mai, Thailand, 14 – 20 August 2016. Poster presentation.*

Patzer, C., K. Tietze and O. Ritter (2016b). "CSEM monitoring in a producing oil field using cascaded inversion." In: *23rd Workshop on Electromagnetic Induction in the Earth, Chiang Mai, Thailand, 14 – 20 August 2016. Oral presentation*.

Patzer, C., K. Tietze and O. Ritter (2016c). "Three dimensional CSEM modelling in a producing oil field - the effect of steel-cased wells". In: *Annual Meeting of the German Geophysical Society (DGG), Münster, 14- 17 March 2016. Oral presentation.*

Patzer, C., K. Tietze and O. Ritter (2017a). "Time-lapse CSEM inversion using focusing regularization techniques for reservoir monitoring". In: *Society of Exploration Geophysicists International Exposition and 87th Annual Meeting, Houston, TX, USA. Expanded abstract, Oral presentation.*

Patzer, C., K. Tietze and O. Ritter (2018). "3D modelling and inversion using elongated electric field receivers". In: *24th Workshop on Electromagnetic Induction in the Earth, Helsingør, Denmark, 12 - 19 August 2018. Oral presentation.*

Tietze, K., O. Ritter and C. Patzer (2018a). "Repeatability of CSEM Measurements on Land and 4D Inversion Concepts". In: *80th EAGE Conference & Exhibition, Copenhagen, Denmark, 11 - 14 June 2018. Oral presentation.*